

Acta Crystallographica Section E

## Structure Reports

Online

ISSN 1600-5368

## Tris(ethylenediamine)cobalt(II) sulfate

Bunlawee Yotnoi, Athittaya Seecharaj, Yothin Chimupala and Apinpus Rujiwatra\*

Department of Chemistry, Faculty of Science, Chiang Mai University, Chiang Mai 50200, Thailand

Correspondence e-mail: apinpus@gmail.com

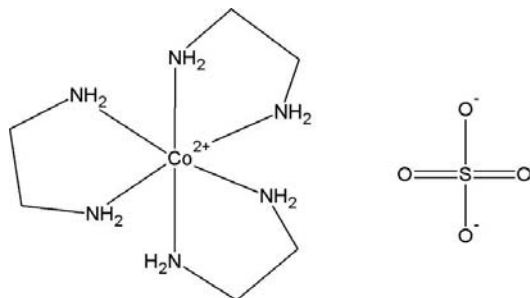
Received 27 April 2010; accepted 3 May 2010

Key indicators: single-crystal X-ray study;  $T = 298\text{ K}$ ; mean  $\sigma(\text{C}-\text{C}) = 0.003\text{ \AA}$ ; disorder in main residue;  $R$  factor = 0.028;  $wR$  factor = 0.069; data-to-parameter ratio = 14.6.

The structure of the title compound,  $[\text{Co}^{\text{II}}(\text{C}_2\text{H}_8\text{N}_2)_3]\text{SO}_4$ , the cobalt example of  $[M(\text{C}_2\text{H}_8\text{N}_2)_3]\text{SO}_4$ , is reported. The Co and S atoms are located at the 2d and 2c Wyckoff sites (point symmetry 32), respectively. The Co atom is coordinated by six N atoms of three chelating ethylenediamine molecules generated from half of the ethylenediamine molecule in the asymmetric unit. The O atoms of the sulfate anion are disordered mostly over two crystallographic sites. The third disorder site of O (site symmetry 3) has a site occupancy approaching zero. The H atoms of the ethylenediamine molecules interact with the sulfate anions *via* intermolecular  $\text{N}-\text{H}\cdots\text{O}$  hydrogen-bonding interactions.

## Related literature

For isostructural  $[M(\text{C}_2\text{H}_8\text{N}_2)_3]\text{SO}_4$  complexes, see: Haque *et al.* (1970); Cullen & Lingafelter (1970); Daniels *et al.* (1995); Lu (2009) for the nickel, copper, vanadium and manganese analogues, respectively.



## Experimental

## Crystal data

$[\text{Co}(\text{C}_2\text{H}_8\text{N}_2)_3]\text{SO}_4$   
 $M_r = 335.30$   
 Trigonal,  $P\bar{3}1c$

$a = 8.9920\text{ (2) \AA}$   
 $c = 9.5927\text{ (3) \AA}$   
 $V = 671.71\text{ (3) \AA}^3$

 $Z = 2$ 

Mo  $K\alpha$  radiation  
 $\mu = 1.45\text{ mm}^{-1}$

 $T = 298\text{ K}$  $0.48 \times 0.22 \times 0.20\text{ mm}$ 

## Data collection

Bruker SMART CCD area-detector diffractometer  
 Absorption correction: multi-scan (*SADABS*; Sheldrick, 1996)  
 $T_{\min} = 0.543$ ,  $T_{\max} = 0.760$

3638 measured reflections  
 688 independent reflections  
 589 reflections with  $I > 2\sigma(I)$   
 $R_{\text{int}} = 0.027$

## Refinement

$R[F^2 > 2\sigma(F^2)] = 0.028$   
 $wR(F^2) = 0.069$   
 $S = 1.06$   
 688 reflections  
 47 parameters

16 restraints  
 H-atom parameters constrained  
 $\Delta\rho_{\max} = 0.25\text{ e \AA}^{-3}$   
 $\Delta\rho_{\min} = -0.29\text{ e \AA}^{-3}$

Table 1

Hydrogen-bond geometry ( $\text{\AA}$ ,  $^\circ$ ).

$D-\text{H}\cdots A$	$D-\text{H}$	$\text{H}\cdots A$	$D\cdots A$	$D-\text{H}\cdots A$
$\text{N1}-\text{H1A}\cdots\text{O3}^{\text{i}}$	0.90	2.13	2.889 (12)	142
$\text{N1}-\text{H1A}\cdots\text{O1}^{\text{i}}$	0.90	2.15	3.049 (7)	176
$\text{N1}-\text{H1A}\cdots\text{O2}^{\text{ii}}$	0.90	2.22	3.054 (8)	155
$\text{N1}-\text{H1A}\cdots\text{O2}^{\text{iii}}$	0.90	2.32	3.104 (11)	145
$\text{N1}-\text{H1B}\cdots\text{O2}^{\text{iv}}$	0.90	1.98	2.843 (6)	161
$\text{N1}-\text{H1B}\cdots\text{O1}$	0.90	2.48	3.353 (14)	165
$\text{N1}-\text{H1B}\cdots\text{O1}^{\text{v}}$	0.90	2.52	3.256 (10)	139

Symmetry codes: (i)  $-x+1, -y+1, -z$ ; (ii)  $y, -x+y, -z$ ; (iii)  $x-y+1, x, -z$ ; (iv)  $-x+y, -x+1, z$ ; (v)  $-y+1, -x+1, -z+\frac{1}{2}$ .

Data collection: *SMART* (Bruker, 2003); cell refinement: *SAINT* (Bruker, 2003); data reduction: *SAINT*; program(s) used to solve structure: *SHELXS97* (Sheldrick, 2008) and *WinGX* (Farrugia, 1999); program(s) used to refine structure: *SHELXL97* (Sheldrick, 2008) and *WinGX* (Farrugia, 1999); molecular graphics: *DIAMOND* (Brandenburg, 2006); software used to prepare material for publication: *PUBLICIF* (Westrip, 2010).

This work was supported financially by the Thailand Research Fund and the Center of Excellence for Innovation in Chemistry. BY thanks the Royal Golden Jubilee PhD program and the Graduate School of Chiang Mai University for a graduate scholarship.

Supplementary data and figures for this paper are available from the IUCr electronic archives (Reference: TK2667).

## References

- Brandenburg, K. (2006). *DIAMOND*. Crystal Impact GbR, Bonn, Germany.  
 Bruker (2003). *SMART* and *SAINT*. Bruker AXS Inc., Madison, Wisconsin, USA.  
 Cullen, D. L. & Lingafelter, E. C. (1970). *Inorg. Chem.* **9**, 1858–1864.  
 Daniels, L. M., Murillo, C. A. & Rodriguez, K. G. (1995). *Inorg. Chim. Acta*, **229**, 27–32.  
 Farrugia, L. J. (1999). *J. Appl. Cryst.* **32**, 837–838.  
 Haque, M.-U., Caughlan, C. N. & Emerson, K. (1970). *Inorg. Chem.* **9**, 2421–2424.  
 Lu, J. (2009). *Acta Cryst.* **E65**, m1187.  
 Sheldrick, G. M. (1996). *SADABS*. University of Göttingen, Germany.  
 Sheldrick, G. M. (2008). *Acta Cryst.* **A64**, 112–122.  
 Westrip, S. P. (2010). *J. Appl. Cryst.* **43**. Submitted.

*Acta Cryst.* (2010). E66, m628 [doi:10.1107/S1600536810016168]

## Tris(ethylenediamine)cobalt(II) sulfate

B. Yotnoi, A. Seeharaj, Y. Chimupala and A. Rujiwatra

### Comment

The title complex,  $[\text{Co}^{\text{II}}(\text{C}_2\text{H}_8\text{N}_2)_3]\text{SO}_4$  (Fig. 1), is isostructural to the earlier reported  $[\text{Ni}^{\text{II}}(\text{C}_2\text{H}_8\text{N}_2)_3]\text{SO}_4$  (Haque *et al.*, 1970),  $[\text{V}^{\text{II}}(\text{C}_2\text{H}_8\text{N}_2)_3]\text{SO}_4$  (Daniels *et al.*, 1995),  $[\text{Mn}^{\text{II}}(\text{C}_2\text{H}_8\text{N}_2)_3]\text{SO}_4$  (Lu, 2009) and  $[\text{Cu}^{\text{II}}(\text{C}_2\text{H}_8\text{N}_2)_3]\text{SO}_4$  (Cullen & Lingafelter, 1970) complexes, constituting the  $[\text{M}^{\text{II}}(\text{C}_2\text{H}_8\text{N}_2)_3]\text{SO}_4$  series. The  $[\text{M}^{\text{II}}(\text{C}_2\text{H}_8\text{N}_2)_3]\text{SO}_4$  structures crystallize in the same trigonal space group of  $\text{P}\bar{3}1\text{c}$  with quite similar cell parameters. Likewise, the metal and sulfur atoms are positioned in the same crystallographic sites;  $\text{M}^{\text{II}}$  on the  $2d$  and S on the  $2c$  Wyckoff sites (each with point symmetry 32). The disorder about the six-fold rotation axis found in the sulfate anion is intriguingly common in each structure, although the number of unique O atoms varies from two to four. In the structure of  $[\text{Co}^{\text{II}}(\text{C}_2\text{H}_8\text{N}_2)_3]\text{SO}_4$ , the O atoms were refined as being disordered over three crystallographic sites, although the site occupancy of O3 located on the  $4f$  Wyckoff site approaches zero. The bond length associated with this O3 atom (S1—O3; 1.382 (16) Å) is notably shorter than the other S—O bonds (1.431 (5)–1.445 (5) Å). The disordered sulfate anions are linked to the  $[\text{Co}^{\text{II}}(\text{C}_2\text{H}_8\text{N}_2)_3]^{2+}$  cations by hydrogen bonding interactions of N—H $\cdots$ O type to form a hydrogen-bonding supramolecular network. The hydrogen bonding geometries are consistent with those of the previously reported  $[\text{M}^{\text{II}}(\text{C}_2\text{H}_8\text{N}_2)_3]\text{SO}_4$  complexes.

### Experimental

Orange blocks of the title complex were synthesized and grown from the solvothermal reaction of  $\text{Co}(\text{NO}_3)_2 \cdot 6\text{H}_2\text{O}$  (1.34 mmol),  $\text{NH}_2\text{SO}_3\text{H}$  (1.34 mmol),  $\text{NH}_2\text{C}_2\text{H}_4\text{NH}_2$  (3.89 mmol) in ethylene glycol (160 mmol), conducted at 453 K for 72 h.

### Refinement

The O atoms were positioned from a difference Fourier map, and refined with restraints using commands SUMP, SADI and SIMU in *SHELXL* (Sheldrick, 2008). Although there was an indication for further splitting of the O2 atom, after the final cycles of refinement, such action did not give a better result. All H-atoms were treated as riding groups on the bonded atoms, with C—H = 0.97 Å and N—H 0.90 Å, and with  $U_{\text{iso}}(\text{H}) = 1.2U_{\text{equiv}}(\text{C}, \text{N})$ .

### Figures

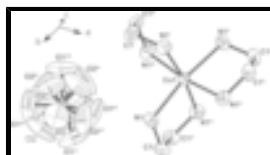


Fig. 1. View of the title complex showing atom numbering scheme. Displacement ellipsoids for non-H atoms are drawn at the 50% probability level. [Symmetry codes: (i)  $-y+1, x-y, z$ ; (ii)  $-x+y+1, -x+1, z$ ; (iii)  $-y+1, -x+1, -z+1/2$ ; (iv)  $-x+y+1, y, -z+1/2$ ; (v)  $x, x-y, -z+1/2$ ; (vi)  $-y+1, x-y+1, z$ ; (vii)  $-x+y, -x+1, z$ ; (viii)  $-x+y, y, -z+1/2$ ; (ix)  $x, x-y+1, -z+1/2$ ]. Hydrogen atoms are omitted.

# supplementary materials

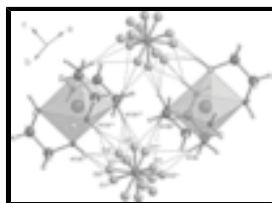


Fig. 2. View of the hydrogen bonding interactions (dotted lines) between the disordered sulfate O atoms and the amino-H atoms of the  $[\text{Co}^{\text{II}}(\text{C}_2\text{H}_8\text{N}_2)]^{2+}$  cations. [Symmetry codes: (ii)  $-x+y+1, -x+1, z$ ; (iii)  $-y+1, -x+1, -z+1/2$ ; (viii)  $-x+y, y, -z+1/2$ ; (ix)  $x, x-y+1, -z+1/2$ ; (xiii)  $y, x, z+1/2$ ; (xiv)  $-y+x, -y+1, -z+1/2$ ; (xv)  $-x+1, -x+y+1, z+1/2$ ].

## Tris(ethylenediamine)cobalt(II) sulfate

### Crystal data

$[\text{Co}(\text{C}_2\text{H}_8\text{N}_2)_3]\text{SO}_4$

$M_r = 335.30$

Trigonal,  $P\bar{3}1c$

Hall symbol:  $-P\ 3\ 2c$

$a = 8.9920\ (2)\ \text{\AA}$

$c = 9.5927\ (3)\ \text{\AA}$

$V = 671.71\ (3)\ \text{\AA}^3$

$Z = 2$

$F(000) = 354$

$D_x = 1.658\ \text{Mg m}^{-3}$

Mo  $K\alpha$  radiation,  $\lambda = 0.71073\ \text{\AA}$

Cell parameters from 589 reflections

$\theta = 2.6\text{--}31.0^\circ$

$\mu = 1.45\ \text{mm}^{-1}$

$T = 298\ \text{K}$

Block, orange

$0.48 \times 0.22 \times 0.20\ \text{mm}$

### Data collection

Bruker SMART CCD area-detector diffractometer

Radiation source: fine-focus sealed tube graphite

? scan

Absorption correction: multi-scan (SADABS; Sheldrick, 1996)

$T_{\min} = 0.543$ ,  $T_{\max} = 0.760$

3638 measured reflections

688 independent reflections

589 reflections with  $I > 2\sigma(I)$

$R_{\text{int}} = 0.027$

$\theta_{\max} = 31.0^\circ$ ,  $\theta_{\min} = 2.6^\circ$

$h = -8 \rightarrow 10$

$k = -11 \rightarrow 11$

$l = -11 \rightarrow 13$

### Refinement

Refinement on  $F^2$

Least-squares matrix: full

$R[F^2 > 2\sigma(F^2)] = 0.028$

$wR(F^2) = 0.069$

$S = 1.06$

688 reflections

47 parameters

16 restraints

Primary atom site location: structure-invariant direct methods

Secondary atom site location: difference Fourier map

Hydrogen site location: inferred from neighbouring sites

H-atom parameters constrained

$w = 1/[\sigma^2(F_o^2) + (0.0354P)^2 + 0.1217P]$

where  $P = (F_o^2 + 2F_c^2)/3$

$(\Delta/\sigma)_{\max} < 0.001$

$\Delta\rho_{\max} = 0.25\ \text{e \AA}^{-3}$

$\Delta\rho_{\min} = -0.29\ \text{e \AA}^{-3}$

*Special details*

**Geometry.** All esds (except the esd in the dihedral angle between two l.s. planes) are estimated using the full covariance matrix. The cell esds are taken into account individually in the estimation of esds in distances, angles and torsion angles; correlations between esds in cell parameters are only used when they are defined by crystal symmetry. An approximate (isotropic) treatment of cell esds is used for estimating esds involving l.s. planes.

**Refinement.** Refinement of  $F^2$  against ALL reflections. The weighted  $R$ -factor  $wR$  and goodness of fit  $S$  are based on  $F^2$ , conventional  $R$ -factors  $R$  are based on  $F$ , with  $F$  set to zero for negative  $F^2$ . The threshold expression of  $F^2 > \sigma(F^2)$  is used only for calculating  $R$ -factors(gt) etc. and is not relevant to the choice of reflections for refinement.  $R$ -factors based on  $F^2$  are statistically about twice as large as those based on  $F$ , and  $R$ -factors based on ALL data will be even larger.

*Fractional atomic coordinates and isotropic or equivalent isotropic displacement parameters ( $\text{\AA}^2$ )*

	<i>x</i>	<i>y</i>	<i>z</i>	$U_{\text{iso}}^*/U_{\text{eq}}$	Occ. (<1)
Co1	0.6667	0.3333	0.2500	0.02175 (16)	
N1	0.68784 (18)	0.54599 (18)	0.12760 (13)	0.0332 (3)	
H1A	0.6936	0.5265	0.0363	0.040*	
H1B	0.5954	0.5579	0.1418	0.040*	
S1	0.3333	0.6667	0.2500	0.0240 (2)	
C1	0.8446 (2)	0.7024 (2)	0.17145 (19)	0.0388 (4)	
H1C	0.8405	0.8031	0.1409	0.047*	
H1D	0.9444	0.7056	0.1297	0.047*	
O1	0.3029 (19)	0.5088 (9)	0.1852 (8)	0.096 (3)	0.319 (8)
O2	0.339 (2)	0.7851 (9)	0.1475 (6)	0.096 (4)	0.316 (9)
O3	0.3333	0.6667	0.1059 (16)	0.086 (8)	0.094 (10)

*Atomic displacement parameters ( $\text{\AA}^2$ )*

	$U^{11}$	$U^{22}$	$U^{33}$	$U^{12}$	$U^{13}$	$U^{23}$
Co1	0.0226 (2)	0.0226 (2)	0.0201 (2)	0.01129 (10)	0.000	0.000
N1	0.0410 (8)	0.0330 (7)	0.0283 (7)	0.0204 (6)	−0.0033 (5)	0.0031 (5)
S1	0.0243 (3)	0.0243 (3)	0.0233 (4)	0.01215 (14)	0.000	0.000
C1	0.0445 (10)	0.0267 (8)	0.0413 (9)	0.0147 (7)	0.0058 (7)	0.0076 (6)
O1	0.185 (9)	0.051 (4)	0.063 (4)	0.069 (5)	−0.012 (5)	−0.016 (3)
O2	0.194 (12)	0.055 (4)	0.044 (3)	0.067 (5)	−0.012 (4)	0.012 (3)
O3	0.118 (11)	0.118 (11)	0.021 (11)	0.059 (5)	0.000	0.000

*Geometric parameters ( $\text{\AA}$ ,  $^\circ$ )*

Co1—N1 <sup>i</sup>	2.1696 (13)	S1—O2 <sup>vi</sup>	1.431 (5)
Co1—N1 <sup>ii</sup>	2.1696 (13)	S1—O2 <sup>v</sup>	1.431 (5)
Co1—N1 <sup>iii</sup>	2.1696 (13)	S1—O2 <sup>vii</sup>	1.431 (5)
Co1—N1 <sup>iv</sup>	2.1696 (13)	S1—O2 <sup>viii</sup>	1.431 (5)
Co1—N1	2.1696 (13)	S1—O2 <sup>ix</sup>	1.431 (5)
Co1—N1 <sup>v</sup>	2.1696 (13)	S1—O1 <sup>ix</sup>	1.445 (5)

# supplementary materials

N1—C1	1.469 (2)	S1—O1 <sup>viii</sup>	1.445 (5)
N1—H1A	0.9000	S1—O1 <sup>vi</sup>	1.445 (5)
N1—H1B	0.9000	S1—O1 <sup>vii</sup>	1.445 (5)
S1—O3	1.382 (16)	C1—C1 <sup>iv</sup>	1.512 (4)
S1—O3 <sup>v</sup>	1.382 (16)	C1—H1C	0.9700
S1—O2	1.431 (5)	C1—H1D	0.9700
N1 <sup>i</sup> —Co1—N1 <sup>ii</sup>	80.49 (7)	O2 <sup>viii</sup> —S1—O1 <sup>viii</sup>	110.7 (4)
N1 <sup>i</sup> —Co1—N1 <sup>iii</sup>	93.48 (5)	O2 <sup>ix</sup> —S1—O1 <sup>viii</sup>	138.0 (11)
N1 <sup>ii</sup> —Co1—N1 <sup>iii</sup>	93.17 (8)	O1 <sup>ix</sup> —S1—O1 <sup>viii</sup>	63.4 (8)
N1 <sup>i</sup> —Co1—N1 <sup>iv</sup>	93.17 (8)	O3—S1—O1 <sup>vi</sup>	64.5 (3)
N1 <sup>ii</sup> —Co1—N1 <sup>iv</sup>	93.48 (5)	O3 <sup>v</sup> —S1—O1 <sup>vi</sup>	115.5 (3)
N1 <sup>iii</sup> —Co1—N1 <sup>iv</sup>	171.28 (7)	O2—S1—O1 <sup>vi</sup>	57.2 (5)
N1 <sup>i</sup> —Co1—N1	93.48 (5)	O2 <sup>vi</sup> —S1—O1 <sup>vi</sup>	110.7 (4)
N1 <sup>ii</sup> —Co1—N1	171.28 (8)	O2 <sup>v</sup> —S1—O1 <sup>vi</sup>	138.0 (11)
N1 <sup>iii</sup> —Co1—N1	93.48 (5)	O2 <sup>vii</sup> —S1—O1 <sup>vi</sup>	69.9 (6)
N1 <sup>iv</sup> —Co1—N1	80.49 (7)	O2 <sup>viii</sup> —S1—O1 <sup>vi</sup>	45.7 (4)
N1 <sup>i</sup> —Co1—N1 <sup>v</sup>	171.28 (8)	O2 <sup>ix</sup> —S1—O1 <sup>vi</sup>	119.2 (10)
N1 <sup>ii</sup> —Co1—N1 <sup>v</sup>	93.48 (5)	O1 <sup>ix</sup> —S1—O1 <sup>vi</sup>	93.3 (11)
N1 <sup>iii</sup> —Co1—N1 <sup>v</sup>	80.49 (7)	O1 <sup>viii</sup> —S1—O1 <sup>vi</sup>	102.9 (4)
N1 <sup>iv</sup> —Co1—N1 <sup>v</sup>	93.48 (5)	O3—S1—O1 <sup>vii</sup>	115.5 (3)
N1—Co1—N1 <sup>v</sup>	93.17 (8)	O3 <sup>v</sup> —S1—O1 <sup>vii</sup>	64.5 (3)
C1—N1—Co1	107.94 (10)	O2—S1—O1 <sup>vii</sup>	138.0 (11)
C1—N1—H1A	110.1	O2 <sup>vi</sup> —S1—O1 <sup>vii</sup>	69.9 (6)
Co1—N1—H1A	110.1	O2 <sup>v</sup> —S1—O1 <sup>vii</sup>	57.2 (5)
C1—N1—H1B	110.1	O2 <sup>vii</sup> —S1—O1 <sup>vii</sup>	110.7 (4)
Co1—N1—H1B	110.1	O2 <sup>viii</sup> —S1—O1 <sup>vii</sup>	119.2 (10)
H1A—N1—H1B	108.4	O2 <sup>ix</sup> —S1—O1 <sup>vii</sup>	45.7 (4)
O3—S1—O3 <sup>v</sup>	180.000 (3)	O1 <sup>ix</sup> —S1—O1 <sup>vii</sup>	102.9 (4)
O3—S1—O2	46.6 (3)	O1 <sup>viii</sup> —S1—O1 <sup>vii</sup>	93.3 (11)
O3 <sup>v</sup> —S1—O2	133.4 (3)	O1 <sup>vi</sup> —S1—O1 <sup>vii</sup>	161.1 (12)
O3—S1—O2 <sup>vi</sup>	46.6 (3)	N1—C1—C1 <sup>iv</sup>	108.84 (12)
O3 <sup>v</sup> —S1—O2 <sup>vi</sup>	133.4 (3)	N1—C1—H1C	109.9
O2—S1—O2 <sup>vi</sup>	78.0 (5)	C1 <sup>iv</sup> —C1—H1C	109.9
O3—S1—O2 <sup>v</sup>	133.4 (3)	N1—C1—H1D	109.9
O3 <sup>v</sup> —S1—O2 <sup>v</sup>	46.6 (3)	C1 <sup>iv</sup> —C1—H1D	109.9
O2—S1—O2 <sup>v</sup>	104.4 (11)	H1C—C1—H1D	108.3
O2 <sup>vi</sup> —S1—O2 <sup>v</sup>	99.7 (7)	O2 <sup>vi</sup> —O1—O2 <sup>viii</sup>	91.9 (8)
O3—S1—O2 <sup>vii</sup>	133.4 (3)	O2 <sup>vi</sup> —O1—S1	66.5 (5)
O3 <sup>v</sup> —S1—O2 <sup>vii</sup>	46.6 (3)	O2 <sup>viii</sup> —O1—S1	60.9 (3)
O2—S1—O2 <sup>vii</sup>	99.7 (7)	O2 <sup>vi</sup> —O1—O1 <sup>vii</sup>	75.7 (11)
O2 <sup>vi</sup> —S1—O2 <sup>vii</sup>	176.3 (13)	O2 <sup>viii</sup> —O1—O1 <sup>vii</sup>	117.8 (4)

O2 <sup>v</sup> —S1—O2 <sup>vii</sup>	78.0 (5)	S1—O1—O1 <sup>vii</sup>	58.3 (4)
O3—S1—O2 <sup>viii</sup>	46.6 (3)	O2 <sup>vi</sup> —O1—O2 <sup>ix</sup>	108.3 (7)
O3 <sup>v</sup> —S1—O2 <sup>viii</sup>	133.4 (3)	O2 <sup>viii</sup> —O1—O2 <sup>ix</sup>	92.2 (8)
O2—S1—O2 <sup>viii</sup>	78.0 (5)	S1—O1—O2 <sup>ix</sup>	54.6 (4)
O2 <sup>vi</sup> —S1—O2 <sup>viii</sup>	78.0 (5)	O1 <sup>viii</sup> —O2—O1 <sup>vi</sup>	129.8 (7)
O2 <sup>v</sup> —S1—O2 <sup>viii</sup>	176.3 (13)	O1 <sup>viii</sup> —O2—S1	67.8 (4)
O2 <sup>vii</sup> —S1—O2 <sup>viii</sup>	104.4 (11)	O1 <sup>vi</sup> —O2—S1	61.9 (4)
O3—S1—O2 <sup>ix</sup>	133.4 (3)	O1 <sup>viii</sup> —O2—O1 <sup>ix</sup>	63.3 (12)
O3 <sup>v</sup> —S1—O2 <sup>ix</sup>	46.6 (3)	O1 <sup>vi</sup> —O2—O1 <sup>ix</sup>	87.5 (9)
O2—S1—O2 <sup>ix</sup>	176.3 (13)	S1—O2—O1 <sup>ix</sup>	55.5 (3)
O2 <sup>vi</sup> —S1—O2 <sup>ix</sup>	104.4 (11)	O1 <sup>viii</sup> —O2—O2 <sup>vi</sup>	49.8 (6)
O2 <sup>v</sup> —S1—O2 <sup>ix</sup>	78.0 (5)	O1 <sup>vi</sup> —O2—O2 <sup>vi</sup>	95.3 (5)
O2 <sup>vii</sup> —S1—O2 <sup>ix</sup>	78.0 (5)	S1—O2—O2 <sup>vi</sup>	51.0 (2)
O2 <sup>viii</sup> —S1—O2 <sup>ix</sup>	99.7 (7)	O1 <sup>ix</sup> —O2—O2 <sup>vi</sup>	91.9 (8)
O3—S1—O1 <sup>ix</sup>	115.5 (3)	O1 <sup>viii</sup> —O2—O2 <sup>viii</sup>	106.1 (5)
O3 <sup>v</sup> —S1—O1 <sup>ix</sup>	64.5 (3)	S1—O2—O2 <sup>viii</sup>	51.0 (2)
O2—S1—O1 <sup>ix</sup>	69.9 (6)	O1 <sup>ix</sup> —O2—O2 <sup>viii</sup>	102.2 (4)
O2 <sup>vi</sup> —S1—O1 <sup>ix</sup>	119.2 (10)	O2 <sup>vi</sup> —O2—O2 <sup>viii</sup>	60.000 (1)
O2 <sup>v</sup> —S1—O1 <sup>ix</sup>	45.7 (4)	O2 <sup>vi</sup> —O3—O2 <sup>viii</sup>	107.9 (8)
O2 <sup>vii</sup> —S1—O1 <sup>ix</sup>	57.2 (5)	O2 <sup>vi</sup> —O3—S1	69.0 (8)
O2 <sup>viii</sup> —S1—O1 <sup>ix</sup>	138.0 (11)	O2 <sup>viii</sup> —O3—S1	69.0 (8)
O2 <sup>ix</sup> —S1—O1 <sup>ix</sup>	110.7 (4)	O2 <sup>vi</sup> —O3—O1 <sup>viii</sup>	61.1 (6)
O3—S1—O1 <sup>viii</sup>	64.5 (3)	O2 <sup>viii</sup> —O3—O1 <sup>viii</sup>	128.2 (13)
O3 <sup>v</sup> —S1—O1 <sup>viii</sup>	115.5 (3)	S1—O3—O1 <sup>viii</sup>	59.8 (5)
O2—S1—O1 <sup>viii</sup>	45.7 (4)	O2 <sup>vi</sup> —O3—O1 <sup>vi</sup>	128.2 (13)
O2 <sup>vi</sup> —S1—O1 <sup>viii</sup>	57.2 (5)	O2 <sup>viii</sup> —O3—O1 <sup>vi</sup>	47.4 (6)
O2 <sup>v</sup> —S1—O1 <sup>viii</sup>	69.9 (6)	S1—O3—O1 <sup>vi</sup>	59.8 (5)
O2 <sup>vii</sup> —S1—O1 <sup>viii</sup>	119.2 (10)	O1 <sup>viii</sup> —O3—O1 <sup>vi</sup>	96.9 (7)

Symmetry codes: (i)  $-x+y+1, -x+1, z$ ; (ii)  $x, x-y, -z+1/2$ ; (iii)  $-y+1, x-y, z$ ; (iv)  $-x+y+1, y, -z+1/2$ ; (v)  $-y+1, -x+1, -z+1/2$ ; (vi)  $-y+1, x-y+1, z$ ; (vii)  $-x+y, y, -z+1/2$ ; (viii)  $-x+y, -x+1, z$ ; (ix)  $x, x-y+1, -z+1/2$ .

#### Hydrogen-bond geometry ( $\text{\AA}, ^\circ$ )

<i>D</i> —H $\cdots$ <i>A</i>	<i>D</i> —H	H $\cdots$ <i>A</i>	<i>D</i> $\cdots$ <i>A</i>	<i>D</i> —H $\cdots$ <i>A</i>
N1—H1A $\cdots$ O3 <sup>x</sup>	0.90	2.13	2.889 (12)	142
N1—H1A $\cdots$ O1 <sup>x</sup>	0.90	2.15	3.049 (7)	176
N1—H1A $\cdots$ O2 <sup>xi</sup>	0.90	2.22	3.054 (8)	155
N1—H1A $\cdots$ O2 <sup>xii</sup>	0.90	2.32	3.104 (11)	145
N1—H1B $\cdots$ O2 <sup>viii</sup>	0.90	1.98	2.843 (6)	161
N1—H1B $\cdots$ O1	0.90	2.48	3.353 (14)	165
N1—H1B $\cdots$ O1 <sup>v</sup>	0.90	2.52	3.256 (10)	139

Symmetry codes: (x)  $-x+1, -y+1, -z$ ; (xi)  $y, -x+y, -z$ ; (xii)  $x-y+1, x, -z$ ; (viii)  $-x+y, -x+1, z$ ; (v)  $-y+1, -x+1, -z+1/2$ .



Chiang Mai J. Sci. 2010; 37(1) : 92-98  
www.science.cmu.ac.th/journal-science/josci.html  
Contributed Paper

## Hydrothermal Synthesis of Lead Titanate Fine Powders at Water Boiling Temperature

Chaiyos Chankaew [a,b], and Apinpus Rujiwatra\* [a,b]

[a] Department of Chemistry, Faculty of Science, Chiang Mai University, Chiang Mai 50200, Thailand.

[b] Center of Excellence for Innovation in Chemistry (Chiang Mai University), Commission on Higher Education, Ministry of Education, Thailand.

\*Author for correspondence; e-mail: apinpus@gmail.com

Received: 10 June 2009

Accepted: 22 July 2009

### ABSTRACT

Lead titanate fine powders comprising of a single tetragonal phase and well characterized particles were successfully synthesized at an exceptionally low temperature of 100 °C. The important role of the ultrasonication in reducing the thermodynamic barrier of the hydrothermal reaction, and the slow rate of hydrothermal reaction at 100°C were underlined. The synthesized particles were revealed to be tetragonal in shape, mostly submicrometers in size, and generally present as large aggregates. The layer-by-layer model was also proposed as the particle growth mechanism.

**Keywords:** lead titanate, perovskite, ultrasonication, hydrothermal synthesis.

### 1. INTRODUCTION

Among several wet-chemical routes available for the synthesis of advanced materials, hydrothermal technique has been proved to be very promising due to its uniqueness in being facile, cost effective, environmentally benign and applicable for the tailored synthesis of various phases in different forms [1]. Along this line, the hydrothermal technique has been applied for the synthesis of lead titanate ( $\text{PbTiO}_3$  or PT) [2,3] which is one of the most important ferroelectric materials. The high spontaneous polarization and piezoelectric coefficients, but low aging rate of dielectric constant as well as a remarkable anisotropy make the PT-based compounds suitable for a wide range of high temperature and frequency applications, *e.g.*

infrared sensors, electro-optic devices and ultrasonic transducers [4-6]. Compared to the other techniques *e.g.* sol-gel [7], chemical precipitation [8] and emulsion [9], the hydrothermal technique is somewhat superior in providing controllability on phase formation, chemical stoichiometry, particle size and morphology by simply fine tuning the processing parameters [3]. The recent stage of development for this technique involves the usage of other heating sources, *e.g.* a sand bath, an ultrasonic wave and a microwave, instead of the conventional oven [10-11]. The application of an ultrasonic wave on the reaction mixture in precedence to the hydrothermal reaction in particular has added advantages to the technique by both reducing



the reaction temperature providing the phase-pure PT nanoparticles, and promoting better size homogeneity [10]. The observed phenomena were rationalized by the formation of hot spots and local acoustic microjets from a sudden collapse of cavitation bubbles induced by the ultrasonic wave.

In the present work, a further investigation on the developed technique which has led to a dramatic reduction in the reaction temperature affording the phase-pure PT to an extraordinary low temperature of 100°C is reported. The influences of the ultrasonication and hydrothermal processing conditions on phase formation, particle size and habits of the PT powders are discussed.

## 2. MATERIALS AND METHODS

Due to the recent report on the apparent possibility in the synthesis of phase-pure PT fine powders at the water boiling temperature, there were therefore the attempts to conduct the reactions at 100 °C following the previously reported experimental procedure [10]. Mixtures of lead (II) nitrate ( $\text{Pb}(\text{NO}_3)_2$ , Univar 99.0%) and titanium (IV) oxide ( $\text{TiO}_2$ , Riedel-de Haen 99.5-100%) in anatase form were prepared in aqueous media. The amount of  $\text{Pb}^{\text{II}}$  and  $\text{Ti}^{\text{IV}}$  was controlled to be equimolar, and the final concentrations for each precursor were fixed at  $1.32 \text{ mol.dm}^{-3}$ . The pellets of potassium hydroxide (KOH, Merck 85%) as mineralizer were gradually added to each reaction mixture to adjust the pH of the mixture to be 14, reported as the minimal pH required yielding well crystallized powder [2]. Such a high alkalinity is allegedly necessary for the dissolution of the oxide precursors under hydrothermal conditions. The mixtures were transferred into Teflon liners, which were then sealed and ultrasonicated at  $70(\pm 5)^\circ\text{C}$  for varied durations ranging from 1 h to 6 h, using a laboratory ultrasonic bath (Bandelin

Electronic RK255H, 160/320W, 35kHz). The liners were fitted in stainless steel cases for further hydrothermal reactions conducted under autogenous pressure at 100°C for 1.5-144 h. The particles were then recovered by filtration, washed with deionized water, and dried in air.

Powder X-ray diffractometer (PXRD, Siemen D500/D501,  $\text{CuK}_\alpha$ , Ni filter,  $\lambda=1.54 \text{ \AA}$ ) was used to characterize the crystalline phases, and field emission scanning electron microscope (FESEM, JEOL JSM-6335F) equipped with an energy dispersive X-ray (EDX) analyzer was employed for the investigation of particle morphology, size and elemental composition. In order to study the aggregation of the synthesized PT particles, size distributions of the bulk samples were analyzed by laser diffraction technique (Malvern Instruments Limited, Mastersizer S).

## 3. RESULTS AND DISCUSSION

According to the PXRD results as shown in Figure 1 to Figure 3, the preceding ultrasonication was an important factor in reducing the hydrothermal reaction temperature affording the phase-pure PT powders although the bargaining between the ultrasonication duration and the hydrothermal reaction time was mandatory. It was evident that the tetragonal phase-pure PT powders could be synthesized from the hydrothermal reactions conducted at 100°C for reasonable reaction times, *i.e.* 24 and 48 h in this study (Figure 1 and Figure 2), when the reaction mixtures were ultrasonicated for at least 1.5 h. The achievement of the phase-pure PT at this extraordinary low temperature has thus far never been reported. The application of an ultrasonic wave for an hour nonetheless seemed to be feasibly in affording the phase-pure PT, according to the PXRD pattern of the powder obtained from the 48 h reaction as shown in Figure 2(a) where the desired PT



was present as the major phase. Further experiments revealed that the purity of the obtained powders in this case was however rather ambiguous even when the hydrothermal reaction was prolonged for over 120 h, as shown in Figure 3. This indicated the significance of the ultrasonication in rendering the success of the hydrothermal synthesis of the phase-pure PT at the water boiling temperature. The ultrasonication of 6 h nonetheless led to the formation of other oxide phases instead of the desired PT when the hydrothermal reaction was conducted for 24 h (Figure 1). This was not the case when the reaction was prolonged for 48 h (Figure 2), suggesting the influences of the reaction time to overpower that of the ultrasonication.

Two observations can be made on the basis of the PXRD results. In the view of the ultrasonication time, it was apparent that the lengthy ultrasonication could reduce the hydrothermal reaction time affording the phase-pure PT powders. This suggests the promotion of the reaction activities by the ultrasonic wave, which may be due to (1) the reduced particle sizes of the starting

precursors and/or oxide intermediates caused by the local acoustic microjets, and (2) the better probability for nucleation induced by the formation of the confined hot spots. The important role of the ultrasonication in lessening the thermodynamic barrier and therefore increasing the reactivity of the hydrothermal reaction has therefore been underlined. In the aspect of the hydrothermal reaction time, a distinctly slow reaction rate can be presumed at 100°C. For the same ultrasonication duration of 1 and 3 h, the tetragonal phase-pure PT could be yielded hydrothermally in only 6 and 3.5 h at 130°C [10], but 72 and 24 h at 100°C. The hydrothermal reaction rate should therefore be governed mainly by the hydrothermal reaction temperature, which was well agreed with that reported previously [10].

The obtained PT powders could be well refined in tetragonal  $P4/mmm$  (JCPDS 6-0425) with  $a = 3.8940(41)$ - $3.9000(43)$  Å, and  $c = 4.185(11)$ - $4.218(55)$  Å. The variation in ultrasonication time showed no distinct influences on the refined cell parameters and therefore the corresponding  $c/a$  ratios,

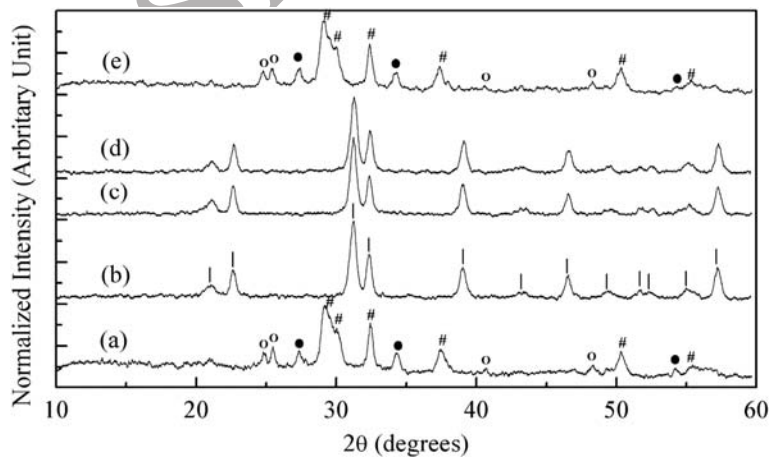


**Figure 1.** PXRD patterns of the particles obtained from the hydrothermal reactions conducted at 100°C for 24 h with prior ultrasonication for (a) 1 h (b) 1.5 h (c) 3 h (d) 4.5 h and (e) 6 h; | = tetragonal PT, # = non-stoichiometric PT, ● = TiO<sub>2</sub> rutile/anatase and ○ = Ti<sub>x</sub>O<sub>y</sub>.

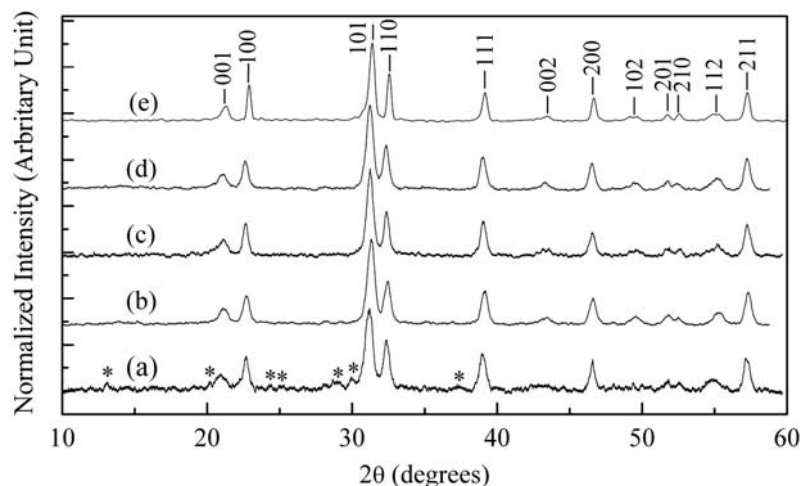


**Figure 2.** PXRD patterns of the particles obtained from the hydrothermal reactions conducted at 100°C for 48 h with prior ultrasonication for (a) 1 h (b) 1.5 h (c) 3 h (d) 4.5 h and (e) 6 h, where the asterisks indicate unidentified peaks.

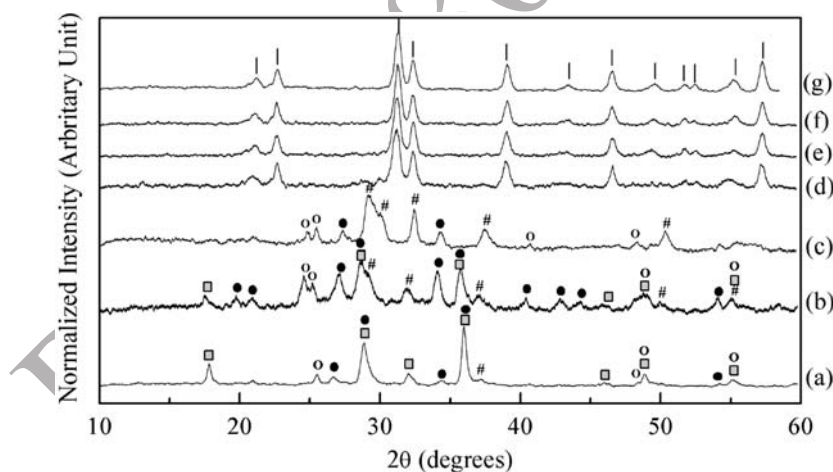


**Figure 3.** PXRD patterns of the particles obtained from the hydrothermal reactions conducted at 100°C for (a) 6 h (b) 12 h (c) 24 h (d) 48 h (e) 72 h (f) 120 h and (g) 124 h with the prior ultrasonication for an hour; | = tetragonal PT, # = non-stoichiometric PT, ● =  $\text{TiO}_2$  rutile/anatase, ○ =  $\text{Ti}_x\text{O}_y$  and ■ =  $\text{PbO}$ .

1.073(3)-1.083(2). These values were in good agreement with the values commonly yielded for the hydrothermally derived PT particles [2,3,10], but larger than those of the solid state reactions [12]. Regarding the interpretation of the PXRD results, although the presence of

other phases beside the desired PT (JCPDS 6-0425) in some cases was plain, the index of these phases to certain JCPDS could be ambiguous. These phases were therefore shown as groups of feasible phases in Figure 1 and Figure 3; #, ●, ○ and ■ were therefore

employed to represent lead titanates of other stoichiometry than  $\text{PbTiO}_3$ , a mixture of rutile and anatase  $\text{TiO}_2$ , various oxides of titanium, and different  $\text{PbO}$  phases, respectively.

The SEM images as typically illustrated

in Figure 4(a) showed the PT particles to be tetragonal in shape, which was well reflecting the crystallographic internal order, regardless of the synthetic conditions. Sizes of these particles were accordingly measured in two directions along the short and long axes from

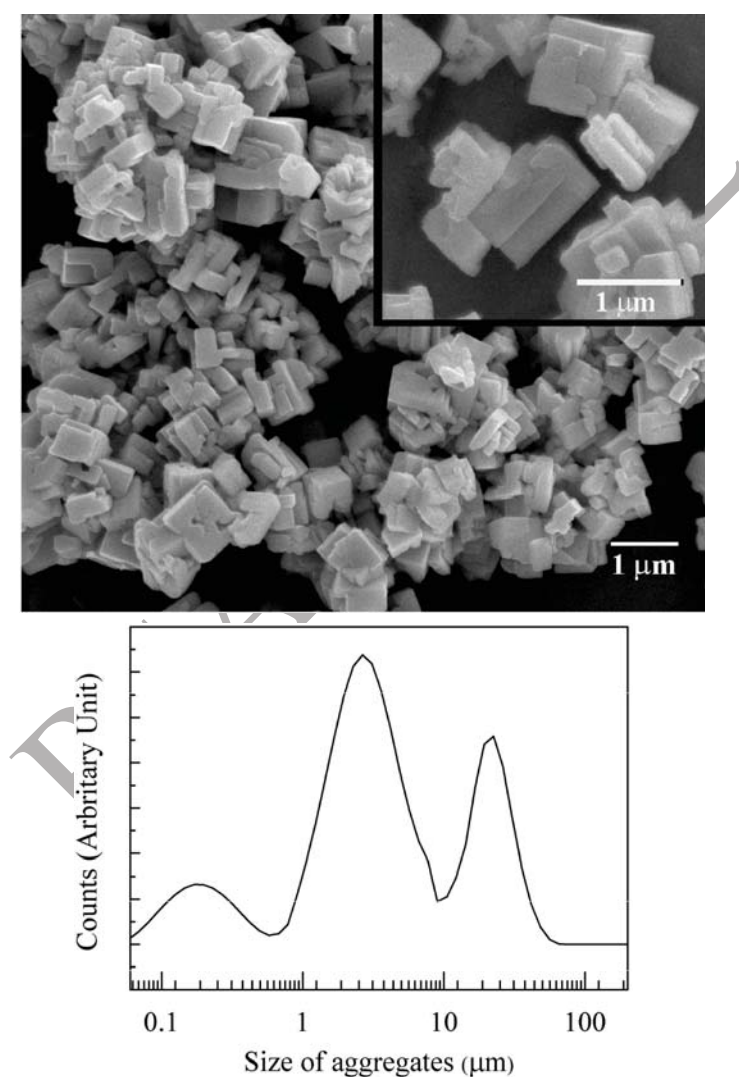


**Figure 4.** (a) Typical SEM image the PT aggregates obtained from the reaction conducted at 100°C for 48 h with 4.5 h ultrasonication with the magnified image to illustrate the layer-by-layer growth of the particle in the inset, and (b) the corresponding tri-nodal aggregate size distribution.

the SEM images, and summarized in Table 1. Being independent of also the synthetic conditions, sizes of these particles were distributed regularly from few hundred nanometers to just over one micron, with most of the population distributed in the submicrometer region. The average sizes were *ca.* 500-600 nm alike. According to the SEM images, the PT particles were mostly present as hard aggregates, with the growth of small particles on the surfaces of the larger ones as exemplified in the inset of Figure 4(a). This observation could lead to the assumption of the layer-by-layer crystal growth model where the nucleation and growth of the new crystals

occur on the surfaces of the mature ones [13]. In spite of the variation in synthetic conditions, sizes of the PT aggregates disseminated in a similar tri-nodal fashion as typically illustrated in Figure 4(b), centering at *ca.* 0.20, 2.0 and 20  $\mu\text{m}$ . The mean aggregate sizes were rather similar, falling into a narrow range of *ca.* 5-8  $\mu\text{m}$ . There was no apparent correlation between the aggregate sizes and the ultrasonication time (Table 1). The prolongation of the hydrothermal reaction time nonetheless led to the enlargement of both the length of the particles and mean aggregate sizes. This should be due to the growth of the particle with the extended hydrothermal reaction time.

**Table 1.** Sizes of PT particles measured from the SEM images, and of the aggregates obtained from laser diffraction experiments.

Hydrothermal reaction time (h)	Ultrasonication time (h)	Particle sizes ( $\mu\text{m}$ )			Aggregate sizes ( $\mu\text{m}$ )	
		Short axis	Long axis	Average	D50	Mean
24	1.5	0.19-0.98	0.21-1.30	0.57	2.60(6)	6.14(1)
	3.0	0.16-1.00	0.35-1.62	0.65	1.99(4)	5.18(2)
	4.5	0.23-1.41	0.28-1.26	0.55	3.37(4)	7.59(3)
48	1.5	0.12-0.92	0.28-1.27	0.53	3.37(1)	9.23(7)
	3.0	0.15-1.28	0.17-1.69	0.48	2.72(6)	6.90(7)
	4.5	0.12-0.73	0.22-1.30	0.47	3.01(1)	7.65(2)
72	1	0.19-1.20	0.23-1.30	0.57	1.69(2)	6.05(6)
120		0.13-1.11	0.28-1.32	0.60	2.20(7)	6.54(2)
144		0.18-1.35	0.26-1.59	0.63	2.14(2)	6.73(6)

#### 4. CONCLUSIONS

In summary, the ultrasonication of the reaction mixture has been proved to be able to reduce the thermodynamic barrier in the synthesis of fine PT powders under hydrothermal conditions, and the sonocatalyzed hydrothermal concept was underlined. The tetragonal phase-pure PT could be achieved at an exceptionally low temperature of 100 °C for the first time, irrespective to the slow kinetic at this temperature. The

synthesized PT particles were tetragonal in shape and mostly submicrometers in sizes. These PT particles were in general comparable to those obtained at high reaction temperature either with or without the ultrasonication process. They were present mostly as hard aggregates of few micrometers. Under the studied conditions, the growth of the PT particles was manifestly occurred *via* the layer-by-layer mechanism.

# ACKNOWLEDGEMENTS

The Synchrotron Light Research Institute (Public Organization), the Thailand Research Fund and the Thailand Toray Science Foundation (TTSF) are acknowledged for financial support. Chaiyos Chankaew thanks also to the Graduate School of Chiang Mai University for Graduate Scholarship.

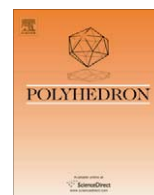
# REFERENCES

- [1] Byrappa K. and Yoshimura M., *Handbook of Hydrothermal Technology: A Technology for Crystal Growth and Materials Processing*, Noyes Publication, New Jersey, 2001.
- [2] Rujiwattra A., Jongphipphan J. and Ananta S., Stoichiometric synthesis of tetragonal phase pure lead titanate under mild chemical conditions employing NaOH and KOH, *Mater. Lett.*, 2005; **59**: 1871–1875.
- [3] Rujiwattra A., Thammajak N., Sarakonstri T., Wongmaneerung R. and Ananta S., Influence of alkali reagents on phase formation and crystal morphology of hydrothermally derived lead titanate, *J. Cryst. Growth*, 2006; **289**: 224-230.
- [4] Moulson A.J. and Herbert J.M., *Electroceramics: Materials, Properties, Applications*, 2nd Edn., Wiley, New York, 2003.
- [5] Xu Y., *Ferroelectric Materials and Their Applications*, North-Holland, New York, 1991.
- [6] Jona F. and Shirane G., *Ferroelectric Crystals*, Dover Publications, New York, 1993.
- [7] Udomporn A., Pengpat K. and Ananta S., Highly dense lead titanate ceramics from refined processing, *J. Eur. Ceram. Soc.*, 2004; **24**: 185-188.
- [8] Tartaj J., Fernandez J.F. and Villafuerte-Castrejon F.M.E., Preparation of  $\text{PbTiO}_3$  by seeding-assisted chemical sol-gel, *Mater. Res. Bull.*, 2001; **36**: 479-486.
- [9] Fang J., Wang J., Gan L.M. and Ng S.C., Comparative study on phase development of lead titanate powders, *Mater. Lett.*, 2002; **52**: 304-312.
- [10] Rujiwattra A., Wongtaewan C., Pinyo W. and Ananta S., Sonocatalyzed hydrothermal preparation of lead titanate nanopowders, *Mater. Lett.*, 2007; **61**: 4522–4524.
- [11] Tapala S., Thammajak N., Laorattanakul P. and Rujiwattra A., Effects of microwave heating on sonocatalyzed hydrothermal preparation of lead titanate nanopowders, *Mater. Lett.*, 2008; **62**: 3685-3687.
- [12] Wongmaneerung R., Yimnirun R. and Ananta S., Effect of vibro-milling time on phase formation and particle size of lead titanate nanopowders, *Mater. Lett.*, 2006; **60**: 1447-1452.
- [13] Chen X., Fan H. and Liu L., Synthesis and crystallization behavior of lead titanate from oxide precursors by a hydrothermal route, *J. Cryst. Growth*, 2005; **284**: 434-439.



Contents lists available at ScienceDirect

Polyhedron

journal homepage: [www.elsevier.com/locate/poly](http://www.elsevier.com/locate/poly)

# Microwave synthesis and crystal structures of two cobalt-4,4'-bipyridine-sulfate frameworks constructed from 1-D coordination polymers linked by hydrogen bonding

Timothy J. Prior<sup>a,\*</sup>, Bunlawee Yotnoi<sup>b</sup>, Apinpus Rujiwatra<sup>b</sup>

<sup>a</sup> Department of Chemistry, University of Hull, Kingston upon Hull, HU6 7RX, UK

<sup>b</sup> Department of Chemistry, Faculty of Science, Chiang Mai University, Chiang Mai 50200, Thailand

## ARTICLE INFO

### Article history:

Received 27 July 2010

Accepted 19 October 2010

Available online 26 October 2010

### Keywords:

Cobalt

Bipyridine

Sulfate

Framework

Template

Microwave

## ABSTRACT

Two extended solids displaying both one-dimensional coordination polymer and two-dimensional hydrogen-bonded structural features has been prepared under microwave-assisted hydrothermal conditions.  $[\text{Co}(\text{H}_2\text{O})_4(4,4'\text{-bipyridine})](4,4'\text{-bipyridineH}_2)\cdot 2(\text{SO}_4)\cdot 2\text{H}_2\text{O}$  (**1**) contains one-dimensional coordination polymer chains of composition  $[\text{Co}(4,4'\text{-bipyridine})(\text{H}_2\text{O})_4]^{2+}_n$  that are linked into a three dimensional framework by hydrogen bonding through uncoordinated sulfate and water. Within this framework is located a twice protonated 4,4'-bipyridine molecule ( $\text{C}_{10}\text{N}_2\text{H}_{10}^{2+}$ ) which forms two short  $\text{N}\cdots\text{H}\cdots\text{O}$  hydrogen bonds and eight further non-classical  $\text{C}\cdots\text{H}\cdots\text{O}$  interactions. The close approach of guest and framework and the large number of interactions between them suggest the cation is important in templating this phase.

$[\text{Co}_2(4,4'\text{-bipyridine})_2(\text{SO}_4)_2(\text{H}_2\text{O})_6]\cdot 4(\text{H}_2\text{O})$  (**2**) displays one dimensional chains of cobalt-bipyridine which are sinusoidal in nature. Two sets of these chains run parallel to the crystallographic  $[2\ 1\ 2]$  and  $[\bar{2}\ 1\ \bar{2}]$  directions. Two-dimensional hydrogen-bonded sheets parallel to the  $xz$  plane link these; further hydrogen bonds to uncoordinated water help to form a three-dimensional honeycomb network with the centroids of the six-membered rings aligned parallel to the  $a$ -axis.

The use of microwave synthesis for framework solids of this type is described and the structures of the frameworks and the interactions responsible for their assembly are discussed. The thermal and spectroscopic behaviour of the two phases are described.

© 2010 Elsevier Ltd. All rights reserved.

## 1. Introduction

Historically, the best known of the framework solids were the naturally-occurring aluminosilicate zeolites which have extended structures based on tetrahedra [1]. The synthesis of artificial zeolites led to a huge interest in the synthesis of other phases based on tetrahedra such as the aluminophosphates and gallophosphates [2]. The basic technique for directing the formation of these phases is to utilise suitable sources of metal and non-metal with a so-called structure directing agent (a template), typically a quaternary amine. The size, shape, and charge of this template are all important in determining the nature of the framework obtained [3,4]. In some examples the hydrogen-bonding propensity of the template was also shown to be important [5].

There has been considerable interest in simulating and expanding upon the structures displayed by the aluminosilicate zeolites and other oxide frameworks through the construction of metal-

organic frameworks (MOFs) [6,7]. The different range of metal–ligand interactions and other parameters, such as metal co-ordination, ligand geometry and co-ordination preference, have produced chemistry in MOFs which is not known for classical framework solids [8]. In particular, structural design in MOFs is now well-established [9,10]. This chemistry has generated a huge range of novel structures with potentially useful properties, for example, porosity [11], chirality [12], selective sorption [13], gas storage [14–16], catalysis [17], non-linear optical properties [18], and guest-responsive magnetism [19]. Some examples exist where MOFs have been templated by a specific guest species [20–22]. For example, naphthalene has been shown to have a profound influence on the structures of frameworks constructed from  $\text{Ni}^{2+}$  with 1,3,5-benzenetricarboxylate and 4,4'-bipyridine [23].

In the construction of MOFs, assembly of the structural building units is by strong co-ordinative covalent bonds. In many MOF examples, weaker interactions such as classical (e.g.  $\text{O}\cdots\text{H}\cdots\text{O}$ ) [24] and non-classical [25] (e.g.  $\text{C}\cdots\text{H}\cdots\text{O}$ ) hydrogen bonding interactions are present as secondary structural components [26]. Examples are also emerging where there are genuinely two distinct

\* Corresponding author. Tel.: +44 (0)1482466389; fax: +44 (0)1482466410.

E-mail address: [t.prior@hull.ac.uk](mailto:t.prior@hull.ac.uk) (T.J. Prior).



structural units including a coordination polymer and a hydrogen-bonded architecture [26–29].

One of the most widely studied linear bidentate ligands is 4,4'-bipyridine (4,4'-bipy) which is found in a very great number of MOFs, with examples extending from 1-D to 2-D and 3-D architectures [30]. The inflexibility of the ligand along its long axis and the predictable coordination chemistry make the ligand a very attractive framework-former, both on its own and with auxiliary ligands. For example, a hybrid framework,  $[\text{Co}_2(4,4'\text{-bipy})_3(\text{SO}_4)_2(\text{H}_2\text{O})_2](4,4'\text{-bipy})(\text{CH}_3\text{OH})$ , in which both 4,4'-bipy and sulfate act as framework-forming ligands has been reported [31]. This compound displays remarkable, reversible, behaviour upon dehydration; unbound encapsulated 4,4'-bipy becomes involved in the formation of a new framework when coordinated water is removed. Sulfate is found as a framework former in many examples with linear dipyrindines. It has diverse coordination chemistry to transition metal ions, sometimes displaying more than one coordination mode in a single framework [32]. Sulfate is also a very suitable anion for the construction of hydrogen-bonded networks because it readily forms strong hydrogen bonds [33].

In our study, we sought to combine the ability of 4,4'-bipy to form coordination polymers with the strong (classical) hydrogen bonding properties of the sulfate anion to produce solids which featured both coordination polymer and hydrogen-bonding motifs in the extended structures. Our previous experience of this system suggested it would be important that the pH of the solution and the amount of water present were carefully controlled [34] to achieve this aim, so that other previously observed phases were not formed [31,35–37].

Hydrothermal synthesis is one widely exploited route for crystal growth of MOFs and this typically takes days or weeks to generate crystals of an appropriate size for diffraction experiments. Despite the great success of microwave heating in organic synthesis [38], the application of this technique to inorganic materials is poorly developed. Recently, microwave-assisted hydrothermal chemistry has been utilised in the crystal growth of MOFs [39,40]. The microwave heating helps to shorten the reaction time to minutes [41]. Here, microwave-assisted hydrothermal synthesis was employed in growing crystals of two new extended metal-organic frameworks. The two extended solids have both coordination polymer and hydrogen-bonding structural features. Intriguingly though, one of these solids is assembled around a twice-protonated 4,4'-bipy molecule which appears to act as a template. The other has a much more extensive 3-D hydrogen bonding arrangement.

## 2. Materials and methods

### 2.1. Microwave-assisted hydrothermal crystal growth

Each reaction was conducted using a tightly closed Teflon container under an autogenous pressure generated at 630 W for 5 min using a domestic microwave oven (Whirlpool XT – 25ES/S, 900 W, 2.45 GHz). The pH of each mixture was measured using universal pH strips (Merck, 1.09535.0001), and in each case there was no change in the pH of the mixture after the reaction. Crystalline products were separated from supernatant, washed with deionized water and dried in air. In each case the solid products had a uniform appearance under magnification and the chemical analysis described in Sections 3.2 and 3.3 show these are single phase products. The yield of each reaction was of the order of 30%.

**Reaction A:** Pale pink needles were grown from the mixture of 0.1395 g cobalt(II) nitrate hexahydrate ( $\text{Co}(\text{NO}_3)_2 \cdot 6\text{H}_2\text{O}$ , 98% Aldrich), 0.4475 g 4,4'-bipyridine ( $\text{C}_{10}\text{H}_8\text{N}_2$ , 99% Fluka) and sulphuric

acid ( $\text{H}_2\text{SO}_4$ , 98% Merck) in 9.50 g of deionized water. (Co:bipy:sulfate:water molar ratio = 1:6:1:1128) The initial pH of the solution was 6.

**Reaction B:** Pale orange sagittate crystals of  $[\text{Co}(\text{H}_2\text{O})_4(4,4'\text{-bipy})](4,4'\text{-bipyH}_2) \cdot 2(\text{SO}_4) \cdot 2\text{H}_2\text{O}$  (**1**) were grown from the mixture of 0.1400 g cobalt(II) nitrate hexahydrate, 0.4502 g 4,4'-bipyridine and 0.0923 g sulphuric acid in 9.50 g of deionized water. (Co:bipy:sulfate:water molar ratio = 1:6:2:1100) The initial pH of the solution was 4.

**Reaction C:** Pink acicular crystals of  $[\text{Co}_2(4,4'\text{-bipy})_2(\text{SO}_4)_2(\text{H}_2\text{O})_6] \cdot 4(\text{H}_2\text{O})$  (**2**) were grown from the mixture of 0.3299 g cobalt(II) sulphate heptahydrate ( $\text{Co}(\text{SO}_4)_2 \cdot 7\text{H}_2\text{O}$ , 99% Fluka) and 0.1833 g 4,4'-bipyridine in 9.50 g of deionized water. (Co:bipy:sulfate:water molar ratio = 1:1:2:454) The pH of the mixture was 6. No further attempt was performed to vary the pH of the mixture.

### 2.2. X-ray diffraction structure determination

Routine data collection and structure solution procedures were adopted. Data were collected in series of  $\omega$ -scans using a Stoe IPDS2 diffractometer. Full matrix least squares refinement against  $F^2$  was employed for structure refinement. Crystals of each phase displayed a tendency to form aggregates. This may prove to be a general feature of microwave hydrothermal synthesis [42]. The crystal of **2** examined was found to be subject to non-merohedral twinning which was dealt with using the program ROTAX [43]. Use of this and omission of a few partially overlapped reflections yielded a vast improvement in the quality of the final structure. Final residual electron density maxima and minima were improved thus: initially 4.11 and  $-0.943 \text{ e } \text{\AA}^{-3}$ ; after treatment these were 0.564 and  $-0.564 \text{ e } \text{\AA}^{-3}$  (*sic*).

For each structure the final data were of good quality and hydrogen atoms were located from difference Fourier maps. Hydrogen atoms attached to 4,4'-bipyridine were refined using a riding model. Those of water were located in difference Fourier maps and refined with sensible restraints. A small portion of disorder within the crystal structure of **2** was modelled using standard techniques. Full details of data collection, treatment of twinning, and the modelling of disorder are contained in the Supplementary Information.

### 2.3. Spectroscopic studies of **1** and **2**

The Fourier-transform IR spectra of the ground crystals of **1** and **2** were recorded using a Bruker Tensor 27 FT-IR instrument ( $4000\text{--}400 \text{ cm}^{-1}$ , resolution  $0.5 \text{ cm}^{-1}$ ) using KBr (BDH 98.5%) disks. Raman spectra were collected using a HORIBA JOBIN YVON T64000 spectrophotometer, employing the 514.5 nm line of an Ar laser excitation source with 0.5 mW at the sample for a total integration time of 120 s. The UV-Vis spectra of **1** and **2** were collected on both the aqueous solution and the suspension in hexane at room temperature from 200 nm to 800 nm using UV-1800 spectrophotometer (Shimadzu, Japan).

## 3. Results and discussion

### 3.1. Microwave synthesis

Although the microwave-assisted hydrothermal process is not new, examples of the application of the process in growing single crystals of MOFs are limited. Here the process was successfully applied for the rapid synthesis of single crystals of two new phases in the cobalt-4,4'-bipy-sulfate-water system. In each case the reaction duration was only 5 min, in contrast to traditional hydrothermal chemistry reactions lasting days. The reaction products are



<b>Reaction A – initial pH = 6</b>	<b>CoSO<sub>4</sub>(H<sub>2</sub>O)<sub>3</sub>(4,4'-bipy).2H<sub>2</sub>O</b> <sup>35</sup>
Co:bipy:sulfate:water molar ratio = 1:6:1:1128	
<b>Reaction B – initial pH = 4</b>	<b>[Co(H<sub>2</sub>O)<sub>4</sub>(4,4'-bipy)].(4,4'-bipyH<sub>2</sub>).2(SO<sub>4</sub>).2H<sub>2</sub>O</b>
Co:bipy:sulfate:water molar ratio = 1:6:2:1100 (compound 1)	
<b>Reaction C – initial pH = 6</b>	<b>[Co<sub>2</sub>(4,4'-bipy)<sub>2</sub>(SO<sub>4</sub>)<sub>2</sub>(H<sub>2</sub>O)<sub>6</sub>].4(H<sub>2</sub>O)</b>
Co:bipy:sulfate:water molar ratio = 1:1:2:454 (compound 2)	

Scheme 1. Reaction products.

summarised within Scheme 1 below. During the synthesis it was found that the nature of the product obtained was very sensitive to the initial pH; no crystalline products were obtained where the initial pH of the mixture was lower than 4. If the reaction is too acidic, the 4,4'-bipy present should all be protonated and thus not available for coordination. Reaction A (pH 6) yielded crystals of the phase CoSO<sub>4</sub>(H<sub>2</sub>O)<sub>3</sub>(4,4'-bipy).2H<sub>2</sub>O which has been reported before [35]. Reaction B (pH 4) rapidly yielded pale orange sagittate crystals that were shown by X-ray diffraction to be an unknown phase, hereafter labelled **1**. A third synthesis (Reaction C) with subtly different initial conditions yielded compound **2**.

### 3.2. Bipyridinium-templated phase, **1**

This compound crystallises in the centrosymmetric space group *P*2<sub>1</sub>/*n* (number 14) with a single Co<sup>2+</sup> ion within the asymmetric

unit located on a 4e Wyckoff position. Crystal data and basic refinement information is contained within Table 1. The chemical formula for **1** is best expressed as [Co(H<sub>2</sub>O)<sub>4</sub>(4,4'-bipy)](4,4'-bipyH<sub>2</sub>).2(SO<sub>4</sub>).2H<sub>2</sub>O and in this formulation the diprotonated 4,4'-bipy may be regarded as an occluded cation which is enclosed within an anionic framework composed of 1-D coordination polymer extended into 3-D by hydrogen bonding of sulfate and water. The asymmetric unit is depicted in Fig. 1. Full crystal structure data are included within the Supplementary Information. The composition of a bulk sample of **1** was determined by chemical analysis and this demonstrated a good fit between the calculated and observed compositions. Percentage C/H/N composition was as follows; *Anal.* Calc.: C, 35.78; H, 4.51; N, 8.35. Found: C, 35.63; H, 4.45; N, 8.31%.

Each Co<sup>2+</sup> adopts pseudo-octahedral coordination and is surrounded by four water molecules in a square plane and furthermore by two trans 4,4'-bipy molecules, the first of which binds

**Table 1**  
Summary of crystal and refinement data for **1** and **2**.

Identification code	<b>1</b>	<b>2</b>
Structural formula	[Co(H <sub>2</sub> O) <sub>4</sub> (4,4'-bipy)](4,4'-bipyH <sub>2</sub> ).2(SO <sub>4</sub> ).2H <sub>2</sub> O	[Co(H <sub>2</sub> O) <sub>3</sub> (SO <sub>4</sub> )(4,4'-bipy) <sub>2</sub> ] <sub>2</sub> Co(H <sub>2</sub> O) <sub>4</sub> Co(H <sub>2</sub> O) <sub>2</sub> (SO <sub>4</sub> ) <sub>2</sub> .8H <sub>2</sub> O
Empirical formula	C <sub>20</sub> H <sub>30</sub> CoN <sub>4</sub> O <sub>14</sub> S <sub>2</sub>	C <sub>20</sub> H <sub>36</sub> Co <sub>2</sub> N <sub>4</sub> O <sub>18</sub> S <sub>2</sub>
Formula weight	673.54	802.52
Temperature (K)	150(2)	150(2)
Wavelength (Å)	0.71073	0.71073
Crystal system	monoclinic	monoclinic
Space group	<i>P</i> 2 <sub>1</sub> / <i>n</i>	<i>P</i> 2 <sub>1</sub> / <i>c</i>
Unit cell dimensions		
<i>a</i> (Å)	9.4120(18)	7.4347(5)
<i>b</i> (Å)	13.0143(13)	40.573(4)
<i>c</i> (Å)	22.155(3)	11.4833(8)
$\alpha$ (°)	90	90
$\beta$ (°)	97.943(13)	117.405(5)
$\gamma$ (°)	90	90
Volume (Å <sup>3</sup> )	2687.8(7)	3075.2(4)
<i>Z</i>	4	4
<i>D</i> <sub>calc</sub> (mg/m <sup>3</sup> )	1.664	1.733
Absorption coefficient (mm <sup>-1</sup> )	0.872	1.301
<i>F</i> (0 0 0)	1396	1656
Crystal size (mm <sup>3</sup> )	0.35 × 0.14 × 0.12	0.4 × 0.1 × 0.1
$\theta$ Range for data collection (°)	3.09–26.14	2.01–27.13
Index ranges	–11 ≤ <i>h</i> ≤ 11 0 ≤ <i>k</i> ≤ 16 0 ≤ <i>l</i> ≤ 27	0 ≤ <i>h</i> ≤ 9 –51 ≤ <i>k</i> ≤ 51 –14 ≤ <i>l</i> ≤ 13
Reflections collected	5150	6320
Independent reflections	5150 [ <i>R</i> <sub>int</sub> = 0.068]	6320 [ <i>R</i> <sub>int</sub> = 0.048]
Completeness to $\theta$ = 26.00°	95.8%	94.0%
Absorption correction	analytical	analytical
Maximum and minimum transmission	0.8324 and 0.6966	0.9624 and 0.8381
Refinement method	full-matrix least-squares on <i>F</i> <sup>2</sup>	full-matrix least-squares on <i>F</i> <sup>2</sup>
Data/restraints/parameters	5150/22/408	6320/235/474
Goodness-of-fit on <i>F</i> <sup>2</sup>	1.087	1.091
Largest difference in peak and hole (e Å <sup>-3</sup> ) (sic)	0.729 and –0.594	0.564 and –0.564
Final <i>R</i> indices [ <i>I</i> > 2 $\sigma$ ( <i>I</i> )]	<i>R</i> <sub>1</sub> = 0.0683, <i>wR</i> ( <i>F</i> <sup>2</sup> ) = 0.2381	<i>R</i> <sub>1</sub> = 0.0559, <i>wR</i> ( <i>F</i> <sup>2</sup> ) = 0.1514
<i>R</i> indices (all data)	<i>R</i> <sub>1</sub> = 0.1105, <i>wR</i> ( <i>F</i> <sup>2</sup> ) = 0.2469	<i>R</i> <sub>1</sub> = 0.0832, <i>wR</i> ( <i>F</i> <sup>2</sup> ) = 0.1566

Where  $R_1 = \frac{\sum |F_o| - |F_c|}{\sum |F_o|}$ ,  $wR(F^2) = \sqrt{\frac{\sum w(F_o^2 - F_c^2)^2}{\sum wF_o^4}}$  and *F*<sub>o</sub> and *F*<sub>c</sub> are the observed and calculated structure factors for each reflection and *w* is the weight for each reflection.

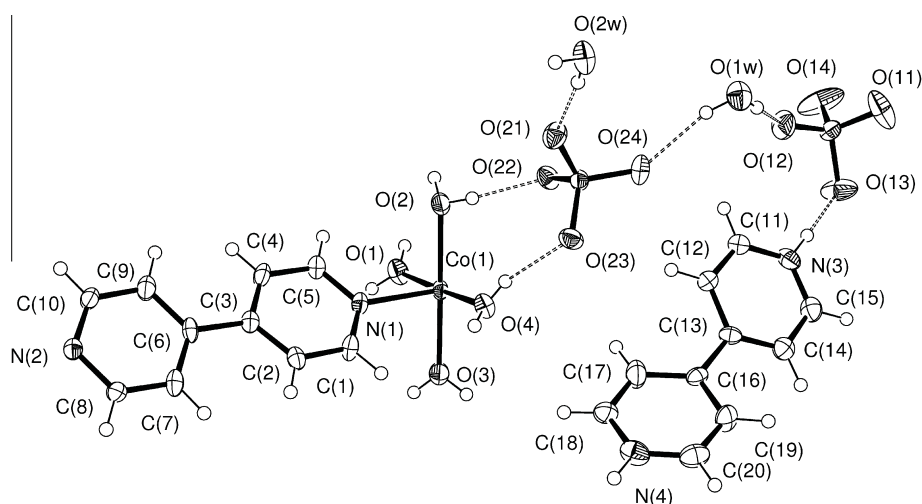


**Fig. 1.** ORTEP representation of the asymmetric unit of **1**. Atoms are drawn as 50% thermal ellipsoids. Only non-hydrogen atoms are labelled for clarity. Selected bonds lengths (in Å): Co1–O1 2.075(7); Co1–O2 2.109(6); Co1–O3 2.062(7); Co1–O4 2.112(6); Co1–N2' 2.154(6); Co1–N1 2.155(6); S1–O11 1.426(9); S1–O12 1.438(7); S1–O14 1.460(8); S1–O13 1.490(7); S2–O21 1.465(7); S2–O22 1.491(6); S2–O23 1.477(6); S2–O24 1.453(6). Symmetry equivalent atom generated by the operator (i)  $x - \frac{1}{2}, -y + \frac{1}{2}, z - \frac{1}{2}$ .

through N1, while the second binds through N2 and is generated from the first by the symmetry operator  $x - \frac{1}{2}, \frac{1}{2} - y, z - \frac{1}{2}$ . The  $\text{Co}^{2+}$  and 4,4'-bipy therefore form a one-dimensional chain which runs parallel to the crystallographic  $[1\ 0\ 1]$  direction. There is a little twisting of the 4,4'-bipy about the central C–C bond; the angle between the mean planes of the two six-membered rings is  $10.36(10)^\circ$ . This chain is illustrated in Fig. 2. The 1-D linear chain is an important motif in metal-bipyridine frameworks; there are a large number of MOFs based on this arrangement [30]. The arrangement of metal and 4,4'-bipy in **1** is typical of this type of chain. Co–N distances are in good agreement with those of similar frameworks [44]. The angle subtended by the bipyridine molecules at the  $\text{Co}^{2+}$  is  $178.9(3)^\circ$ . There are two unbound sulfate anions in the asymmetric unit and these are located such that four sulfates are arranged around the  $\text{Co}^{2+}$  ion forming hydrogen bonds to the four water molecules bound in a square plane with O...O hydrogen bond distances indicative of relatively strong hydrogen bonds (Table 2). The hydrogen bonds formed to each sulfate have the effect of linking together the 1-D coordination polymer chains; each

sulfate is involved in bridging between the  $\text{Co}(\text{H}_2\text{O})_4$  square planes to form infinite 2-D hydrogen-bonded sheets in the  $xy$  plane. Each of the 1-D cobalt-bipyridine polymer chains cuts this plane at any angle of  $61.37^\circ$ . Fig. 3 illustrates the interaction between the cobalt centres and each sulfate. Two sulfate molecules (central atom S1) form an embrace with multiple hydrogen bonds while for the second sulfate (central atom S2) a centrosymmetric  $R_4^2(8)$  embrace is observed and this is augmented by other hydrogen bonds.

Located between these sulfate anions are two further symmetry independent water molecules. These two unbound water molecules act as hydrogen bond donors to the sulfate anions. Short O–H...O interactions form infinite sulfate–water–sulfate chains which run parallel to the  $[1\ 0\ 1]$  direction (illustrated in the Supplementary Information). These chains run parallel to the cobalt-bipyridine 1-D chain and reinforce the bonding in this direction. Finally, contained between the chains is located twice protonated 4,4'-bipy ( $\text{C}_{10}\text{H}_{10}\text{N}_2^{2+}$ ). This cation forms a remarkable set of contacts to the framework and to sulfate, which are detailed in Table 2. Each protonated pyridine function forms one hydrogen

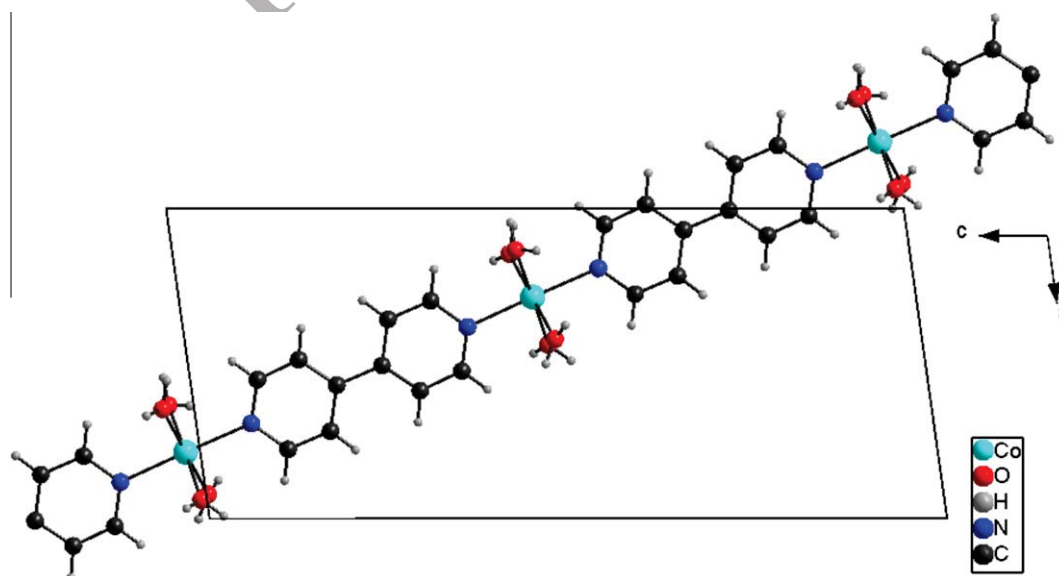


**Fig. 2.** Illustration of the one-dimensional coordination polymer chain within **1** that has composition  $[\text{Co}(4,4'\text{-bipyridine})(\text{H}_2\text{O})_4]^{2+}$ .

**Table 2**

Details of the classical hydrogen bonds and C–H···O interactions in **1**. A hydrogen bond donor is signified as D–H, where D is the donor atom. The hydrogen bond acceptor atom is labelled A.

Hydrogen bond donor (D–H)	D–H bond length (Å)	H···A distance (Å)	D–H···A angle (°)	D···A distance (Å)	Acceptor atom (A) [symmetry operator]
O1–H1A	0.83(4)	1.82(8)	173(7)	2.645(12)	O14 [ $x + 1/2, -y + 1/2, z + 1/2$ ]
O1–H1B	0.86(4)	1.89(5)	165(8)	2.735(10)	O2W [ $-x, -y + 1, -z + 1$ ]
O2–H2A	0.82(4)	1.88(7)	168(8)	2.674(9)	O22
O2–H2B	0.85(4)	1.93(6)	169(10)	2.773(10)	O21 [ $-x, -y + 1, -z + 1$ ]
O3–H3A	0.80(4)	1.97(8)	157(8)	2.729(10)	O13 [ $x + 1/2, -y + 1/2, z + 1/2$ ]
O3–H3B	0.84(4)	2.08(8)	173(11)	2.919(12)	O11 [ $-x + 1/2, y - 1/2, -z + 1/2$ ]
O3–H3B	0.84(4)	2.47(8)	126(8)	3.048(10)	O13 [ $-x + 1/2, y - 1/2, -z + 1/2$ ]
O4–H4A	0.76(4)	2.05(8)	155(8)	2.755(9)	O23
O4–H4B	0.82(4)	2.02(8)	160(8)	2.807(9)	O23 [ $-x + 1, -y + 1, -z + 1$ ]
O1W–H1X	0.85(4)	2.01(9)	166(10)	2.845(9)	O24
O1W–H1Y	0.80(4)	2.00(8)	165(8)	2.782(10)	O12
O2W–H2X	0.86(5)	1.89(5)	173(11)	2.746(10)	O21
O2W–H2Y	0.81(5)	2.19(9)	151(10)	2.933(12)	O11 [ $x + 1/2, -y + 3/2, z + 1/2$ ]
O2W–H2Y	0.81(5)	2.49(8)	150(8)	3.222(13)	O14 [ $x + 1/2, -y + 3/2, z + 1/2$ ]
N3–H3C	0.88	1.712	177	2.592(11)	O13
N4–H4C	0.88	1.791	162	2.641(10)	O22 [ $x + 1, y, z$ ]
C7–H7	0.95	2.57	163	3.487(11)	O1W [ $1 + x, y, z$ ]
C11–H11	0.95	2.54	124	3.167(12)	O12 [ $1/2 - x, 1/2 + y, 1/2 - z$ ]
C12–H12	0.95	2.46	125	3.110(11)	O24 [ $1/2 - x, 1/2 + y, 1/2 - z$ ]
C14–H14	0.95	2.52	143	3.329(13)	O14 [ $3/2 - x, 1/2 + y, 1/2 - z$ ]
C15–H15	0.95	2.33	147	3.168(11)	O2W
C18–H18	0.95	2.49	153	3.367(11)	O21 [ $1/2 + x, 1/2 - y, 1/2 + z$ ]
C19–H19	0.95	2.42	137	3.181(12)	O12 [ $3/2 - x, 1/2 + y, 1/2 - z$ ]
C20–H20	0.95	2.44	134	3.176(12)	O24 [ $3/2 - x, 1/2 + y, 1/2 - z$ ]

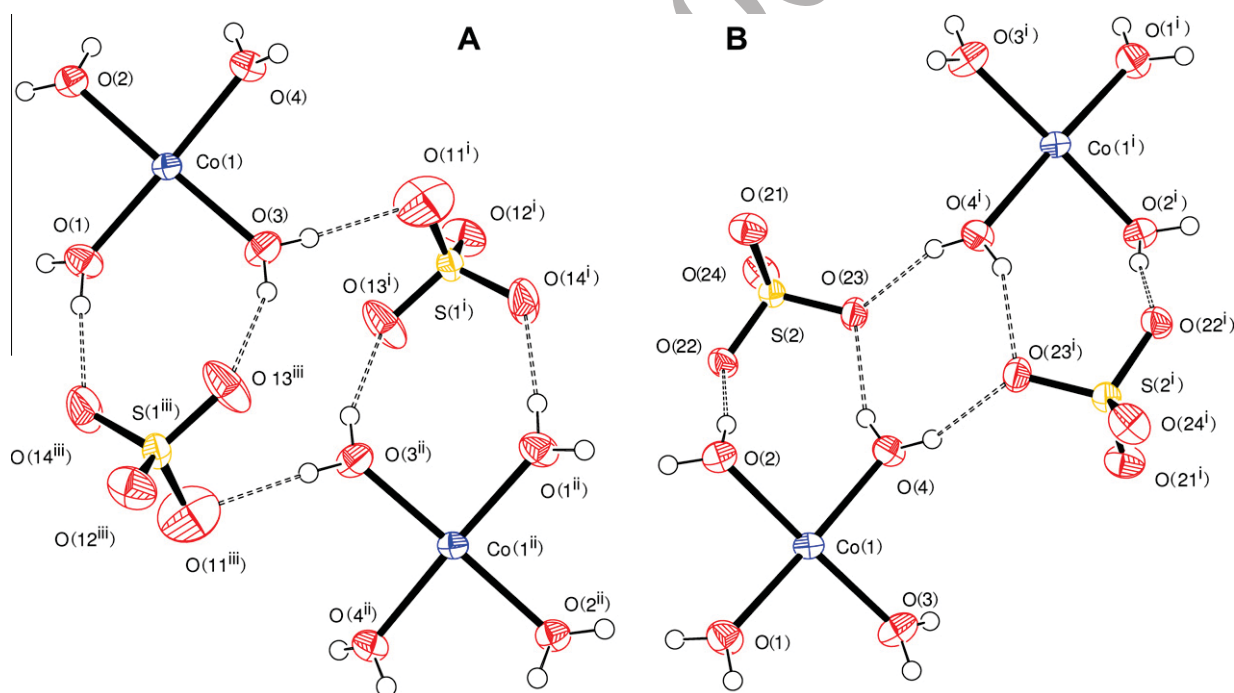


**Fig. 3.** (A) Hydrogen bonding of sulfate (S1) linking two  $\text{Co}(\text{H}_2\text{O})_4$  units. Symmetry equivalent atoms are generated by the symmetry operations: (i)  $0.5 - x, y - 0.5, 0.5 - z$ ; (ii)  $1 - x, -y, 1 - z$ ; (iii)  $0.5 + x, 0.5 - y, 0.5 + z$ . (B) Augmented  $R_4^2(8)$  embrace between two  $\text{Co}(\text{H}_2\text{O})_4$  units mediated by sulfate (S2). Symmetry equivalent atoms are generated by the symmetry operation: (i)  $1 - x, 1 - y, 1 - z$ .

bond (through N3 and N4) to sulfate and there are supplementary C–H···O interactions which hold the dication in place; for example there are six C–H···O contacts where the C···O distance is in the range 3.1–3.2 Å. These are in good agreement with other species containing this cation and somewhat shorter than many of those for uncharged 4,4'-bipy bound to a metal [44]. Alone, this is a relatively weak interaction, but the cumulative effect of six such interactions becomes important. The protonation of the 4,4'-bipy must play a role in strengthening these interactions through an additional coulombic interaction not present for uncharged

species. Interestingly the two rings of the diprotonated 4,4'-bipy are not coplanar with the angle between the mean planes of the two six-membered rings being  $29.9(2)^\circ$ . This rotation facilitates the formation of these non-classical hydrogen bonds by rotating the 4,4'-bipy towards the sulfate ions. The relatively short C–H···O distances promoted by protonation of the 4,4'-bipy, suggest this dication has a key role in templating **1**. The protonated 4,4'-bipy is crucial in filling space within the other network, but the close interaction with surrounding species suggests this acts as a template around which the framework assembles. Fig. 4 shows the

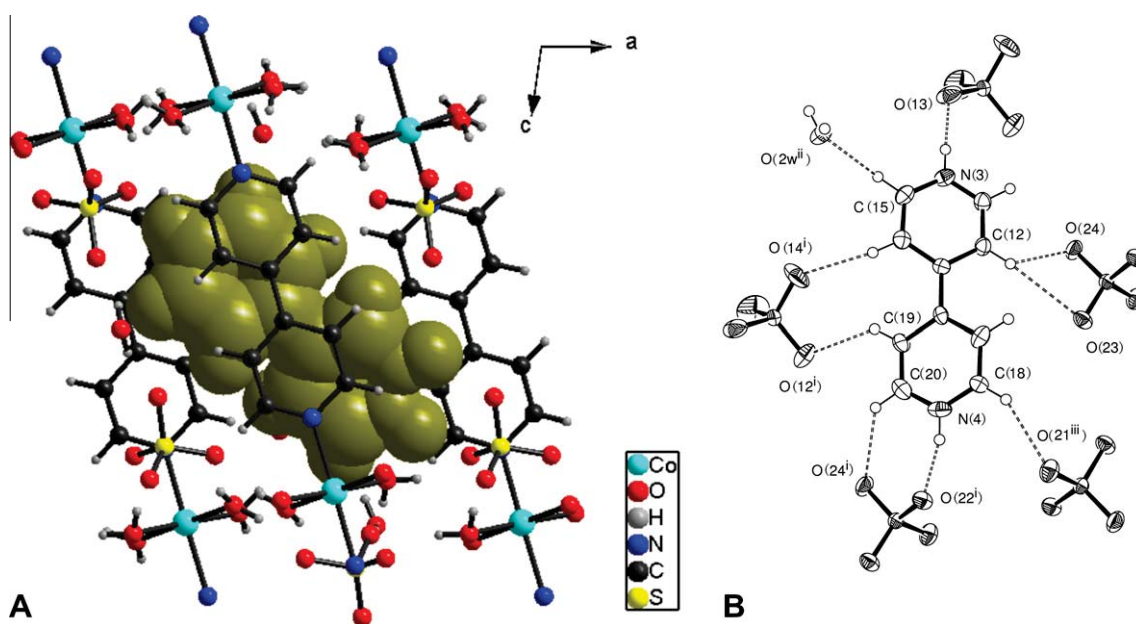


**Fig. 4.** (A) Space filling representation of the bipyridinium cation ( $C_{10}N_2H_{10}^{2+}$ ) occluded within the coordination polymer and hydrogen bonding framework. (B) ORTEP representation of the bipyridinium cation and the interactions it makes to the surrounding species. Short contacts which are indicative of favourable interactions are shown as dashed lines. Symmetry equivalent atoms are generated by the symmetry operations: (i)  $1 + x, y, z$ ; (ii)  $0.5 - x, y - 0.5, 0.5 - z$ ; (iii)  $1 - x, 1 - y, 1 - z$ .

location of the  $(4,4'\text{-bipyH}_2)^{2+}$  cation within the framework and the interactions between cation and framework. The role of the  $4,4'\text{-bipy}$  may be considered directly analogous to its role in templating the gallium oxyfluorophosphate DIPYR-GaPO [45]. The interaction between framework and twice protonated  $4,4'\text{-bipy}$  in the two phases is very similar when the hydrogen bonds between cation and framework are considered. The  $(4,4'\text{-bipyH}_2)^{2+}$  cation has been observed in similar phases before [20,21] but to our knowledge a detailed description of the interaction of this cation with a framework has not appeared.

The 1-D coordination polymer chain with composition  $M(H_2O)_4(4,4'\text{-bipy})$  is known in other examples [46,47], but this is the first example of any 1-D cobalt-bipyridine chain that is templated by  $(4,4'\text{-bipyH}_2)^{2+}$ . A similar compound containing manganese has recently been reported [48] but the description of the interaction of template and framework is rather scant. One similar example composed of chains of  $4,4'\text{-bipy}$  with  $Co^{2+}$  that contains a guest molecule is  $[Co(H_2O)_4(4,4'\text{-bipy})](SO_4) \cdot 3H_2O$  (PABA) (where PABA = para-aminobenzoic acid) [49]. This phase is less dense than **1** and has a greater cobalt to sulfate ratio but has similar structural features. However, the guest is uncharged and forms fewer short contacts with the framework than **1** suggesting a less important role in templating the framework. A similar example containing  $(4,4'\text{-bipyH}_2)^{2+}$  but with a framework composed  $Co^{2+}$  coordinated by both  $4,4'\text{-bipy}$  and 1,2,4,5-benzene-tetracarboxylate has been reported [50].

Data concerning the thermal behaviour of **1** are contained within the Supplementary Information. As **1** is heated under nitrogen, it decomposes in well-defined steps. First the coordinated and uncoordinated water is lost in the range 70–155 °C to form a species with approximate composition  $Co(4, 4'\text{-bipy})(4, 4'\text{-bipyH}_2)(SO_4)_2$ . This loses the template above 155 °C to form  $Co(4, 4'\text{-bipy})(SO_4H)_2$  at 270 °C. This is stable until 320 °C above which it decomposes to  $CoSO_4$ . The sulphate is stable up to 700 °C when it decomposes to  $Co_3O_4$ .

### 3.3. Sulfate-decorated coordination polymer, **2**

A second reaction with similar initial conditions to those used to generate **1** but employing a different source of sulfate (Reaction

C), and therefore the most basic reaction attempted, was found to yield pink needles of a compound with an unknown structure, hereafter **2**. Compound **2** crystallises in the centric space group  $P2_1/c$  with three independent  $Co^{2+}$  ions within the asymmetric unit, located on **4e**, **2a**, and **2c** Wyckoff positions. The chemical formula may be written in a short form as  $[Co_2(4,4'\text{-bipy})_2(SO_4)_2(-H_2O)_6] \cdot 4(H_2O)$  although this formulation does not elucidate the structure very effectively. It is more enlightening to write the composition of **2** as  $[Co(H_2O)_3(SO_4)(4,4'\text{-bipy})_2]_2Co(H_2O)_4Co(H_2O)_2(-SO_4)_2 \cdot 8H_2O$  where the coordination about each cobalt is more clearly defined. An ORTEP representation of the asymmetric unit is shown in Fig. 5 and basic crystal structure and refinement data are contained within Table 1. Full crystal structure data are included within the Supplementary Information. The composition of a bulk sample of **2** was determined by chemical analysis and this demonstrated a satisfactory fit between the calculated and observed compositions. Percentage C/H/N composition was as follows; *Anal. Calc.*: C, 30.67; H, 4.47; N, 7.01. *Found*: C, 29.91; H, 4.49; N, 6.98%.

The structure has many features in common with **1** but there are important differences. Compound **2** is a rather more dense phase than **1** and contains one-dimensional coordination polymer chains based on linear coordination of  $Co^{2+}$  by *trans*  $4,4'\text{-bipy}$  which is further decorated with coordinated water and sulfate. Importantly in **2**, there is no uncoordinated sulfate, but further uncoordinated water is found within the structure. Hydrogen bonding between the ligands (sulfate and water) and uncoordinated water forms a three dimensional honeycomb net which is in addition to the 1-D polymer.

Each  $Co^{2+}$  adopts pseudo-octahedral geometry, linking *trans*  $4,4'\text{-bipy}$  molecules to form a 1-D chain. The chain contains two symmetry independent  $4,4'\text{-bipy}$  molecules which display very similar geometry. The planes of the six-membered rings of each of the two  $4,4'\text{-bipy}$  molecules are twisted a little way from being parallel. The angles between the mean planes of the two sets of rings are 8.5(3)° and 9.3(3)°. The coordination environment about each of the three  $Co^{2+}$  ions is different and varies in the amount of bound sulfate. Coordination about Co1 is completed by three water molecules and one sulfate. The sulfate is disordered by



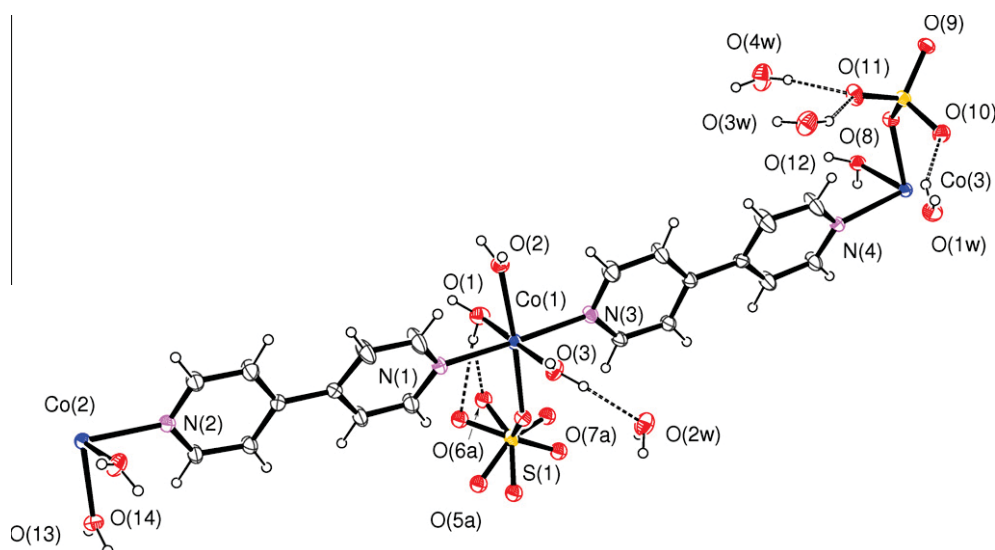


**Fig. 5.** ORTEP representation of the asymmetric unit of **2**. Atoms are drawn as 50% thermal ellipsoids. Carbon and hydrogen atoms have not been labelled to aid clarity. Similarly only the major orientation of the disordered sulfate is labelled. Selected bonds lengths (in Å): Co1–O1 2.030(6); Co1–O2 2.160(5); Co1–O3 2.032(6); Co1–N1 2.168(5); Co1–N3 2.180(5); Co1–O4 2.197(4); Co2–O13 2.127(5); Co2–O14 1.997(5); Co2–N2 2.168(5); Co3–O8 2.168(4); Co3–O12 2.068(5); Co3–N4 2.189(5); S1–O4 1.492(5); S1–O5A 1.488(5); S1–O6A 1.493(6); S1–O7A 1.475(5); S2–O8 1.491(5); S2–O9 1.479(5); S2–O10 1.484(5); S2–O11 1.462(5).

rotation about the S1–O4 bond. The two orientations which are approximately  $39.3^\circ$  apart are occupied in the ratio 82.1:17.9(5). Co2 resides on an inversion centre and coordination is completed by four bound water molecules. Similarly Co3 is located on an inversion centre, but is coordinated by two sulfate groups and two molecules of water in an 'all *trans*' arrangement. For Co2 and Co3 the N–Co–N angle is  $180^\circ$ , but for Co1, this angle is  $174.0(2)^\circ$ , possibly as a result of the greater steric demand of the sulfate group than the water molecule *trans* to it. The deviation from linearity that occurs at Co1 produces a sinusoidal form to the chain as shown in Fig. 6. This gentle curvature at Co1 is rather unusual in chains of this type. Examination of the Cambridge Structural Database [44] reveals a strong preference for a strictly linear coordination in transition metal compounds in which a metal cations links two 4,4'-bipy ligands in a *trans* arrangement. (See Supplementary Information) These infinite chains run parallel to the [2 1 2] direction and the sinusoidal variation has a wavelength of four 4,4'-bipy links which corresponds to a translation of  $(x+2, y+1, z+2)$ ; a distance of  $45.611(4)$  Å. Adjacent chains are related by a translation of  $(x+1, y, z+1)$ . A second set of identical chains related to the first by the symmetry operator  $-x, \frac{1}{2}+y, \frac{1}{2}-z$  run parallel to the  $[\bar{2}1\bar{2}]$  direction and are interdigitated with the first. The set of infinite chains are illustrated in Fig. 7.

The sulfate is not observed bridging between cations in contrast to other 4,4'-bipy frameworks [32]. It is monodentate and decorates the chain rather than being involved in framework formation.

By careful choice of metal-sulfate ratio we sought to limit the coordination of sulfate and to promote the formation of hydrogen bonds involving sulfate. The water and sulfate ligands attached to each  $\text{Co}^{2+}$  ion have considerable hydrogen bonding capability. This is augmented by the presence of four molecules of uncoordinated water in the asymmetric unit. Compound **2** contains a three dimensional O–H...O hydrogen bond network in addition to the coordination polymers. If the structure is viewed along the [1 0 0] direction, a network which contains rings of six sulfate anions is visible (Fig. 7). The coordinated sulfate, and bound and unbound water assemble into network reminiscent of honeycomb with channels along *a*. Each six-ring has a sulfate at each vertex; one side is composed of two sulphates bound to  $\text{Co}^{2+}$ ; another side is formed from sulfates bridged by a  $\text{Co}(\text{H}_2\text{O})_4$  square plane; two more are formed from two uncoordinated water molecules bridging between two sulphates to form an  $R_4^2(8)$  embrace; a further two sides exist with two sulfates bridged by two bound water and one unbound water molecule to give an asymmetric motif with the graph set notation  $R_5^3(10)$ . The hydrogen bonding within **2** is very complicated and there are further interactions which sustain the formation of this honeycomb arrangement. The 3-D honeycomb array is easier to visualise in the Supplementary Fig. S1. Full details of the O–H...O hydrogen bonds in **2** are given in Table 3. There are a small number of C–H...O interactions present in the structure of **2**. The majority of these are short contacts between the 4,4'-bipy hydrogen atoms and sulfate or water bound to the

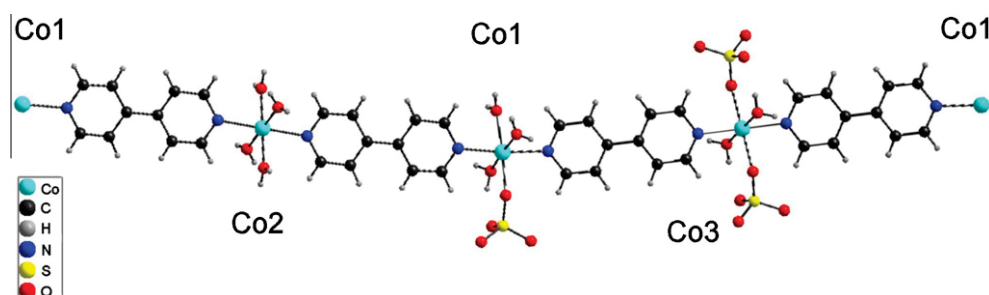


**Fig. 6.** Part of the infinite coordination polymer chain in **2**. The section drawn represents one period of the sinusoidal chain.

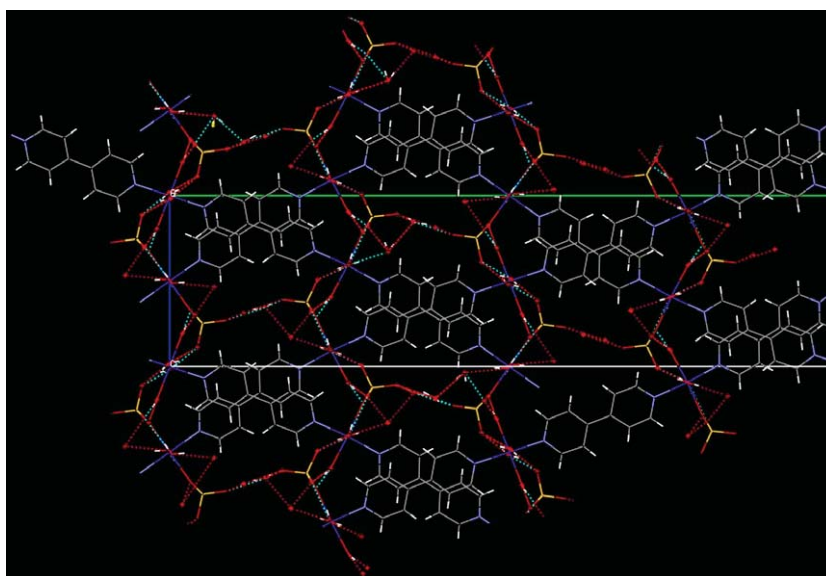


**Fig. 7.** The structure of **2** viewed down [1 0 0] showing the interdigitated  $\text{Co}^{2+}$ -4,4'-bipy chains. The six-membered rings of the 3-D hydrogen bonding network are also shown.

**Table 3**  
Details of the classical hydrogen bonds and selected C–H...O interactions in **2**. A hydrogen bond donor is signified as D–H, where D is the donor atom. The hydrogen bond acceptor atom is labelled A.

Hydrogen bond donor (D–H)	D–H bond length (Å)	H...A distance (Å)	D–H...A angle (°)	D...A distance (Å)	Acceptor atom (A) [symmetry operator]
O1–H1B	0.83(6)	1.87(4)	157(8)	2.65(8)	O6A
O1–H1B	0.83(6)	2.16(6)	149(10)	2.90(2)	O6B
O1–H1A	0.83(6)	1.79(4)	166(10)	2.602(8)	O5A [x, –y + 1/2, z + 1/2]
O1–H1A	0.83(6)	2.19(4)	165(9)	3.00(2)	O5B [x, –y + 1/2, z + 1/2]
O2–H2A	0.83(6)	2.03(4)	164(9)	2.845(8)	O6A [x + 1, –y + 1/2, z + 1/2]
O2–H2A	0.83(6)	2.20(6)	138(8)	2.87(2)	O6B [x + 1, –y + 1/2, z + 1/2]
O2–H2B	0.83(6)	2.13(3)	169(8)	2.949(7)	O4 [x, –y + 1/2, z + 1/2]
O3–H3B	0.82(6)	1.88(3)	176(10)	2.701(8)	O5A [x + 1, –y + 1/2, z + 1/2]
O3–H3B	0.82(6)	2.14(8)	131(9)	2.75(2)	O6B [x + 1, –y + 1/2, z + 1/2]
O3–H3A	0.82(6)	1.92(4)	162(8)	2.715(7)	O2W
O12–H12A	0.83(6)	1.90(4)	168(9)	2.713(7)	O1W [x – 1, y, z]
O12–H12B	0.82(6)	1.94(4)	161(10)	2.731(7)	O10 [–x + 2, –y + 1, –z + 2]
O13–H13B	0.84(6)	2.01(4)	164(10)	2.827(7)	O10 [x – 2, –y + 1/2, z – 3/2]
O13–H13A	0.83(6)	2.09(3)	171(10)	2.916(7)	O8 [x – 1, –y + 1/2, z – 3/2]
O14–H14B	0.83(6)	1.86(4)	162(10)	2.656(7)	O9 [–x + 2, y – 1/2, –z + 3/2]
O14–H14A	0.83(6)	1.86(4)	163(10)	2.665(7)	O9 [x – 1, –y + 1/2, z – 3/2]
O1W–H1D	0.83(6)	2.05(5)	152(9)	2.800(8)	O10
O1W–H1C	0.82(6)	1.94(4)	166(9)	2.744(9)	O4W [x + 1, y, z]
O2W–H2D	0.84(6)	1.96(4)	159(9)	2.757(9)	O6A [x + 1, y, z]
O2W–H2D	0.84(6)	2.45(7)	146(9)	3.18(2)	O7B [x + 1, y, z]
O2W–H2C	0.84(6)	1.94(5)	160(10)	2.740(8)	O3W [x – 1, y, z – 1]
O3W–H3C	0.83(6)	2.04(5)	155(9)	2.808(9)	O11
O3W–H3D	0.83(6)	1.98(3)	172(11)	2.808(9)	O7A [x + 1, y, z + 1]
O4W–H4C	0.84(6)	2.02(3)	171(11)	2.851(9)	O11
O4W–H4D	0.83(6)	2.01(8)	136(9)	2.666(16)	O7B [x + 1, y, z + 1]
O4W–H4D	0.83(6)	2.20(8)	137(10)	2.860(9)	O7A [x + 1, y, z + 1]
C2–H2	0.95	2.48	170	3.420(9)	O2W [x – 1, 1/2 – y, z – 1/2]
C7–H7	0.95	2.68	173	3.625(9)	O2W [x – 1, 1/2 – y, z – 1/2]
C9–H9	0.95	2.49	148	3.333(9)	O1W [x – 1, 1/2 – y, z – 1/2]
C19–H19	0.95	2.41	147	3.254(8)	O9 [x – 1, y, z – 1]

same infinite chain. However, it is noteworthy that H2 and H7 form contacts to the uncoordinated water, O2W. Although these contacts are rather long, they are close to linear, which has been identified as signifying a hydrogen bond rather than van der Waals contact [51]. Notably, H19 forms a contact to one of the sulfate anions attached to a neighbouring parallel chain, enhancing the interaction between adjacent chains. Details of selected C–H...O interactions are given in Table 3.

Thermogravimetric data for **2** are presented within the Supplementary Information. As **2** is heated in flowing nitrogen, it decom-

poses in well-defined steps. Similarly to **1**, when **2** is heated it loses all of the coordinated and uncoordinated water first in the range 60–160 °C to produce a phase with approximate composition  $\text{Co}(\text{bipy})(\text{OH})(\text{SO}_4)$  which is stable until 285 °C. Above this temperature it decomposes slowly until at 420 °C a phase with composition  $\text{Co}(\text{OH})(\text{SO}_4)$  is formed. This is stable until 570 °C at which point  $\text{CoSO}_4$  forms rapidly and is stable until 680 °C. Above this point cobalt oxide is obtained. Phase 1 contains much more sulfate than **2** and this appears to have a profound influence on the nature of the intermediate phases upon thermal decomposition. In phase 2,

it appears that some water is retained as hydroxide (perhaps bridging) to satisfy the coordination requirement of the cobalt.

The control of synthesis for frameworks of this type is clearly dependent upon a number of factors. The reactions presented here are examples of different regions of a complex composition space. For example, in reactions A and B, a small change in the initial pH of the mixture coupled with variation of the cobalt to sulfate ratio leads to different products. It is notable that variation of cobalt to 4,4'-bipy ratio leads to different products (Reactions B and C). Experiments are currently underway to alter the initial pH of the mixture while preserving the cobalt to sulfate ratio, along with an investigation of the effect of metal source on the nature of the products.

### 3.4. Spectroscopic characterisation of **1** and **2**

#### 3.4.1. Vibrational spectra of **1** and **2**

The differences in coordination modes of sulfate and 4,4'-bipy with the additional influence of hydrogen bonding interactions and local structural disorder in structures **1** and **2** are clearly manifested in the IR and Raman spectra of the ground crystals of **1** and **2**. Four normal modes of vibration including the stretching  $\nu_1(A_1)$  and  $\nu_3(T_2)$ , and the bending  $\nu_2(E)$  and  $\nu_4(T_2)$  are expected for uncoordinated sulfate anions with a regular tetrahedral geometry of  $T_d$  point symmetry. While all of these vibrations are expected to be Raman-active, only the stretching  $\nu_3(T_2)$  and the bending  $\nu_4(T_2)$  are IR-active. Upon coordination, the symmetry of the coordinated sulfate will be lowered;  $C_{3v}$  and  $C_{2v}$  for monodentate and bidentate sulfate ligands, respectively. A reduction in point symmetry should result in the appearance of  $\nu_1(A_1)$  and  $\nu_2(E)$ , and the splitting of  $\nu_3(T_2)$  and  $\nu_4(T_2)$  in the IR. The presence of one, three and four  $\nu(S-O)$  bands can therefore be expected in the IR for the uncoordinated, monodentate and bidentate sulfate. However, in the spectrum of uncoordinated sulfate the appearance of a weak  $\nu_1(A_1)$  band and a broadening of the  $\nu_3(T_2)$  band is commonly reported, due to the other non-bonding interactions of the sulfate with the neighbouring species in the crystal structures [52,53].

Fig. 8 shows portions of the IR spectra of **1** and **2**. Full spectra and detailed assignment of peaks are contained within the Supplementary Information. Despite a different coordination mode of the sulfate anions, the IR spectra of the two compounds are rather similar at the first glance, notably the presence of the very intense  $\nu_3$  and  $\nu_4$  and the very weak  $\nu_1$  and  $\nu_2$ , with the broadening of  $\nu_3$  band. The broadening of these  $\nu_3$  bands is similar in each case and clearly visible. The clear splitting of the  $\nu_4$  band in **2** compared with that of **1** is notable. The observed features in the IR spectra indicate the lowering of point symmetry of both the uncoordinated sulfate in **1** and the monodentate sulfate in **2**, which is consistent with the

crystallographic information. In the structure of **2**, although the two distinct sulfate ligands adopt the same coordination mode, crystallographic disorder and the dissimilarity of the hydrogen bonding interactions (Tables 2 and 3) differentiate the two sulfate ligands, which accounts for the apparent features in the IR spectrum. Regarding the uncoordinated sulfate anions in structure **1**, a distortion of the sulfate local environment is due to O–H...O hydrogen bonding (Fig. 3) reducing the symmetry from the expected  $T_d$ . The influence of hydrogen bonding interactions in lowering local symmetry is demonstrated by the observed spectra.

The vibrational bands of the sulfate anions are not clearly visible in the Raman spectra, (contained within the Supplementary Information) which are dominated by bands due to the 4,4'-bipy species. The di-protonation of the 4,4'-bipy ( $4,4\text{-bipyH}_2^{2+}$ ) and range of local environments for 4,4'-bipy introduce a huge degree of splitting in the characteristic vibrational bands in the IR. However, the presence of characteristic bands for the  $\nu(NH^+)$  and the  $\delta(NH^+)$  of the protonated species is obvious in the IR spectra of **1**. The splitting of the breathing modes in the Raman can also be used to distinguish the protonated  $4,4\text{-bipyH}_2^{2+}$  in **1** from the neutral 4,4'-bipy molecule in **2**.

#### 3.5. UV–Vis spectra of **1** and **2**

The electronic spectra of **1** and **2** in hexane are noticeably similar, both dominated by a broad band centred around  $42\,500\text{ cm}^{-1}$  with a shoulder centred on  $37\,200\text{ cm}^{-1}$ , which are characteristic of the phenyl ring of 4,4'-bipy and can be assigned as the ligand  $\pi-\pi^*$  transitions. In addition to these intense bands, there are also weak absorptions at frequencies lower than  $30\,000\text{ cm}^{-1}$ , particularly in the case of **1**. A weak broad band centred on  $16\,000\text{ cm}^{-1}$  is consistent with two overlapped transitions,  ${}^4T_{1g}(P) \leftarrow {}^4T_{1g}(F)$  and  ${}^4A_{2g}(F) \leftarrow {}^4T_{1g}(F)$  of the high spin  $\text{Co}^{II}$  in a distorted octahedral field demonstrated by the crystal structure.

### 4. Conclusion

Microwave-assisted hydrothermal synthesis is an extremely promising technique for the growth of MOFs. It cuts typical reaction times from a few days to a few minutes. In this study and others though, we have noticed the tendency for the products to grow as aggregates of crystals which can complicate structure determination. However, it is emerging as a very useful synthetic protocol in this field.

In a previous study, changes to the cobalt source and reaction conditions were found to influence the nature of the products in a similar system [54]. The frameworks described here suggest that even in the seemingly simple system cobalt-4,4'-bipy-sulfate-water, there is considerable scope for the synthesis of new frameworks by small changes in the initial conditions. We are currently exploring this system with a view to mapping how the nature of the product varies with initial composition. Furthermore, alteration of the amount of water present will prove another variable to control the nature and likely density of framework obtained.

Fortified by the success of our approach, we are also investigating similar syntheses using other positively charged species such as quaternary amines that may act as templates for cavities of this sort of 3-D network composed of 1-D coordination polymer and 2-D hydrogen-bonded sheets in attempts to mimic **1**.

### Acknowledgements

AR thanks the Thailand Research Fund, the Royal Golden Jubilee, and the Centre for Innovation in Chemistry, PERCH-CIC, for

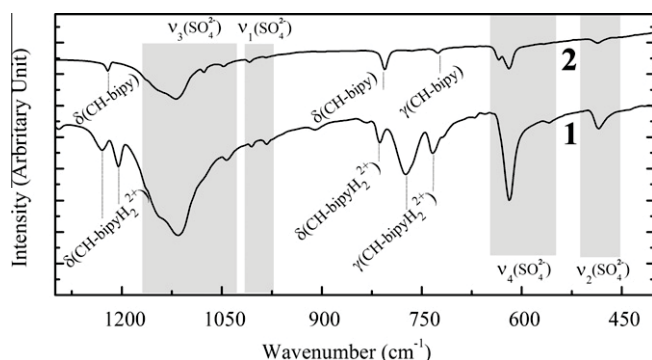


Fig. 8. Portions of the FT-IR spectra of **1** and **2** in the range  $400\text{--}1300\text{ cm}^{-1}$ . Selected band assignments are overlaid to illustrate the difference between the spectra.



support with this work. We thank Mr. I. Dobson for the collection of thermogravimetric data.

## Appendix A. Supplementary data

CCDC 780738 and 780739 contain the supplementary crystallographic data for this paper. These data can be obtained free of charge via <http://www.ccdc.cam.ac.uk/conts/retrieving.html>, or from the Cambridge Crystallographic Data Centre, 12 Union Road, Cambridge CB2 1EZ, UK; fax: (+44) 1223-336-033; or e-mail: [deposit@ccdc.cam.ac.uk](mailto:deposit@ccdc.cam.ac.uk). Supplementary data associated with this article can be found, in the online version, at doi:10.1016/j.poly.2010.10.010.

## References

- [1] A. Dyer, Introduction to Zeolite Molecular Sieves, John Wiley & Sons, 1988.
- [2] A.K. Cheetham, G. Ferey, T. Loiseau, *Angew. Chem., Int. Ed. Engl.* 38 (1999) 3268.
- [3] C.R.A. Catlow, D.S. Coombes, J.C.G. Pereira, *Chem. Mater.* 10 (1998) 3249.
- [4] M.E. Davis, R.F. Lobo, *Chem. Mater.* 4 (1992) 756.
- [5] S. Natarajan, M.P. Attfield, A.K. Cheetham, *J. Solid State Chem.* 132 (1997) 229.
- [6] C.N.R. Rao, S. Natarajan, R. Vaidyanathan, *Angew. Chem., Int. Ed.* 43 (2004) 1466.
- [7] S. Natarajan, P. Mahata, *Chem. Soc. Rev.* 38 (2009) 2304.
- [8] O.M. Yaghi, M. O'Keeffe, N.W. Ockwig, H.K. Chae, M. Eddaoudi, J. Kim, *Nature* 423 (2003) 705.
- [9] H.K. Chae, J. Kim, O.D. Friedrichs, M. O'Keeffe, O.M. Yaghi, *Angew. Chem., Int. Ed. Engl.* 42 (2003) 3907.
- [10] H. Li, M. Eddaoudi, M. O'Keeffe, O.M. Yaghi, *Nature* 402 (1999) 276.
- [11] G. Ferey, *Mol. Networks* 132 (2009) 87.
- [12] R.E. Morris, X.H. Bu, *Nat. Chem.* 2 (2010) 353.
- [13] R.J. Kuppler, D.J. Timmons, Q.R. Fang, J.R. Li, T.A. Makal, M.D. Young, D.Q. Yuan, D. Zhao, W.J. Zhuang, H.C. Zhou, *Coord. Chem. Rev.* 253 (2009) 3042.
- [14] R.Q. Zou, A.I. Abdel-Fattah, H.W. Xu, Y.S. Zhao, D.D. Hickmott, *Cryst. Eng. Commun.* 12 (2010) 1337.
- [15] H.J. Park, M.P. Suh, *Chem. Commun.* 46 (2010) 610.
- [16] L.J. Murray, M. Dinca, J.R. Long, *Chem. Soc. Rev.* 38 (2009) 1294.
- [17] D. Farrusseng, S. Aguado, C. Pinel, *Angew. Chem., Int. Ed. Engl.* 48 (2009) 7502.
- [18] J.D. Lin, X.F. Long, P. Lin, S.W. Du, *Cryst. Growth Des.* 10 (2010) 146.
- [19] K.S. Murray, C.J. Kepert, *Cooperativity in Spin Crossover Systems: Memory, Magnetism and Microporosity*, Springer-Verlag, 2004.
- [20] M.L. Tong, X.M. Chen, *Cryst. Eng. Commun.* 2 (2000) 1.
- [21] M.L. Tong, B.H. Ye, J.W. Cai, X.M. Chen, S.W. Ng, *Inorg. Chem.* 37 (1998) 2645.
- [22] D.T. De Lill, N.S. Gunning, C.L. Cahill, *Inorg. Chem.* 44 (2005) 258.
- [23] E.Y. Choi, Y.U. Kwon, *Inorg. Chem.* 44 (2005) 538.
- [24] T. Steiner, *Angew. Chem., Int. Ed. Engl.* 41 (2002) 48.
- [25] T. Steiner, *Chem. Commun.* (1997) 727.
- [26] M.D. Stephenson, T.J. Prior, M.J. Hardie, *Cryst. Growth Des.* 8 (2008) 643.
- [27] T.J. Prior, M.J. Rosseinsky, *Chem. Commun.* (2001) 1222.
- [28] A.D. Burrows, D.M.P. Mingos, A.J.P. White, D.J. Williams, *Chem. Commun.* (1996) 97.
- [29] S.R. Breeze, S.N. Wang, *Inorg. Chem.* 32 (1993) 5981.
- [30] K. Biradha, M. Sarkar, L. Rajput, *Chem. Commun.* (2006) 4169.
- [31] D. Bradshaw, J.E. Warren, M.J. Rosseinsky, *Science* 315 (2007) 977.
- [32] S.D. Huang, R.G. Xiong, P.H. Sotero, *J. Solid State Chem.* 138 (1998) 361.
- [33] G.A. Jeffrey, *An Introduction to Hydrogen Bonding*, OUP, 1997.
- [34] L.S. Long, *Cryst. Eng. Commun.* 12 (2010) 1354.
- [35] S. Luachan, C. Pakawatchai, A. Rujiwatra, *J. Inorg. Organomet. Polym. Mater.* 17 (2007) 561.
- [36] X.H. Li, Q. Miao, H.P. Xiao, M.L. Hu, *Acta Crystallogr., Sect. E* 60 (2004) m1784.
- [37] W.J. Lu, Y.M. Zhu, K.L. Zhong, *Acta Crystallogr., Sect. C* 62 (2006) m448.
- [38] C.O. Kappe, *Angew. Chem., Int. Ed. Engl.* 43 (2004) 6250.
- [39] H. Phetmung, S. Wongsawat, C. Pakawatchai, D.J. Harding, *Inorg. Chim. Acta* 362 (2009) 2435.
- [40] P. Amo-Ochoa, G. Givaja, P.J.S. Miguel, O. Castillo, F. Zamora, *Inorg. Chem. Commun.* 10 (2007) 921.
- [41] Z. Ni, R.I. Masel, *J. Am. Chem. Soc.* 128 (2006) 12394.
- [42] B. Yotnoi, S. Yimklan, T.J. Prior, A. Rujiwatra, *J. Inorg. Organomet. Polym. Mater.* 19 (2009) 306.
- [43] R.I. Cooper, R.O. Gould, S. Parsons, D.J. Watkin, *J. Appl. Cryst.* 35 (2002) 168.
- [44] F.H. Allen, *Acta Crystallogr., Sect. B* 58 (2002) 380; (see <[www.ccdc.cam.ac.uk](http://www.ccdc.cam.ac.uk)>.)
- [45] S.J. Weigel, R.E. Morris, G.D. Stucky, A.K. Cheetham, *J. Mater. Chem.* 8 (1998) 1607.
- [46] L.P. Zhang, L.G. Zhu, *Acta Crystallogr., Sect. E* 61 (2005) m1264.
- [47] Z.-X. Lian, J. Cai, C.-H. Chen, *Polyhedron* 26 (2007) 2647.
- [48] S.R. Fan, L.G. Zhu, *Acta Crystallogr., Sect. E* 61 (2005) m1689.
- [49] H. Chen, (Jiegou Huaxue) *Chin. J. Struct. Chem.* 24 (2005) 236.
- [50] C. Ruiz-Pérez, P. Lorenzo-Luis, M. Hernández-Molina, M.M. Laz, F.S. Delgado, P. Gili, M. Julve, *Eur. J. Inorg. Chem.* (2004) 3873.
- [51] T. Steiner, G.R. Desiraju, *Chem. Commun.* (1998) 891.
- [52] C. Papatrifiantafyllopoulou, E. Manessi-Zoupa, A. Escuer, S.P. Perlepes, *Inorg. Chim. Acta* 362 (2009) 634.
- [53] V.P. Mahadevan Pillai, V.U. Nayar, V.B. Jordanovska, *J. Solid State Chem.* 133 (1997) 407.
- [54] J. Lu, C. Yu, T. Nui, T. Paliwala, G. Crisci, F. Somosa, A.J. Jacobsen, *Inorg. Chem.* 37 (1998) 4637.

# Lanthanide Sulfate Frameworks: Synthesis, Structure, and Optical Properties


Published as part of a virtual special issue on Structural Chemistry in India: Emerging Themes

Bunlawee Yotnoi,<sup>†</sup> Apinpus Rujiwatra,<sup>†</sup> M. L. P. Reddy,<sup>‡</sup> Debajit Sarma,<sup>§</sup> and Srinivasan Natarajan<sup>\*,§</sup>

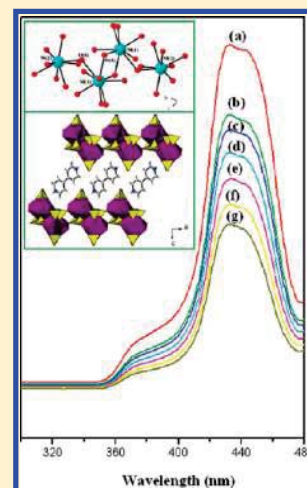
<sup>†</sup>Department of Chemistry, Faculty of Science, Chiang Mai University, Chiang Mai, Thailand, 50200

<sup>‡</sup>Chemical Sciences and Technology Division, National Institute for Interdisciplinary Science & Technology (NIIST), Thiruvananthapuram 695019, India

<sup>§</sup>Framework Solids Laboratory, Solid State and Structural Chemistry Unit, Indian Institute of Science, Bangalore-560012, India

 Supporting Information

**ABSTRACT:** Layered lanthanide sulfate compounds with three different structures have been prepared and characterized. The compounds  $[\text{C}_{10}\text{H}_{10}\text{N}_2][\text{La}(\text{SO}_4)_2] \cdot 2\text{H}_2\text{O}$  (**I**),  $[\text{C}_{10}\text{H}_{10}\text{N}_2][\text{La}(\text{SO}_4)_2(\text{H}_2\text{O})_2]_2$  (**IIa**),  $[\text{C}_{10}\text{H}_{10}\text{N}_2][\text{Pr}(\text{SO}_4)_2(\text{H}_2\text{O})_2]_2$  (**IIb**),  $[\text{C}_{10}\text{H}_{10}\text{N}_2][\text{Nd}_2(\text{SO}_4)_4(\text{H}_2\text{O})_2]_2$  (**IIIa**),  $[\text{C}_{10}\text{H}_{10}\text{N}_2][\text{Sm}_2(\text{SO}_4)_4(\text{H}_2\text{O})_2]_2$  (**IIIb**), and  $[\text{C}_{10}\text{H}_{10}\text{N}_2][\text{Eu}_2(\text{SO}_4)_4(\text{H}_2\text{O})_2]_2$  (**IIIc**) have anionic lanthanide sulfate layers separated by protonated bipyridine molecules. The layers are formed by the connectivity between the lanthanide polyhedra and sulfate tetrahedra. The formation of a two-dimensional La–O–La layer (**Ia**), Pr–O–Pr chains (**IIb**), and a tetramer cluster (**IIIa**) is noteworthy. The compounds exhibit honeycomb (**I**), square (**IIa**, **IIb**), and honeycomb (**IIIa**–**IIIc**) net arrangements, when the connectivity between the lanthanide ions is considered. Optical studies indicate the observation of characteristic metal-centered emission at room temperature. The Nd compound (**IIIa**) exhibits a two-photon upconversion behavior.



## INTRODUCTION

Traditional open-framework compounds are based on tetrahedral anions such as silicates and phosphates.<sup>1</sup> Persistent research over the years has established that other tetrahedral anions such as the arsenates,<sup>2</sup> sulfates,<sup>3</sup> selenates,<sup>4</sup> and borates<sup>5</sup> can, in fact, become part of the extended structures. The wide structural and compositional diversity exhibited by this class of compounds is a testimony for the flexible nature of the structures. Of the many open-framework compounds that have been synthesized and characterized, those of the sulfates are an important family. The synthesis, structure, and properties of a number of transition metal sulfates have been reported in recent years.<sup>6</sup> Many transition metal sulfates have one- or two-dimensional structures, and it has been observed that the formation of three-dimensionally extended sulfate networks is difficult.<sup>7</sup> It is likely that the sulfate,  $[\text{SO}_4]^{2-}$ , is much less reactive compared to the phosphate,  $[\text{PO}_4]^{3-}$ , and the arsenate,  $[\text{AsO}_4]^{3-}$ , anions. It has been shown that the elements that prefer a higher coordination environment could be employed for the synthesis of the

sulfate networks with three-dimensional structures. One such family of elements is the lanthanides.<sup>8</sup>

Lanthanide-based compounds are being studied for their varied structural, physical, and chemical properties. It is known that the lanthanide-based compounds exhibit interesting luminescence behavior.<sup>9</sup> Lanthanides exhibit intense photoluminescence behavior and find applications as fluorescent probes in biochemistry and other emission-related properties.<sup>10</sup> It has been known that the lanthanide ions exhibit narrow  $f$ – $f$  transitions, which could be exploited for light emitting device applications. Unfortunately, the  $f$ – $f$  transitions are spin and parity forbidden, and exploiting such sharp transitions requires the use of sensitizers. Recently, aromatic carboxylates have been employed as a sensitizer for observing the metal-centered emission of the rare earth ions.<sup>11</sup> Among the rare earth ions,  $\text{Eu}^{3+}$ ,  $\text{Tb}^{3+}$ , and  $\text{Nd}^{3+}$  ions are important for use as optical centers.  $\text{Eu}^{3+}$  and  $\text{Tb}^{3+}$  ions

**Received:** November 30, 2010

**Revised:** January 25, 2011

**Published:** February 16, 2011

Table 1. Synthesis Conditions Employed for the Compounds

synthesis condition				composition
mole ratio	temp (°C)	time (h)	yield (%)	product
0.70 La <sub>2</sub> O <sub>3</sub> + 2.10 4,4'-bipyridine + 0.3 mL of H <sub>2</sub> SO <sub>4</sub> (conc) + 556 H <sub>2</sub> O	200	24	68	[C <sub>10</sub> H <sub>10</sub> N <sub>2</sub> ][La(SO <sub>4</sub> ) <sub>2</sub> ]·2H <sub>2</sub> O, (I)
0.70 La <sub>2</sub> O <sub>3</sub> + 2.10 4,4'-bipyridine + 0.5 mL of H <sub>2</sub> SO <sub>4</sub> (conc) + 556 H <sub>2</sub> O	125	24	65	[C <sub>10</sub> H <sub>10</sub> N <sub>2</sub> ][La(SO <sub>4</sub> ) <sub>2</sub> (H <sub>2</sub> O) <sub>2</sub> ] <sub>2</sub> , (IIa)
0.23 Pr <sub>6</sub> O <sub>11</sub> + 2.10 4,4'-bipyridine + 0.5 mL of H <sub>2</sub> SO <sub>4</sub> (conc) + 556 H <sub>2</sub> O	125	24	63	[C <sub>10</sub> H <sub>10</sub> N <sub>2</sub> ][Pr(SO <sub>4</sub> ) <sub>2</sub> (H <sub>2</sub> O) <sub>2</sub> ] <sub>2</sub> , (IIb)
0.23 Nd <sub>2</sub> O <sub>3</sub> + 2.10 4,4'-bipyridine + 0.5 mL of H <sub>2</sub> SO <sub>4</sub> (conc) + 556 H <sub>2</sub> O	125	24	72	[C <sub>10</sub> H <sub>10</sub> N <sub>2</sub> ][Nd <sub>2</sub> (SO <sub>4</sub> ) <sub>4</sub> (H <sub>2</sub> O) <sub>2</sub> ] <sub>2</sub> , (IIIa)
0.23 Sm <sub>2</sub> O <sub>3</sub> + 2.10 4,4'-bipyridine + 0.5 mL of H <sub>2</sub> SO <sub>4</sub> (conc) + 556 H <sub>2</sub> O	125	24	68	[C <sub>10</sub> H <sub>10</sub> N <sub>2</sub> ][Sm <sub>2</sub> (SO <sub>4</sub> ) <sub>4</sub> (H <sub>2</sub> O) <sub>2</sub> ] <sub>2</sub> , (IIIb)
0.23 Eu <sub>2</sub> O <sub>3</sub> + 2.10 4,4'-bipyridine + 0.5 mL of H <sub>2</sub> SO <sub>4</sub> (conc) + 556 H <sub>2</sub> O	125	24	70	[C <sub>10</sub> H <sub>10</sub> N <sub>2</sub> ][Eu <sub>2</sub> (SO <sub>4</sub> ) <sub>4</sub> (H <sub>2</sub> O) <sub>2</sub> ] <sub>2</sub> , (IIIc)

are useful in the visible region ( $\lambda = \sim 400\text{--}800\text{ nm}$ ), whereas Nd<sup>3+</sup> ions are useful in the near infrared (IR) region ( $\lambda = 800\text{--}1700\text{ nm}$ ). It has been shown that the Nd<sup>3+</sup> ions also exhibit upconversion behavior of converting the IR radiation to the visible region through a two-photon absorption process.<sup>12</sup>

In spite of the considerable progress achieved toward the understanding of the photophysical behavior of the lanthanides, the subtle relationship that exists between the photophysical properties and the structure suggests the need for further studies. It occurred to us that the lack of higher dimensional structures in sulfates and the need for larger coordination numbers for the lanthanide ions can be gainfully employed in preparing new three dimensionally extended lanthanide sulfate compounds. It has been shown that the use of 4,4'-bipyridine enhances the dimensionality of the structures by acting as a rigid linker between the metal centers.<sup>13</sup> In addition, the use of 4,4'-bipyridine might assist in the luminescence behavior of the lanthanides through initial absorption and energy transfer. We used a combination of these during the preparation of a new family of lanthanide sulfate compounds. Our efforts were successful and we have isolated three new lanthanide sulfate compounds. The compounds [C<sub>10</sub>H<sub>10</sub>N<sub>2</sub>][La(SO<sub>4</sub>)<sub>2</sub>]·2H<sub>2</sub>O (I), [C<sub>10</sub>H<sub>10</sub>N<sub>2</sub>][La(SO<sub>4</sub>)<sub>2</sub>(H<sub>2</sub>O)<sub>2</sub>]<sub>2</sub> (IIa), [C<sub>10</sub>H<sub>10</sub>N<sub>2</sub>][Pr(SO<sub>4</sub>)<sub>2</sub>(H<sub>2</sub>O)<sub>2</sub>]<sub>2</sub> (IIb), [C<sub>10</sub>H<sub>10</sub>N<sub>2</sub>][Nd<sub>2</sub>(SO<sub>4</sub>)<sub>4</sub>(H<sub>2</sub>O)<sub>2</sub>]<sub>2</sub> (IIIa), [C<sub>10</sub>H<sub>10</sub>N<sub>2</sub>][Sm<sub>2</sub>(SO<sub>4</sub>)<sub>4</sub>(H<sub>2</sub>O)<sub>2</sub>]<sub>2</sub> (IIIb), and [C<sub>10</sub>H<sub>10</sub>N<sub>2</sub>][Eu<sub>2</sub>(SO<sub>4</sub>)<sub>4</sub>(H<sub>2</sub>O)<sub>2</sub>]<sub>2</sub> (IIIc) all have a two-dimensional layer structure formed by the connectivity between the rare earth ions and the sulfate units. The 4,4'-bipyridine ligand occupies the interlamellar spaces. In this paper, we present the synthesis, structure, and photophysical properties of all the compounds.

## EXPERIMENTAL SECTION

**Synthesis and Initial Characterization.** The compounds were prepared by employing the hydrothermal method. In a typical synthesis, for I, La<sub>2</sub>O<sub>3</sub> (0.2283 g, 0.70 mmol) was added to 10 mL of deionized water. To this, 4,4'-bipyridine (0.3283 g, 2.10 mmol) and concentrated sulfuric acid (0.3 mL) were added under continuous stirring. The mixture was homogenized for 30 min at room temperature. The final mixture was transferred, sealed in a 23 mL PTFE lined autoclave, and heated at 200 °C for 24 h under autogenous pressure. The final product contained large quantities of colorless rod-shaped single crystals, which were filtered under a vacuum, washed with deionized water, and dried at ambient conditions (yield  $\sim 68\%$  based on La). The other compounds were obtained employing similar conditions (Table 1). In the case of Pr (IIb), Nd (IIIa), Sm (IIIb), and Eu (IIIc), the final product contains large quantities of light green (Pr), light purple (Nd), light purple (Sm), and colorless (Eu) rod-type single crystals. In the case of compound IIa, the product was found to be a polycrystalline white powder. The product was later characterized by powder X-ray diffraction (PXRD) studies by

comparing with the PXRD pattern of the related Pr compound (IIb). The PXRD pattern of IIa matched well with the simulated XRD pattern generated from the single crystal structure of Pr (IIa) compound. The microcrystalline phase IIa was indexed and the unit cell parameters were obtained from the PXRD patterns by the Le Bail method (Supporting Information Figure S1).<sup>14</sup> The Eu doped (4 mol % and 8 mol %) and Tb doped (4 mol % and 8 mol %) in place of La in I and Eu doped (4 mol % and 8 mol %) and Tb doped (4 and 8 mol) in place of La in IIa were prepared using the same experimental procedure as that employed for I and IIa. Initial characterizations were carried out by elemental analysis, PXRD, thermogravimetric analysis (TGA), and IR studies.

PXRD patterns were recorded in the  $2\theta$  range 5–50° using Cu K $\alpha$  radiation (Philips X'pert) (Supporting Information, Figures S2–S8). The IR spectra for the compounds were recorded as KBr pellets (Perkin-Elmer, SPECTRUM 1000). The IR spectroscopic studies exhibit typical peaks corresponding to the hydroxyl group, the amino groups, etc. (Supporting Information, Figure S9). The main IR bands are (KBr):  $\nu$  (H<sub>2</sub>O) = 3230–3450 cm<sup>−1</sup>,  $\nu$  (N–H) = 3070–3110 cm<sup>−1</sup>,  $\nu$  (C–H) = 2670–2780 cm<sup>−1</sup>,  $\nu$  (C–H) = 1300–1500 cm<sup>−1</sup>,  $\nu_1$  (SO<sub>4</sub>) = 950–1000 cm<sup>−1</sup>,  $\nu_3$  (SO<sub>4</sub>) = 1100–1150 cm<sup>−1</sup>,  $\delta$  (SO<sub>4</sub>) = 500–700 cm<sup>−1</sup>. The IR spectrum can be useful for investigating the sulfate species. In general, the free sulfate ions exhibit two bands at 1105 and 615 cm<sup>−1</sup>, which are assigned to the  $\nu_3$ (F2) stretching [ $\nu_3$ (SO)] and  $\nu_4$ (F2) stretching [ $\delta_d$ (OSO)] modes, respectively. The coordination of the free sulfate group to the metal centers would lower the overall symmetry of the sulfate group and lead to the splitting of the  $\nu_3$  and  $\nu_4$  modes. The IR spectrum of the present compounds exhibits characteristic IR bands for the sulfate ions, SO<sub>4</sub><sup>2−</sup>, with the IR-active region for the SO<sub>4</sub> tetrahedron located between 500 and 1150 cm<sup>−1</sup>. In addition, we observed that the sulfate site symmetry is also lowered due to the many bridging coordination modes of the sulfate ions. The observed shoulders in the IR bands, thus, in the region 1025–1185 cm<sup>−1</sup> may be attributed to the  $\nu_3$  modes and the shoulders in the region 554–670 cm<sup>−1</sup> can be assigned to the  $\nu_4$  modes.

**Single Crystal Structure Determination.** A suitable single crystal of each compound was carefully selected under a polarizing microscope and glued to a thin glass fiber. The single crystal data were collected on a Bruker AXS smart Apex CCD diffractometer at 293(2) K. The X-ray generator was operated at 50 kV and 35 mA using Mo K $\alpha$  ( $\lambda = 0.71073\text{ \AA}$ ) radiation. Data were collected with  $\omega$  scan width of 0.3°. A total of 606 frames were collected in three different settings of  $\phi$  (0, 90, 180°) keeping the sample-to-detector distance fixed at 6.03 cm and the detector position ( $2\theta$ ) fixed at  $-25^\circ$ . The data were reduced using SAINTPLUS,<sup>15</sup> and an empirical absorption correction was applied using the SADABS program.<sup>16</sup> The structure was solved and refined using SHELXL97<sup>17</sup> present in the WinGx suite of programs (Version 1.63.04a).<sup>18</sup> All the hydrogen positions were initially located in the difference Fourier maps, and for the final refinement, the hydrogen atoms were placed in geometrically ideal positions and refined in the riding mode. Final refinement included atomic positions for all the atoms, anisotropic thermal parameters for all the non-hydrogen atoms, and isotropic thermal parameters for all the hydrogen atoms. Full-matrix

**Table 2.** Crystal Data and Structure Refinement Parameters for the Compounds  $[\text{C}_{10}\text{H}_{10}\text{N}_2][\text{La}(\text{SO}_4)_2] \cdot 2\text{H}_2\text{O}$ , (**I**)  $[\text{C}_{10}\text{H}_{10}\text{N}_2][\text{Pr}(\text{SO}_4)_2(\text{H}_2\text{O})_2]_2$ , (**IIb**),  $[\text{C}_{10}\text{H}_{10}\text{N}_2][\text{M}_2(\text{SO}_4)_4(\text{H}_2\text{O})_2]_2$ <sup>a</sup>

empirical formula	$\text{C}_5\text{H}_7\text{NLaS}_2\text{O}_9$	$\text{C}_5\text{H}_9\text{NPrS}_2\text{O}_{10}$	$\text{C}_{10}\text{H}_{14}\text{N}_2\text{Nd}_2\text{S}_4\text{O}_{18}$	$\text{C}_{10}\text{H}_{14}\text{N}_2\text{Sm}_2\text{S}_4\text{O}_{18}$	$\text{C}_{10}\text{H}_{14}\text{N}_2\text{Eu}_2\text{S}_4\text{O}_{18}$
formula weight	426.13	448.16	866.95	875.14	878.36
crystal system	triclinic	triclinic	triclinic	triclinic	triclinic
space group	$P\bar{1}$	$P\bar{1}$	$P\bar{1}$	$P\bar{1}$	$P\bar{1}$
$a/\text{\AA}$	5.6238(2)	5.0354(1)	8.0119(5)	7.9585(2)	7.9370(6)
$b/\text{\AA}$	7.3489(3)	7.0079(1)	9.4075(6)	9.3752(3)	9.3612(7)
$c/\text{\AA}$	12.9709(5)	16.6321(3)	14.9538(9)	14.9270(4)	14.9214(10)
$\alpha/^\circ$	90.821(2)	88.50	79.439(1)	79.327(2)	79.348(1)
$\beta/^\circ$	96.912(2)	87.94	83.749(1)	83.927(2)	83.996(1)
$\gamma/^\circ$	100.159(2)	75.47	73.988(1)	73.830(2)	73.777(1)
$\text{vol}/\text{\AA}^3$	523.48(3)	567.67(2)	1062.99(11)	1049.44(5)	1044.52(13)
$Z$	2	2	2	2	2
$T/\text{K}$	293(2)	293(2)	293(2)	293(2)	293(2)
$\rho_{\text{calc}} (\text{g cm}^{-3})$	2.703	2.622	2.696	2.769	2.793
$\mu (\text{mm}^{-1})$	4.522	4.711	5.320	6.036	6.448
$\theta$ range (deg)	1.58–26.00	2.45–26.00	2.28–26.00	2.48–26.00	1.39–26.00
$\lambda$ (Mo $\text{K}\alpha$ ) ( $\text{\AA}$ )	0.71073	0.71073	0.71073	0.71073	0.71073
$R_{\text{int}}$	0.0262	0.0244	0.0252	0.0568	0.0416
reflection collected	7955	8568	11057	25572	10666
unique reflections	2007	2217	4159	4119	4082
no. of parameters	163	188	325	325	325
$R$ indices $[I > 2\sigma(I)]$	$R_1 = 0.0161, wR_2 = 0.0438$	$R_1 = 0.0160, wR_2 = 0.0428$	$R_1 = 0.0215, wR_2 = 0.0538$	$R_1 = 0.0420, wR_2 = 0.1141$	$R_1 = 0.0534, wR_2 = 0.1400$
$R$ indices (all data)	$R_1 = 0.0163, wR_2 = 0.0439$	$R_1 = 0.0166, wR_2 = 0.0431$	$R_1 = 0.0249, wR_2 = 0.0551$	$R_1 = 0.0438, wR_2 = 0.1154$	$R_1 = 0.0542, wR_2 = 0.1412$

<sup>a</sup>  $\text{M} = \text{Nd}^{3+}$  (**IIIa**),  $\text{Sm}^{3+}$  (**IIIb**), and  $\text{Eu}^{3+}$  (**IIIc**).  $R_1 = \sum |F_o| - |F_c| / \sum |F_o|$ ;  $wR_2 = \{ \sum [w(F_o^2 - F_c^2)] / \sum [w(F_o^2)] \}^{1/2}$ .  $w = 1 / [\rho^2(F_o)^2 + (aP)^2 + bP]$ .  $P = [\max(F_o, 0) + 2(F_c)^2] / 3$ , where  $a = 0.0188$  and  $b = 0.7083$  for **I**, where  $a = 0.0190$  and  $b = 0.7399$  for **IIb**, where  $a = 0.0257$  and  $b = 1.0297$  for **IIIa**, where  $a = 0.0879$  and  $b = 4.0864$  for **IIIb**, where  $a = 0.1103$  and  $b = 2.2382$  for **IIIc**.

**Table 3.** Selected Observed Bond Distances in the Lanthanide Sulfate Compounds<sup>a</sup>

bond	distance ( $\text{\AA}$ )	bond	distances ( $\text{\AA}$ )	bond	distances ( $\text{\AA}$ )
<b>I</b>					
La(1)–O(1)#1	2.473(2)	La(1)–O(4)	2.555(1)	La(1)–O(6)#5	2.610(2)
La(1)–O(2)#2	2.474(2)	La(1)–O(5)#4	2.575(2)	La(1)–O(3)	2.613(2)
La(1)–O(3)#3	2.555(2)	La(1)–O(5)	2.589(2)	La(1)–O(6)	2.623(2)
<b>IIb</b>					
Pr(1)–O(1)#1	2.402(2)	Pr(1)–O(4)#3	2.480(2)	Pr(1)–O(7)	2.602(2)
Pr(1)–O(2)#2	2.434(2)	Pr(1)–O(5)	2.504(2)	Pr(1)–O(8)	2.615(2)
Pr(1)–O(3)	2.469(2)	Pr(1)–O(6)	2.527(2)	Pr(1)–O(7)#3	2.820(2)
<b>IIIa</b>					
Nd(1)–O(1)	2.378(3)	Nd(1)–O(4)	2.471(2)	Nd(1)–O(7)	2.526(2)
Nd(1)–O(2)	2.429(3)	Nd(1)–O(5)#2	2.482(2)	Nd(1)–O(4)#3	2.603(2)
Nd(1)–O(3)#1	2.460(3)	Nd(1)–O(6)	2.490(3)	Nd(1)–O(8)	2.731(2)
Nd(2)–O(9)#2	2.340(2)	Nd(2)–O(12)	2.473(3)	Nd(2)–O(8)	2.517(2)
Nd(2)–O(10)	2.423(3)	Nd(2)–O(13)#4	2.489(2)	Nd(2)–O(15)	2.548(3)
Nd(2)–O(11)	2.470(3)	Nd(2)–O(14)#5	2.509(2)		

<sup>a</sup> Symmetry transformations used to generate equivalent atoms: For **I**: #1  $x + 1, y, z$ , #2  $x - 1, y, z$ , #3  $-x + 1, -y + 1, -z + 2$ , #4  $-x, -y + 1, -z + 2$ , #5  $-x, -y, -z + 2$ . For **IIb**: #1  $-x + 1, -y, -z$ , #2  $x, y + 1, z$ , #3  $x + 1, y, z$ . For **IIIa**: #1  $x, y + 1, z$ , #2  $-x + 1, -y, -z + 1$ , #3  $-x + 1, -y + 1, -z + 1$ , #4  $x, y - 1, z$ , #5  $-x, -y, -z + 1$ .

least-squares refinement against  $|F^2|$  was carried out using the WinGx package of programs.<sup>18</sup> Details of the structure solution and final refinements for the compounds are given in Table 2. CCDC: 802347–802351 contains the crystallographic data for this paper. These data can be obtained free of charge from The Cambridge Crystallographic Data Center (CCDC) via [www.ccdc.cam.ac.uk/data\\_request/cif](http://www.ccdc.cam.ac.uk/data_request/cif).

## RESULTS AND DISCUSSION

**Structure of  $[\text{C}_{10}\text{H}_{10}\text{N}_2][\text{La}(\text{SO}_4)_2] \cdot 2\text{H}_2\text{O}$ , (**I**).** The asymmetric unit of **I** consists of 18 non-hydrogen atoms. It has one crystallographically independent  $\text{La}^{3+}$  ion, two sulfate groups, half a molecule of protonated bipyridine molecule, and a lattice



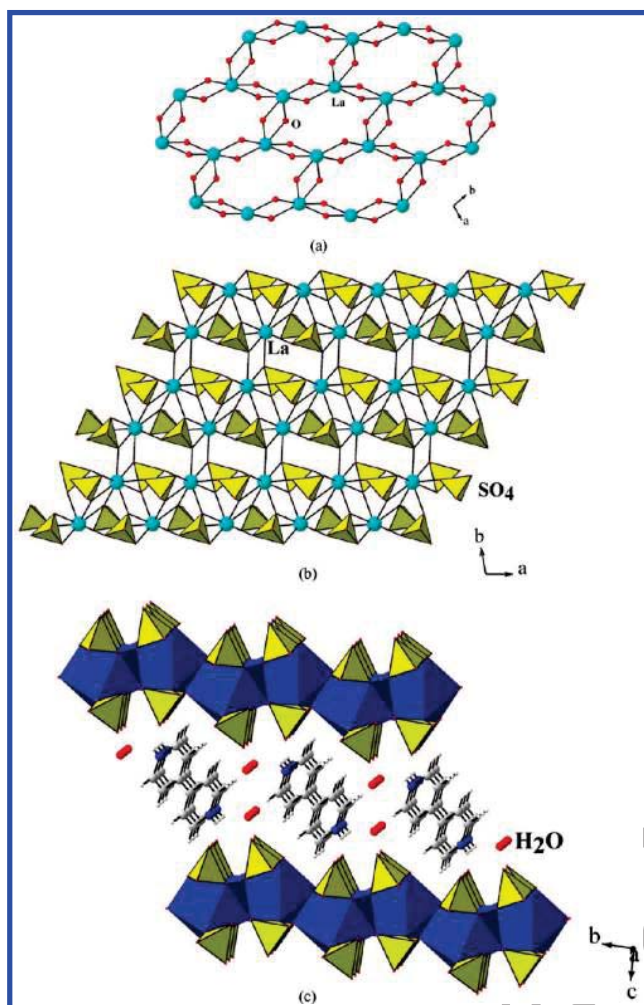


**Figure 1.** (a) View of the two-dimensional infinite La–O–La layer in  $[\text{C}_{10}\text{H}_{10}\text{N}_2][\text{La}(\text{SO}_4)_2] \cdot 2\text{H}_2\text{O}$ , **I**. Only the lanthanide ion connectivity is shown (see text). (b) View of the two-dimensional lanthanide sulfate layer in the  $ab$  plane. (c) The arrangement of layers in the  $bc$  plane. Note that the bipyridine molecules occupy interlamellar spaces along with the water molecules.

water molecule (Supporting Information, Figure S10). The half bipyridine unit is related to the other half through the C–C bond, which lies on the center of symmetry. The  $\text{La}^{3+}$  ions are surrounded by nine sulfate oxygens forming a  $\text{LaO}_9$  polyhedra, with a distorted tricapped trigonal prismatic coordination environment (Supporting Information, Figure S11). The oxygen atoms O(3), O(5), and O(6) were found to be three coordinated, binding two La atoms and one S atom. The La–O bond distances are in the range of 2.474(2)–2.624(2) Å (av. 2.563 Å). The O–La–O bond angles are in the range 53.59(6)–160.11(6)°. The selected bond distances are given in Table 3.

The structure of **I** consists of linkages between  $\text{LaO}_9$  tricapped trigonal prisms and  $\text{SO}_4$  tetrahedral units. The  $\text{LaO}_9$  units are connected through three coordinated oxygen atoms [O(3), O(5), and O(6)] forming an infinite two-dimensional La–O–La network (Figure 1a). The two sulfate tetrahedral units, S(1) $\text{O}_4$  and S(2) $\text{O}_4$ , are connected to the La–O–La two-dimensional layers in such a way that they connect with 4 and 3 La atoms respectively, and each possess one terminal S=O

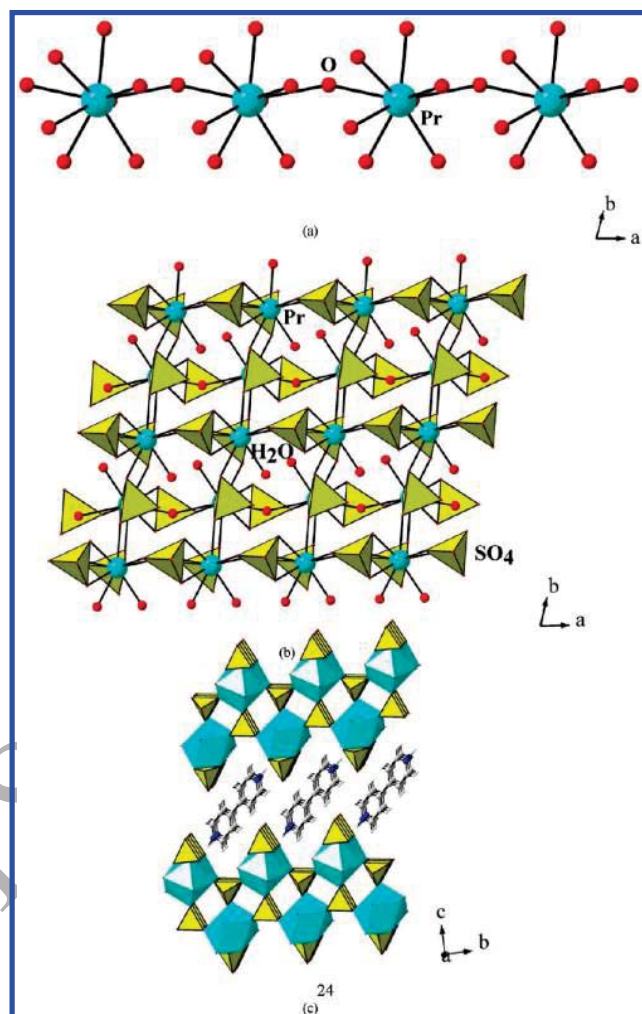


**Figure 2.** (a) The one-dimensional infinite Pr–O–Pr chains observed in  $[\text{C}_{10}\text{H}_{10}\text{N}_2][\text{Pr}(\text{SO}_4)_2(\text{H}_2\text{O})_2]_2$ , **IIb**. (b) View of the two-dimensional praseodymium sulfate layer in the  $ab$  plane. Note that the bound water molecules project out of the plane of the layers. (c) Arrangement of the layers in the  $bc$  plane.

bond [S(1)–O(7) and S(2)–S(8)] (Figure 1b). The layers are arranged in a ABABAB... fashion and are stabilized by the N–H...O interaction between the protonated bipyridinium cation and the framework oxygen [N(1)–H(1)...O(7), N–O = 2.72 Å, angle = 143°] (Figure 1c).

**Structure of  $[\text{C}_{10}\text{H}_{10}\text{N}_2][\text{Pr}(\text{SO}_4)_2(\text{H}_2\text{O})_2]_2$ , (IIb).** The asymmetric unit of **IIb** consists of 19 non-hydrogen atoms. It has one crystallographically independent  $\text{Pr}^{3+}$  atoms, two sulfate units, half a molecule of protonated bipyridine molecule, and two coordinated water molecules (Figure S12, Supporting Information). The  $\text{Pr}^{3+}$  ions are coordinated by seven sulfate oxygen and two aqua oxygen forming a  $\text{PrO}_9$  polyhedra with a distorted tricapped trigonal prism arrangement (Figure S13, Supporting Information). The half bipyridine molecule is related to the other half via the C–C bond, which lies on the center of symmetry. The Pr–O bond distances are in the range of 2.402(2)–2.820(2) Å (av. 2.539 Å). The O–Pr–O bond angles are in the range 54.65(6)–149.31(6)°. The selected bond distances are given in Table 3.

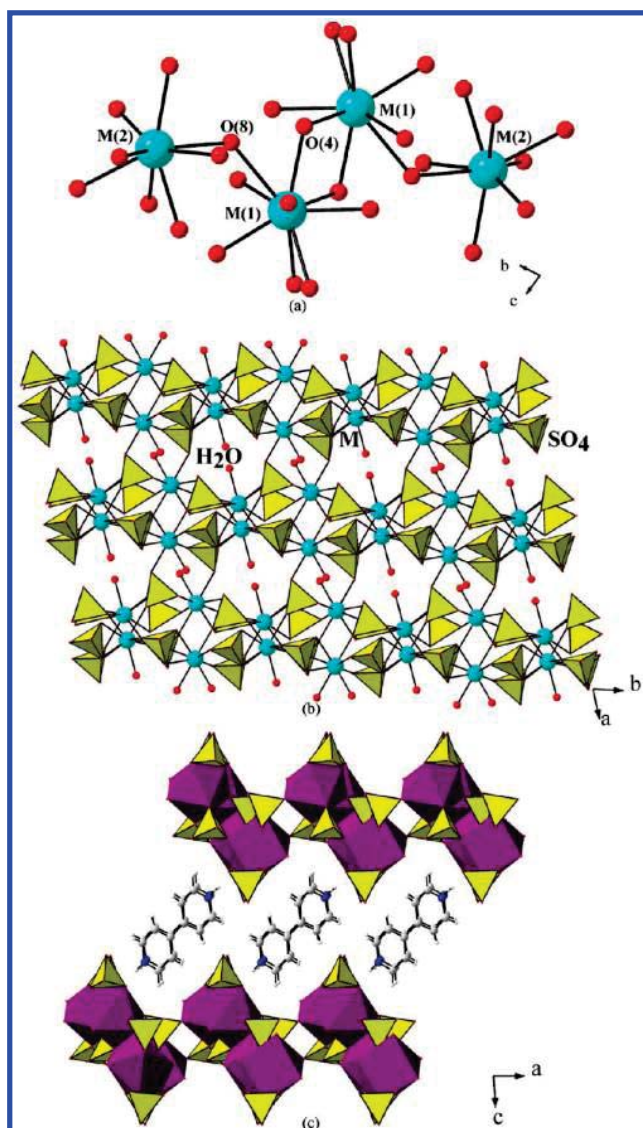


**Figure 3.** (a) View of the tetrameric unit found in  $[\text{C}_{10}\text{H}_{10}\text{N}_2][\text{Nd}_2(\text{SO}_4)_4(\text{H}_2\text{O})_2]_2$ , **IIIa**. (b) The two-dimensional layer in the *ab* plane. (c) The arrangement of the layers in **IIIa**.

The structure of **IIb** consists of a linkage between  $\text{PrO}_9$  and  $\text{SO}_4$  units forming a two-dimensional structure. The Pr atoms are connected through a  $\mu_2$  oxygen atom forming one-dimensional  $\text{Pr}-\text{O}-\text{Pr}$  infinite chains (Figure 2a). The sulfate tetrahedra  $\text{S}(1)\text{O}_4$  connects the  $\text{Pr}-\text{O}-\text{Pr}$  chains forming the two-dimensional structure, which is anionic. The other sulfate tetrahedral  $\text{S}(2)\text{O}_4$  connects only to the Pr centers and is not employed in extending the dimensionality of the structure. This arrangement appears to satisfy the coordination requirement of the central Pr atoms only (Figure 2b). Another view to understand the structure is to consider the connectivity between  $\text{PrO}_9$  and  $\text{S}(1)\text{O}_4$  polyhedral units, which forms a one-dimensional edge-shared ladder-like structure (Figure S14, Supporting Information). The ladder units are connected with the  $\text{Pr}-\text{O}-\text{Pr}$  linkages giving rise to the two-dimensional layers. The layers are arranged in a  $\text{ABABAB} \cdots$  fashion and the interlamellar space is occupied by the protonated bipyridinium cations (Figure 2c). Only one hydrogen bond interaction is observed

$[\text{N}(1)-\text{H}(1)-\text{O}(8); \text{N}-\text{O} = 2.77 \text{ \AA}, \text{angle} = 155^\circ]$  between the bipyridinium cation and the framework oxygen, which is not very strong.<sup>19</sup>

**Structure of  $[\text{C}_{10}\text{H}_{10}\text{N}_2][\text{M}_2(\text{SO}_4)_4(\text{H}_2\text{O})_2]_2$ ,  $\text{M} = \text{Nd}^{3+}$  (**IIIa**),  $\text{Sm}^{3+}$  (**IIIb**), and  $\text{Eu}^{3+}$  (**IIIc**).** The asymmetric unit of  $[\text{M}_2(\text{SO}_4)_4(\text{H}_2\text{O})_2](\text{C}_{10}\text{H}_{10}\text{N}_2)$ ,  $\text{M} = \text{Nd}^{3+}$  (**IIIa**),  $\text{Sm}^{3+}$  (**IIIb**) and  $\text{Eu}^{3+}$  (**IIIc**) consists of 36 non-hydrogen atoms. It has two crystallographically independent  $\text{M}^{3+}$  ion, four sulfate groups, one protonated bipyridine molecule, and two coordinated water molecules (Figure S15, Supporting Information). The  $\text{M}(1)^{3+}$  ions are surrounded by eight sulfate oxygen and one aqua oxygen to form a  $\text{M}(1)\text{O}_9$  polyhedra, which has a distorted tricapped trigonal prismatic coordination environment. In the case of  $\text{M}(2)^{3+}$  ions, seven sulfate oxygen and one aqua oxygen surround the central metal atom forming a  $\text{M}(2)\text{O}_8$  polyhedra, with a distorted square antiprism coordination geometry (Figure S16, Supporting Information). The oxygen atoms, O(4) and O(8), are three coordinated connecting two metal centers and a sulfate unit. The  $\text{M}-\text{O}$  bond distances are in the range for Nd: 2.340(2)–2.731(2) Å (av. 2.490 Å); for Sm: 2.306(4)–2.734(4) Å (av. 2.462 Å) and for Eu: 2.292(4)–2.733(4) Å (av. 2.450 Å). The  $\text{O}-\text{M}-\text{O}$  bond angles are in the range for Nd: 53.76(7)–151.02(9)°; for Sm: 54.14(12)–150.76(14)° and for Eu: 54.04(13)–151.09(15)°. The selected bond distances are given in Table 3.

In the structure of **IIIa**, the  $\text{MO}_9$  and  $\text{MO}_8$  polyhedral units are linked with the sulfate tetrahedra giving rise to a two-dimensional anionic layer structure. The  $\text{M}(1)\text{O}_9$  units are linked through the three-connected oxygen atom, [O(8)], with  $\text{M}(2)\text{O}_8$  units forming a four-membered cluster (Figure 3a). The sulfate tetrahedral units bridge the four-membered clusters giving rise to the two-dimensional layer arrangement with an overall anionic layer of the formula,  $[\text{M}_2(\text{SO}_4)_4(\text{H}_2\text{O})_2]^-$  (Figure 3b). The charge is balanced by the presence of the protonated bipyridinium cations, which occupies the interlamellar spaces.  $\text{N}-\text{H} \cdots \text{O}$  hydrogen bond interactions  $[\text{N}(1)-\text{H}(1) \cdots \text{O}(1); \text{N}-\text{O} = 2.757 \text{ \AA}, \text{angle} = 170^\circ, \text{N}(2)-\text{H}(2) \cdots \text{O}(6); \text{N}-\text{O} = 2.830 \text{ \AA}, \text{angle} = 171^\circ]$  have been observed, which appears to be strong.<sup>18</sup>

**Structural Comparison.** The three structures (**I**, **IIb**, and **IIIa**) identified in the present study have some common features: (i) The lanthanide ions have predominantly a tricapped trigonal prismatic coordination, (ESI, X); (ii) the lanthanide ions are connected through the three-coordinated oxygen atoms forming two-dimensional  $\text{La}-\text{O}-\text{La}$  layers in **Ia**, a one-dimensional chain in **IIb** and a four-member cluster in **IIIa**.

In addition, the sulfate connectivity in these structures also exhibit subtle differences. The sulfate groups participate in bonding between two lanthanide centers in **I**, while half the sulfate units in **IIa** and **IIIa** appear to satisfy the coordination requirement of the lanthanide centers only. The larger coordination (8 and 9) requirement of the lanthanide ions could be responsible for this, which also resulted in having coordinated aqua ligands in the structures of **IIa** and **IIIa**. Exclusive use of ligands for coordination requirements is not new, and examples of such roles for the participating ligands have been observed earlier in framework compounds.<sup>20</sup> The presence of bipyridine as a cation in the structure is also important and noteworthy. In many framework compounds, the bipyridine generally binds with the metal centers extending dimensionality,<sup>21</sup> but here it performs the role of a template molecule.

When the lanthanide connectivity alone is considered in these structures, we observed a honeycomb arrangement in the case of **I** and **IIIa**, whereas a square-grid results for **IIb** (Figure 4).



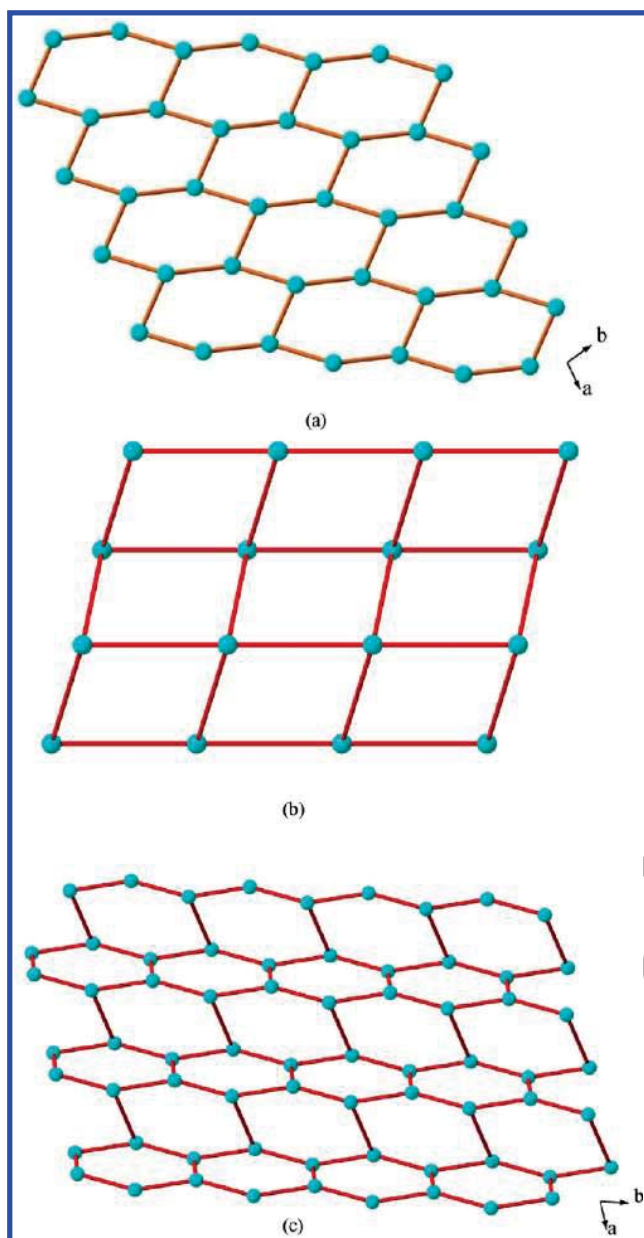


**Figure 4.** The lanthanide ion connectivity in the present structures: (a) the honeycomb layer in **I**; (b) the square-grid layer in **IIb**; (c) the honeycomb layer in **IIIa**.

The formations of such networks in lanthanide containing compounds are rare.

**Thermogravimetric Studies.** TGA on all the compounds has been carried out in flowing air (flow rate = 20 mL min<sup>-1</sup>) in the temperature range 30–850 °C (heating rate = 5 °C min<sup>-1</sup>) (Supporting Information, Figures S17–19). All the compounds exhibit comparable thermal behavior. For compound **I**, two step weight loss was observed (Supporting Information, Figure S17). The first weight loss of 3.7% observed in the range 150–250 °C corresponds to the loss of water molecules (4.2%). The second sharper weight loss of 44.9% in the range 480–520 °C corresponds to the loss of the bipyridine and some sulfate (calc. 46.5%). In the case of **IIa** and **IIb** we observed a near identical behavior in terms of the weight losses though the total weight loss

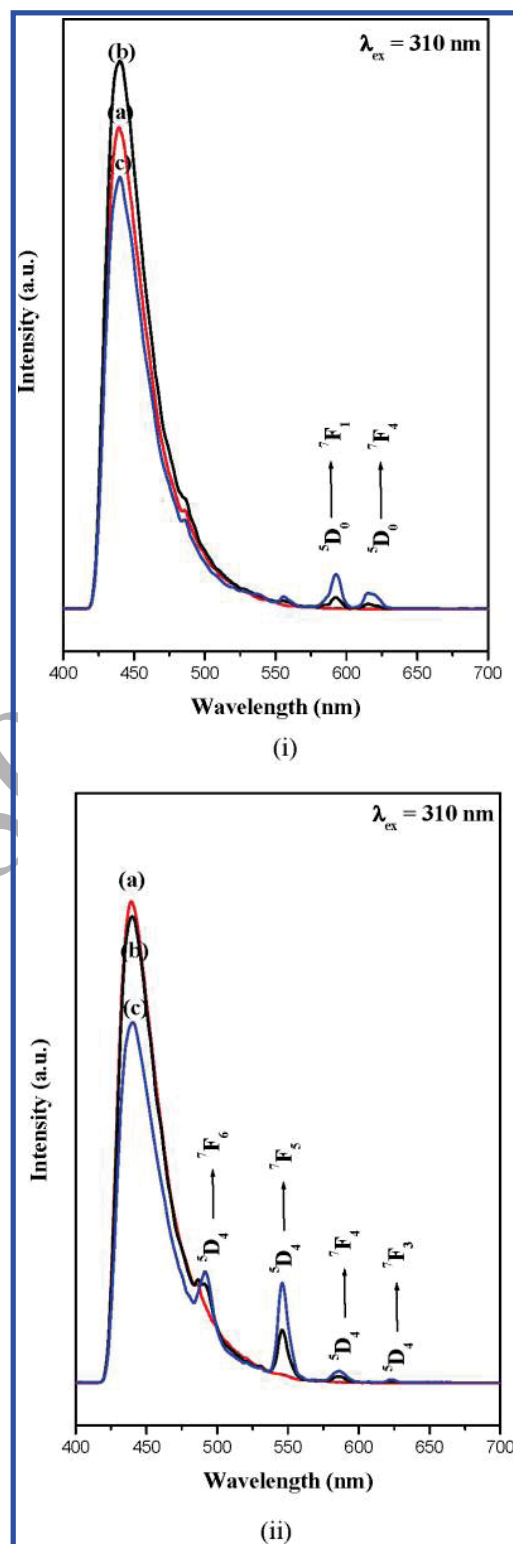


**Figure 5.** Room temperature photoluminescence spectra of compound **I** and the corresponding Eu<sup>3+</sup> and Tb<sup>3+</sup> doped samples. (i) (a) Compound **I**, (b) 4 mol % and (c) 8 mol % Eu<sup>3+</sup> doped samples. (ii) (a) Compound **I**, (b) 4 mol % and (c) 8 mol % Tb<sup>3+</sup> doped samples.

was different (Supporting Information, Figure S18). The first weight loss of 7.8% in the range 140–190 °C corresponds to the loss of water molecules (calc. 8% for **IIa** and **IIb**). The second



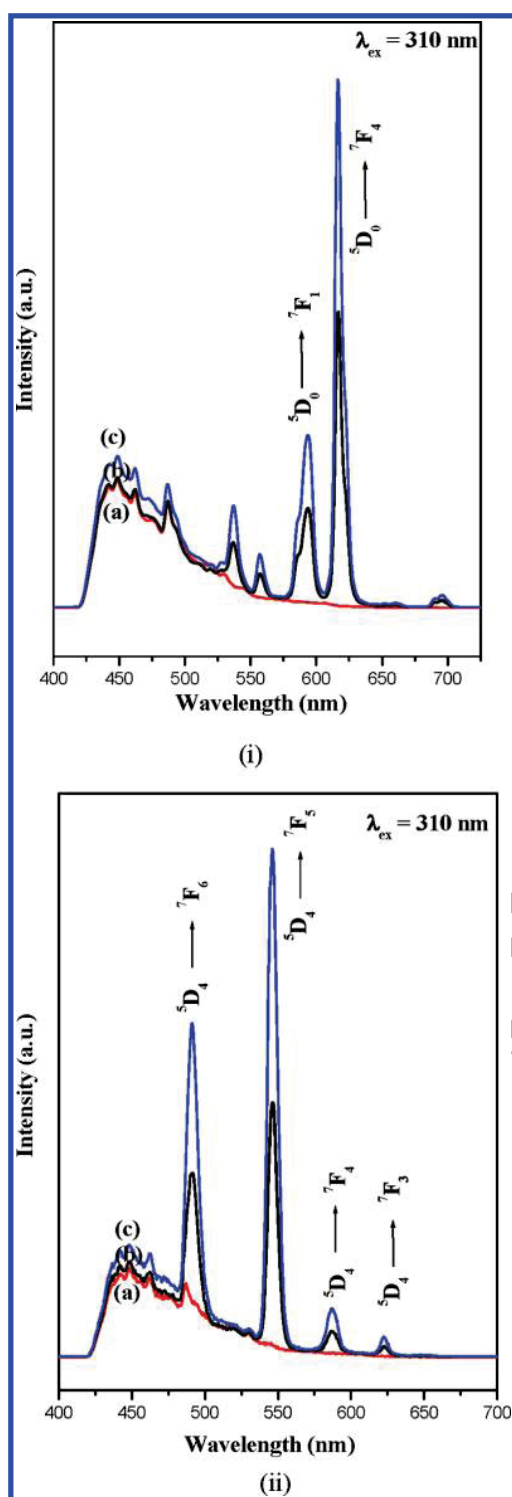


**Figure 6.** Room temperature photoluminescence spectra of compound **IIa** and the corresponding  $\text{Eu}^{3+}$  and  $\text{Tb}^{3+}$  doped samples. (i) (a) Compound **IIa**, (b) 4 mol % and (c) 8 mol %  $\text{Eu}^{3+}$  doped samples. (ii) (a) Compound **IIa**, (b) 4 mol % and (c) 8 mol %  $\text{Tb}^{3+}$  doped samples.

weight loss 31.2% for **IIa** and 44.2% for **IIb** in the range 410–500 °C corresponds to the loss of the bipyridine and sulfate (calc 44.4% for **IIa**: 45.6% for **IIb**). In the case of compounds **I** and **IIa**, the calcined product was found to be crystalline and corresponds to the compound  $\text{La}_2\text{O}_2\text{SO}_4$  (JCPDS: 85-1535). In the case of

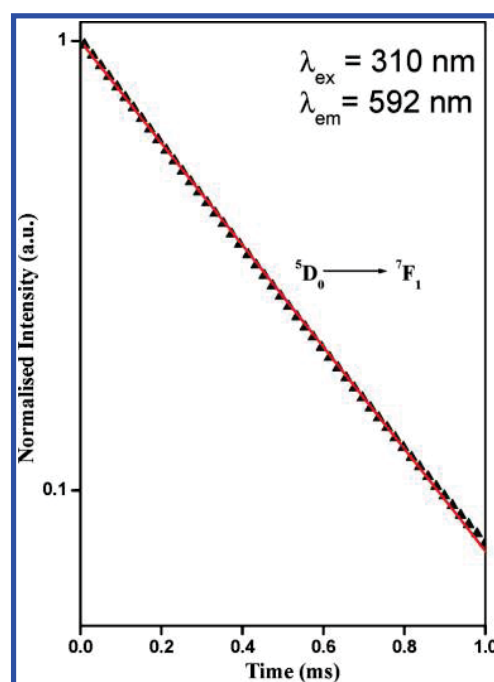


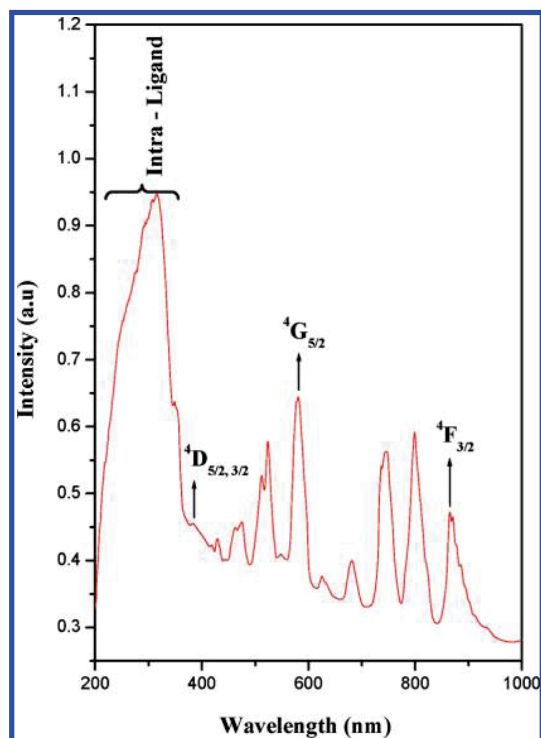
**Figure 7.** Room temperature luminescence decay of the  $^5\text{D}_0 \rightarrow ^7\text{F}_1$  emission band for the 4 mol %  $\text{Eu}^{3+}$  doped compound **I**.

**IIb**, the final calcined product was found to be  $\text{Pr}_2\text{O}_2\text{SO}_4$  (JCPDS: 29-1073). The TGA behavior of compounds **IIIa**, **IIIb**, and **IIIc** are also similar, exhibiting a two-step weight loss. For **IIIa**, the first weight loss of 3.7% in the range 180–250 °C, corresponds to the loss of the coordinated water molecules (calc. 4.4%). The second weight loss of 25.3% in the range 470–500 °C is followed by another loss. The total weight loss of 55% corresponds to the loss of the bipyridine along with some sulfate. The calcined product was found to be crystalline and corresponds to the phase  $\text{Nd}_2\text{O}_2\text{SO}_4$  (JCPDS: 48-1829). Similarly for **IIIb** and **IIIc**, we observed the formation of  $\text{Sm}_2\text{O}_2\text{SO}_4$  (JCPDS: 41-0681) and  $\text{Eu}_2\text{O}_2\text{SO}_4$  (JCPDS: 48-1211) phases after the TGA studies.

**Luminescence Studies.** All the compounds exhibited one strong absorption band centered around 450 nm, which corresponds to the ligand to metal charge transfer (LMCT) band, when excited using a wavelength of  $\lambda = 310$  nm. To probe and to appreciate the LMCT effect further, we have prepared two sets of compounds by doping a small concentration of  $\text{Eu}^{3+}$  and  $\text{Tb}^{3+}$  (4% and 8%) in place of  $\text{La}^{3+}$  (compounds **I** and **IIa**). The results of the photoluminescence studies were shown in Figures 5 and 6. The doped samples exhibited sharp characteristics peaks, in addition to the LMCT peak at 450 nm. We also observed a pink color for  $\text{Eu}^{3+}$  doped samples and a green color for the  $\text{Tb}^{3+}$  doped samples when observed under the UV illumination (Supporting Information, Figure S20–S21). When excited using a wavelength of  $\lambda = 310$  nm, we observed the characteristic  $^5\text{D}_0 \rightarrow ^7\text{F}_j$  ( $j = 1, 2$ ) emission lines for  $\text{Eu}^{3+}$  and  $^5\text{D}_4 \rightarrow ^7\text{F}_j$  ( $j = 3, 4, 5, 6$ ) emission lines for  $\text{Tb}^{3+}$ , respectively (Figures 5 and 6). It may be noted the intensity of the characteristic lanthanide emission due to  $\text{Eu}^{3+}$  and  $\text{Tb}^{3+}$  is not strong, suggesting that the energy transfer process in the present compounds are quite poor. This situation is in contrast to the behavior observed in many of the lanthanide benzene carboxylate frameworks, where intense lanthanide emissions have been observed.<sup>22</sup> Even though the

**Table 4.** Lifetime Values for the Compounds **I** (4% Eu), **IIa** (4% Eu), **I** (4% Tb), and **IIa** (4% Tb)

S. no.	compound	lifetime (in ms)
		$^5D_0 \rightarrow ^7F_1$
1.	<b>I</b> (4 mol % Eu)	0.3833
2.	<b>IIa</b> (4 mol % Eu)	0.2726
		$^5D_4 \rightarrow ^7F_6$
4.	<b>I</b> (4 mol % Tb)	1.1801
5.	<b>IIa</b> (4 mol % Tb)	1.3420

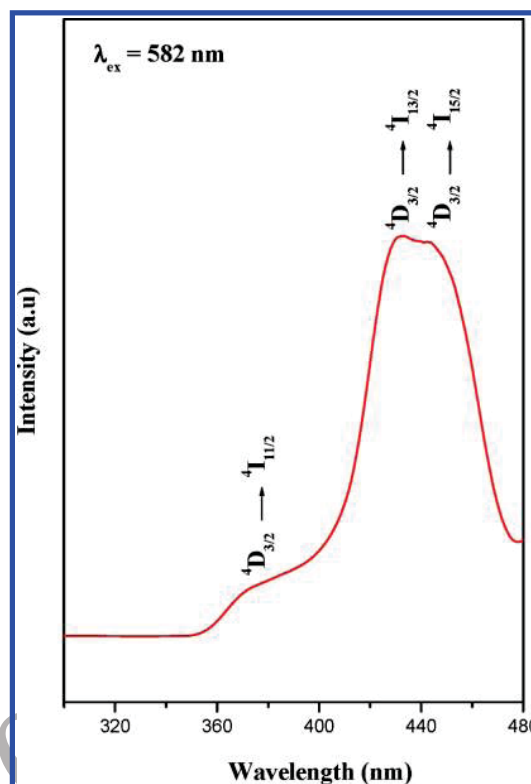
**Figure 8.** Room temperature UV-vis spectra of compound  $[\text{Nd}_2(\text{SO}_4)_4(\text{H}_2\text{O})_2](\text{C}_{10}\text{H}_{10}\text{N}_2)$ , **IIIa**.

intensity of the emission in the present compounds is not strong, we sought to investigate the lifetime of the excited states in the doped compounds.

**Lifetime Studies.** The luminescence lifetimes of the excited states of the 4 mol % doped samples of **I** and **IIa** were investigated. The  $^5D_0 \rightarrow ^7F_1$  band for the  $\text{Eu}^{3+}$  samples **I** (4% Eu) and **IIa** (4% Eu) and the  $^5D_4 \rightarrow ^7F_6$  emission band for the  $\text{Tb}^{3+}$  samples **I** (4% Tb) and **IIa** (4% Tb) were monitored for the lifetime studies employing 310 nm excitation at room temperature. The experimental luminescent decay curve was fitted to a single exponential decay function as,

$$I = I_0 \exp(-t/\tau)$$

where  $I$  and  $I_0$  stands for the luminescent intensities at time  $t = t$  and  $t = 0$  and  $\tau$  is defined as the luminescent lifetime. The fit of the curve for a single exponential decay suggests a lifetime value of 0.38 ms for **I** (4% Eu) (Figure 7). The lifetime values for the other samples are given in Table 4 (Supporting Information, Figure S22–S24). The values of the lifetime observed in the present compounds are comparable to the values generally

**Figure 9.** Room temperature upconversion spectra of compound **IIIa**, using 582 nm radiation.

known for the pure  $\text{Eu}^{3+}$  and  $\text{Tb}^{3+}$  compounds reported in the literature.<sup>23</sup>

**Upconversion Studies.** There has been some recent interest in the study of a possible two-photon upconversion processes in compounds containing  $\text{Nd}^{3+}$  ions.<sup>24</sup> The upconversion in these compounds are actually anti-Stokes emissions. Among the present compounds,  $[\text{C}_{10}\text{H}_{10}\text{N}_2][\text{Nd}_2(\text{SO}_4)_4(\text{H}_2\text{O})_2]_2$ , **IIIa**, could exhibit this upconversion emission. The room temperature UV-vis spectrum of **IIIa** indicated that the absorption increases rapidly with decreasing wavelength due to the intraligand absorption (Figure 8). From the UV studies, the absorption bands of the  $\text{Nd}^{3+}$  ions appear to exhibit primary ground state Stark splitting of the eigenstates due to the possible crystal field effects.<sup>25</sup>

A schematic of the energy transfer process in the upconversion using  $\text{Nd}^{3+}$  ions suggests the possible pathway for the two-photon upconversion processes (Supporting Information, Figure S25). The  $\text{Nd}^{3+}$  compound (**IIIa**) has an intense absorption at  $\sim 582$  nm, which corresponds to the  $^4I_{9/2} \rightarrow ^4G_{5/2}$  transition. This is a hypersensitive band and also satisfies the selection rules of  $\Delta J = \pm 2$ ,  $\Delta L = \pm 2$ , and  $\Delta S = 0$ . The luminescence of **IIIa** at short wavelength results from the  $^4D_{3/2}$  levels. In order to observe the possible two-photon absorption in **IIIa**, one needs to excite the photon to either the  $^4D_{3/2}$  or  $^4D_{5/2}$  levels. The direct excitation to this level may be limited due to the intraligand absorption by the short wavelength radiation. In addition, the excitation wavelength ( $\lambda = 582$  nm) is far from the wavelength that may be required for the intraligand absorption. Thus, during our studies, the first excited  $^4G_{5/2}$  level can relax nonradiatively to the  $^4F_{3/2}$  level where some population can occur. This photon may further undergo excited state absorption (ESA), while the

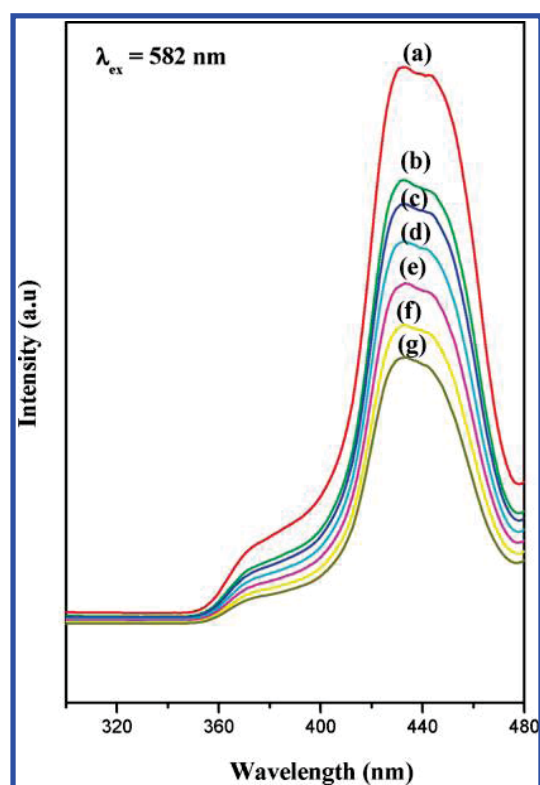


Figure 10. The observed emission dependence on the excitation intensity of  $[\text{Nd}_2(\text{SO}_4)_4(\text{H}_2\text{O})_2](\text{C}_{10}\text{H}_{10}\text{N}_2)$ , **IIIa**. (a) 100%, (b) 90.32% (c) 85.19%, (d) 81.34%, (e) 74.86%, (f) 69.38% and (g) 63.56%.

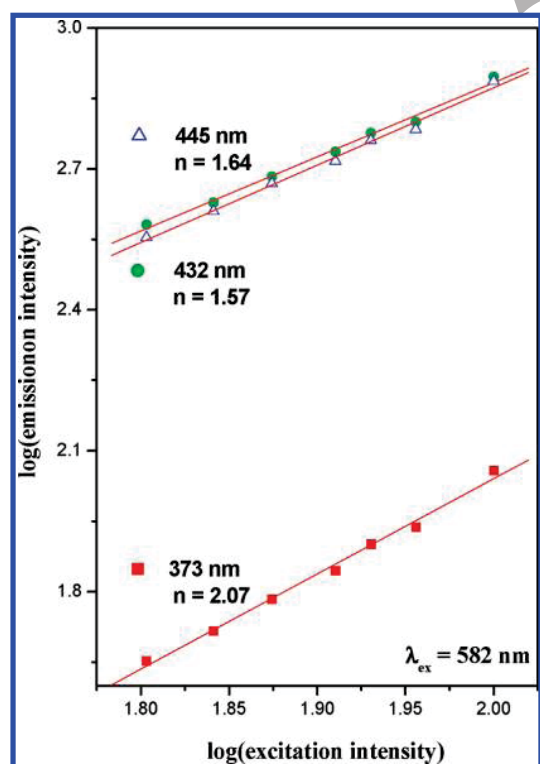


Figure 11. The log–log plot of the excitation intensity dependence of the luminescence intensity for  $\lambda = 373, 432$ , and  $445$  nm.

others relax to lower energy levels. The excitation wavelength ( $\sim 582$  nm) was used to populate the  $^4\text{F}_{3/2}$  levels and efficient re-excitation from the  $^4\text{F}_{3/2}$  to the  $^4\text{D}_{5/2}$  levels. It is likely that the excited  $^4\text{D}_{5/2}$  levels from the ESA also relax nonradiatively to the  $^4\text{D}_{3/2}$  levels from which the upconverted luminescence may be observed. The upconverted luminescence spectra for this yellow pumping (582 nm excitation) from  $^4\text{D}_{3/2}$  levels are shown in Figure 9.

To study the dependence of the excitation intensity on the upconverted luminescence intensity, we have also performed a simple power dependence study. Here a series of sterile glass plates are placed sequentially in the pathway between the excitation source and the sample. The decrease in excitation intensity per glass plate was precalibrated using the UV–vis spectrometer in the transmission mode and also normalized with respect to the transmission obtained in the absence of any glass slides. The decrease in the luminescence intensity for six successive glass plates is shown in Figure 10. We have plotted the log–log plot of the luminescence intensity versus the excitation intensity, and a fit could provide a clue to the number of photons involved in the upconversion process (Figure 11). The plot for the three emission peaks at 373, 432, and 445 nm was found to be linear with a slope of 2.07, 1.57, and 1.64, respectively. These values suggest that the excitation may be due to two photons that are employed successfully. The ideal value for the two photon absorption should be closer to 2, and the decreased value may be due to the loss of some of the excitation energy at the one-photon absorption level, which could result from the  $^4\text{F}_{3/2} \rightarrow ^4\text{I}_{11/2}$ ,  $^4\text{F}_{3/2} \rightarrow ^4\text{I}_{9/2}$  level in the near-IR region.

## CONCLUSIONS

The synthesis, structure, and characterization of a family of layered lanthanide sulfate phases have been accomplished. The formation of related compounds by subtle variations of the synthesis conditions suggests the importance of the reaction parameters in the formation of framework compounds. The observation of bipyridine molecules being protonated and occupying the interlamellar spaces is important and not common. The formation of two-dimensional  $\text{La}-\text{O}-\text{La}$  network in **I** is noteworthy as such networks are not commonly observed. The observation of two-photon upconversion behavior in the Nd-containing compound (**IIIa**) and metal centered emission in  $\text{Eu}^{3+}$  (red) and  $\text{Tb}^{3+}$  (green) doped samples of lanthanum (**I** and **II**) indicates the possibility of using these compounds as optical probes. Further study is required to evaluate the structure–property relationship in these compounds.

## ASSOCIATED CONTENT

**S Supporting Information.** Simulated and experimental powder XRD patterns of the compounds **I–III** and the doped samples, TGA curves of **I–III**, IR spectra and bond angles of **I–III** are presented. The decay curves of the excited state of the doped samples and the Le Bail fit for the compounds **IIa** are also presented. This material is available free of charge via the Internet at <http://pubs.acs.org>.

## AUTHOR INFORMATION

### Corresponding Author

\*E-mail: [snatarajan@sscu.iisc.ernet.in](mailto:snatarajan@sscu.iisc.ernet.in).



## ACKNOWLEDGMENT

S.N. thanks the Department of Science and Technology (DST), Government of India, for the award of a research grant and the authors thanks the Council of Scientific and Industrial Research (CSIR), Government of India, for the award of a fellowship (DS) and a research grant. S.N. also thanks the Department of Science and Technology, Government of India, for the award of the RAMANNA fellowship. B.Y. and A.R. thank the Royal Golden Jubilee program (RGJ), Thailand, and Thailand Research Fund (TRF), Thailand, for a fellowship (B.Y.) and a research grant (A.R.).

## REFERENCES

- (1) (a) Natarajan, S.; Mandal, S. *Angew. Chem., Int. Ed.* **2008**, *47*, 4798. (b) Murugavel, R.; Choudhury, A.; Walawalkar, M. G.; Pothiraja, R.; Rao, C. N. R. *Chem. Rev.* **2009**, *109*, 4283. (c) Cheetham, A. K.; Ferey, G.; Loiseau, T. *Angew. Chem., Int. Ed.* **1999**, *38*, 3268. (d) Wilson, S. T.; Lok, B. M.; Messina, C. A.; Cannan, T. R.; Flanigen, E. M. *J. Am. Chem. Soc.* **1982**, *104*, 1146. (e) Meier, W. M.; Oslen, D. H.; Baerlocher, C. *Atlas of Zeolite Structure Types*; Elsevier: London, 1996; (f) Chen, L.; Bu, X. *Inorg. Chem.* **2006**, *45*, 4654. (g) Rao, C. N. R.; Natarajan, S.; Choudhury, A.; Neeraj, S.; Ayi, A. A. *Acc. Chem. Res.* **2001**, *34*, 80. (h) Murugavel, R.; Walawalkar, M. G.; Dan, M.; Roesky, H. W.; Rao, C. N. R. *Acc. Chem. Res.* **2004**, *37*, 763.
- (2) (a) Rao, V. K.; Chakrabarti, S.; Natarajan, S. *Inorg. Chem.* **2007**, *46*, 10781. (b) Rao, V. K.; Green, M. A.; Pati, S. K.; Natarajan, S. *J. Phys. Chem. B* **2007**, *111*, 12700. (c) Chakrabarti, S.; Natarajan, S. *Angew. Chem., Int. Ed.* **2002**, *41*, 1224. (d) Chakrabarti, S.; Pati, S. K.; Green, M. A.; Natarajan, S. *Eur. J. Inorg. Chem.* **2003**, 4395. (e) Ekambaram, S.; Sevov, S. C. *Inorg. Chem.* **2000**, *39*, 2405. (f) Bu, X.; Gier, T. E.; Ferey, G. *Chem. Commun.* **1997**, 2271.
- (3) (a) Lin, J.; Dong-Wei Guo, D.-W.; Tian, Y.-Q. *Cryst. Growth Des.* **2008**, *8*, 4571. (b) Rao, C. N. R.; Behera, J. N.; Dan, M. *Chem. Soc. Rev.* **2006**, *35*, 375. (c) Paul, G.; Choudhury, A.; Rao, C. N. R. *Chem. Mater.* **2003**, *15*, 1174.
- (4) Krivovichev, S. V.; Kahlenberg, V.; Tananaev, I. G.; Myasoedov, B. F. Z. *Anorg. Allg. Chem.* **2005**, *631*, 2358.
- (5) (a) Paul, A. K.; Natarajan, S. *Cryst. Growth Des.* **2010**, *10*, 765. (b) Paul, A. K.; Sachidananda, K.; Natarajan, S. *Cryst. Growth Des.* **2010**, *10*, 456.
- (6) (a) Fu, Y.; Xu, Z.; Ren, J.; Wu, H.; Yuan, R. *Inorg. Chem.* **2006**, *45*, 8452. (b) Behera, J. N.; Rao, C. N. R. *Chem. Asian J.* **2006**, *1*, 742. (c) Behera, J. N.; Gopalkrishnan, K. V.; Rao, C. N. R. *Inorg. Chem.* **2004**, *43*, 2636. (d) Paul, G.; Choudhury, A.; Sampathkumaran, E. V.; Rao, C. N. R. *Angew. Chem., Int. Ed.* **2002**, *41*, 4297.
- (7) (a) Rujiwatara, A.; Kepert, C. J.; Rosseinsky, M. J. *Chem. Commun.* **1999**, 2307. (b) Rujiwatara, A.; Kepert, C. J.; Claridge, J. B.; Rosseinsky, M. J.; Kumagai, H.; Kurmoo, M. *J. Am. Chem. Soc.* **2001**, *123*, 10584. (c) Behera, J. N.; Rao, C. N. R. *Can. J. Chem.* **2005**, *83*, 668.
- (8) (a) Akkari, H.; Benard-Rocherulle, P.; Merazig, H.; Roisnel, T.; Rocherulle, J. *Solid State Sci.* **2006**, *8*, 704. (b) Ding, S.; Xu, Y.; Nie, L.; Feng, W. J. *Cluster Sci.* **2006**, *17*, 627. (c) Bataille, T.; Louer, D. J. *Mater. Chem.* **2002**, *12*, 3487.
- (9) (a) Binnemans, K. *Chem. Rev.* **2009**, *109*, 4283. (b) Yan, L.; Yue, Q.; Jia, Q. -X.; Lemerrier, G.; Gao, E.-Q. *Cryst. Growth Des.* **2009**, *9*, 2984. (c) Pope, S. J. A.; Coe, B. J.; Faulkner, S.; Bichenkova, E. V.; Yu, X.; Douglas, K. J. *Am. Chem. Soc.* **2004**, *126*, 9490. (d) Zhao, B.; Chen, X. Y.; Cheng, P.; Liao, D. Z.; Yan, S. P.; Jiang, Z. H. *J. Am. Chem. Soc.* **2004**, *126*, 15394. (e) Rudzinski, C. M.; Young, A. M.; Nocera, D. G. *J. Am. Chem. Soc.* **2002**, *124*, 1723. (f) Justel, T.; Nikol, H.; Ronda, C. *Angew. Chem., Int. Ed.* **1998**, *37*, 3084. (g) Blasse, G.; Grabmaier, B. C. *Luminescent Materials*; Springer: Berlin, 1994; (h) Bunzli, J. C. G.; Choppin, G. R. *Lanthanide Probes in Life, Chemical and Earth Science, Theory and Practice*; Elsevier: Amsterdam, 1989.
- (10) (a) Sendor, D.; Hilder, M.; Juestel, T.; Junk, P. C.; Kynast, U. H. *New J. Chem.* **2003**, *27*, 1070. (b) de Lill, D. T.; de Bettencourt-Dias, A.; Cahill, C. L. *Inorg. Chem.* **2007**, *46*, 3960. (c) Crosby, G. A. *Mol. Cryst.* **1966**, *1*, 37. (d) Eisinger, J.; Lamola, A. A. *Biochem. Biophys. Acta* **1971**, *240*, 299. (e) Filipescu, N.; Mushrush, G. W. *J. Phys. Chem.* **1968**, *72*, 3516. (f) Heller, A.; Wasserman, E. J. *J. Chem. Phys.* **1956**, *42*, 949.
- (11) (a) Sarma, D.; Prabu, M.; Biju, S.; Reddy, M. L. P.; Natarajan, S. *Eur. J. Inorg. Chem.* **2010**, 3813. (b) Mahata, P.; Natarajan, S. *Inorg. Chem.* **2007**, *46*, 1250.
- (12) (a) Kiritsis, V.; Michaelides, A.; Skoulaka, S.; Golhen, S.; Ouahab, L. *Inorg. Chem.* **1998**, *37*, 3407. (b) Reineke, T. M.; Eddaoudi, M.; Moler, D.; O'Keeffe, M.; Yaghi, O. M. *J. Am. Chem. Soc.* **2000**, *122*, 4843. (c) Pan, L.; Adams, K. M.; Hernandez, H. E.; Wang, X. T.; Zheng, C.; Hattori, Y.; Kaneko, K. *J. Am. Chem. Soc.* **2003**, *125*, 3062. (d) Zhao, B.; Cheng, P.; Chen, X. Y.; Cheng, C.; Shi, W.; Liao, D. Z.; Yan, S. P.; Jiang, Z. H. *J. Am. Chem. Soc.* **2004**, *126*, 3012. (e) Long, D. L.; Hill, R. J.; Blake, A. L.; Champness, N. R.; Hubberstey, P.; Proserpio, D. M.; Wilson, C.; Schroder, M. *Angew. Chem., Int. Ed.* **2004**, *43*, 1851. (f) Zhang, M. B.; Zhang, J.; Zheng, S. T.; Yang, G. Y. *Angew. Chem., Int. Ed.* **2005**, *44*, 1385. (g) Chen, B.; Wang, L.; Zapata, F.; Qian, G.; Lobkovsky, B. J. *Am. Chem. Soc.* **2008**, *130*, 6718. (h) Shi, F. N.; Cunha-Silva, L.; Sa Ferreira, R. A.; Mafra, L.; Trindade, T.; Carlos, L. D.; Almeida Paz, F. A.; Rocha, J. J. *Am. Chem. Soc.* **2008**, *130*, 150.
- (13) (a) Jiang, Y.; Huang, J.; Kasumaj, B.; Jeschke, G.; Hunger, M.; Mallat, T.; Baiker, A. *J. Am. Chem. Soc.* **2009**, *131*, 2058. (b) Li, Y.; Xie, L.; Liu, Y.; Yang, R.; Li, X. *Inorg. Chem.* **2008**, *47*, 10372. (c) Pichon, A.; Fierro, C. M.; Nieuwenhuysen, M.; James, S. L. *CrystEngComm* **2007**, *9*, 449. (d) Maji, T. K.; Ohba, M.; Kitagawa, S. *Inorg. Chem.* **2005**, *44*, 9225. (e) Biradha, K.; Fujita, M. *Chem. Commun.* **2001**, 15. (f) Noro, S.; Kitagawa, S.; Kondo, M.; Seki, K. *Angew. Chem., Int. Ed.* **2000**, *39*, 2082. (g) Kondo, M.; Yoshitomi, T.; Seki, K.; Matsuzaka, H.; Kitagawa, S. *Angew. Chem., Int. Ed.* **1997**, *36*, 1725.
- (14) Le Bail, A.; Duroy, H.; Fourquet, J. L. *Mater. Res. Bull.* **1988**, *23*, 447–452.
- (15) SMART (V 5.628), SAINT (V 6.45a), XPREP, SHELXTL; Bruker AXS Inc.: Madison, Wisconsin, USA, 2004.
- (16) Sheldrick, G. M. *Siemens Area Correction Absorption Correction Program*; University of Göttingen: Göttingen, Germany, 1994.
- (17) Sheldrick, G. M. *SHELXL-97 Program for Crystal Structure Solution and Refinement*; University of Göttingen: Göttingen, Germany, 1997.
- (18) Farrugia, J. L. WinGx suite for small-molecule single crystal crystallography. *J. Appl. Crystallogr.* **1999**, *32*, 837.
- (19) (a) Desiraju, G. R. *Angew. Chem., Int. Ed. Engl.* **1995**, *34*, 2311. (b) Desiraju, G. R. *Perspective in Supramolecular Chemistry: The Crystal as a Supramolecular Entity*; Wiley: Chichester, 1996, 2.
- (20) (a) Ramaswamy, P.; Hegde, N. N.; Prabhu, R.; Vidya, V. M.; Datta, A.; Natarajan, S. *Inorg. Chem.* **2009**, *48*, 11697. (b) Mandal, S.; Natarajan, S. *Chem.—Eur. J.* **2007**, *13*, 968.
- (21) (a) Paul, A. K.; Madras, G.; Natarajan, S. *Dalton Trans.* **2010**, 39, 2263. (b) Paul, A. K.; Madras, G.; Natarajan, S. *CrystEngComm* **2009**, *11*, 55. (c) Paul, A. K.; Madras, G.; Natarajan, S. *Phys. Chem. Chem. Phys.* **2009**, *11*, 11285.
- (22) (a) Mahata, P.; Ramya, K. V.; Natarajan, S. *Chem.—Eur. J.* **2008**, *14*, 5839. (b) Mahata, P.; Ramya, K. V.; Natarajan, S. *Dalton Trans.* **2007**, 36, 4017.
- (23) Zhang, Z. H.; Okamura, T.; Hasuchika, Y.; Kawaguchi, H.; Kong, L. Y.; Sun, W. Y.; Ueyam, N. *Inorg. Chem.* **2005**, *44*, 6219.
- (24) Auzel, F. *Chem. Rev.* **2004**, *104*, 139.
- (25) Ju, J. J.; Kwon, T. Y.; Kim, H. K.; Kim, J. H.; Kim, S. C.; Cha, M.; Yun, S. I. *Mater. Lett.* **1996**, *29*, 13.

*Communication*

## Microwave-assisted hydrothermal synthesis of lead zirconate fine powders

**Saowalak Tapala and Apinpus Rujiwatra\***

Centre for Innovation in Chemistry, Department of Chemistry, Faculty of Science, Chiang Mai University, Chiang Mai 50200, Thailand

\* Corresponding author, e-mail: [apinpus@gmail.com](mailto:apinpus@gmail.com)

*Received: 3 August 2010 / Accepted: 18 January 2011 / Published: 19 January 2011*

**Abstract:** A rapid synthesis of lead zirconate fine powders by microwave-assisted hydrothermal technique is reported. The influences of type of lead precursor, concentration of potassium hydroxide mineraliser, applied microwave power and irradiation time are described. The synthesised powders were characterised by powder X-ray diffraction, field emission scanning electron microscopy, energy-dispersive X-ray spectroscopic microanalysis and light scattering technique. The merits of the microwave application in reducing reaction time and improving particle mono-dispersion and size uniformity as well as the drawbacks, viz. low purity of the desired phase and increasing demand of mineraliser, are discussed in relation to conventional heating method.

**Keywords:** lead zirconate, hydrothermal synthesis, microwave-assisted synthesis

### INTRODUCTION

Lead zirconate ( $\text{PbZrO}_3$  or PZ) is an important precursor in the preparation of a number of technologically important solid solutions, particularly those of the  $\text{PbZr}_{1-x}\text{Ti}_x\text{O}_3$  series [1-2]. Recently, new studies have revealed novel applications of PZ as a phase-transformation-induced electro-mechanical actuator and a pyroelectric sensor [3-4]. The findings resulted in the reviving of interest in the synthesis of nano-sized PZ powders. Along this line, various synthetic techniques are available, e.g. hydrothermal, vibro-milling, sol-gel and precipitation, each of which exhibits characteristic drawbacks. The formation of aggregates, for instance, is an inherent problem for the hydrothermal technique [5-8]. The synthesis of fine PZ powders composing of mono-dispersed particles of uniform shape and size by this technique is therefore a challenge. According to our previous study, the fine powders of

orthorhombic PZ could be synthesised as a single phase under hydrothermal conditions at a temperature of at least 180°C for 24 hours [8]. The space group of the resulting PZ was the unusual *Pbma* with refined cell parameters  $a=5.88(6)$  Å and  $c=4.27(3)$  Å. The formation of aggregates was the major drawback. Nonetheless, the highly dispersed and well-defined cubic particles could be afforded when the reaction temperature and time were increased to 200°C and 72 hours respectively [8]. The attempt to use organic additives, e.g. polyvinyl alcohol, polyvinylpyrrolidone and cetyltrimethylammonium bromide, which are commonly employed in the synthesis of other oxide powders [9-11], may be an answer to this problem, although they need to be removed in the post-synthesis step.

Herein, the application of the microwave heating in the synthesis of PZ fine powders under hydrothermal conditions is reported. The primary objective of the synthesis is to promote the mono-dispersion of particles of the synthesised PZ powders without the assistance of organic additives. The influences of various synthetic parameters on the obtained powders and the advantages and shortcomings of the microwave heating are described and discussed.

## MATERIALS AND METHODS

Equimolar mixtures of zirconyl nitrate hexahydrate [ $\text{ZrO}(\text{NO}_3)_2 \cdot 6\text{H}_2\text{O}$ , 27% Zr (gravimetric), Fluka, 0.0115 mole] and one of the following lead precursors, i.e. lead(II) nitrate (99.0%, Univar), lead(II) acetate (99.5%, Ajax Chemicals), lead(II) fluoride (99.0%, Univar), lead(II) chloride (99.0%, Riedel de Haën) and lead(II) iodide (99.0%, Aldrich), were prepared in 10.0 cm<sup>3</sup> of deionised water. Pellets of potassium hydroxide (85%, Merck) was gradually added to each mixture with stirring to a concentration ranging from 6 to 14 moles dm<sup>-3</sup>. Each mixture was then transferred to an 18-cm<sup>3</sup> Teflon reactor, which was sealed and placed in a 95(±5)°C water bath placed in a domestic microwave oven (Whirlpool XT-25ES/S, 900W, 2.45 GHz). The reaction was performed under autogenous pressure developed by the microwave heating (720W and 810W) for 3-5 hours. The resulting powder was recovered by filtration and washed with deionised water until the pH of the filtrate was approximately 7, followed a final washing with dilute acetic acid.

The synthesised powders were characterised for crystalline phases by powder X-ray diffraction (XRD) (using D8 Advance, Bruker, Cu  $K\alpha$ , Ni filter,  $\lambda=1.540598$  Å, 40 kV, 30 mA). A field-emission scanning electron microscope equipped with energy-dispersive X-ray spectrometer (JSM-6335F, Jeol) was used in the examination of particle shape and size and elemental composition. In order to evaluate the aggregation, size distributions of the bulk powder samples were measured by light scattering technique (using Zetasizer Nano S, Malvern Instruments, 4mW He-Ne laser operated at 633 nm, particle size range 0.3nm-10µm).

## RESULTS AND DISCUSSION

Although different lead precursors were used in the study, every reaction apparently provided the same off-white powders mixed with some red-block crystals, which were identified as lead oxide by XRD study. Although the contamination of lead oxide in the prepared powders seemed to be inevitable, they could be simply removed by washing with dilute acetic acid solution [12]. After the acid washing, it was found that only  $\text{Pb}(\text{NO}_3)_2$  gave the well crystallised PZ while poorly crystallised powders were

obtained from the other lead precursors as depicted in Figure 1. This could be attributed to the low solubility of these lead precursors in aqueous solution compared to the readily dissolved  $\text{Pb}(\text{NO}_3)_2$  [13]. The hardly dissolved lead precursors might bring about an insufficient nutrient in the solution and consequently the nucleation and crystal growth could not occur properly.

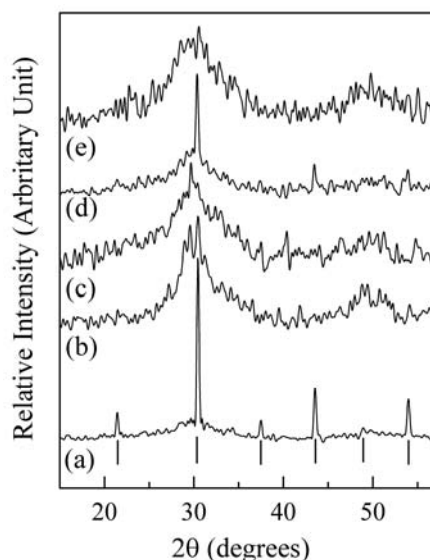


**Figure 1.** XRD patterns of the powders obtained from reactions between  $\text{ZrO}(\text{NO}_3)_2 \cdot \text{H}_2\text{O}$  and different lead precursors in  $14 \text{ mol dm}^{-3}$  KOH solution for 3 hours: (a)  $\text{Pb}(\text{NO}_3)_2$ , (b)  $\text{Pb}(\text{CH}_3\text{COO})_2$ , (c)  $\text{PbF}_2$ , (d)  $\text{PbCl}_2$  and (e)  $\text{PbI}_2$ . The vertical bars indicate diffraction characteristics of PZ (ICSD 077-0856).

For the  $\text{Pb}(\text{NO}_3)_2$  case, according to the XRD patterns of the acid-treated powders as shown in Figure 2, a very high KOH concentration of  $14 \text{ mol dm}^{-3}$  was required for the success of the synthesis. Lower concentrations resulted in poorly crystallised powders. However, a development in intensity of the  $(200)$  diffraction peak with increasing KOH concentration was apparent, suggesting the evolvement of the desired PZ. Another observation was a substantial reduction of the effective reaction time from days to hours when compared with the conventional hydrothermal synthesis [8].

According to former studies on similar issues, the observed phenomena could be explained as follows. Under commonly used hydrothermal conditions, the formation of nanocrystalline  $\text{ZrO}_2$  as the hydrolysis product of aqueous  $\text{ZrO}(\text{NO}_3)_2$  [14] could also be accelerated by microwave heating. This caused the breaking of large water clusters in the hydration sphere and the formation of the smaller ones [15]. Such mechanism increased the mobility of the dissolved lead species as well as the number of reaction sites on the occurring  $\text{ZrO}_2$  surfaces for the hydrated lead ion-water clusters to react. A rapid synthesis should therefore be expected. According to the same studies, the hydrolysis of the aqueous  $\text{ZrO}(\text{NO}_3)_2$  also resulted in the generation of nitric acid, which could neutralise the hydroxide species in solution [14]. In addition, there was evidence for the reduced electrolytic reaction of the KOH solution by the microwave radiation [16]. These phenomena were probably responsible for the increase in the high KOH concentration required in this study. This assumption was supported by the



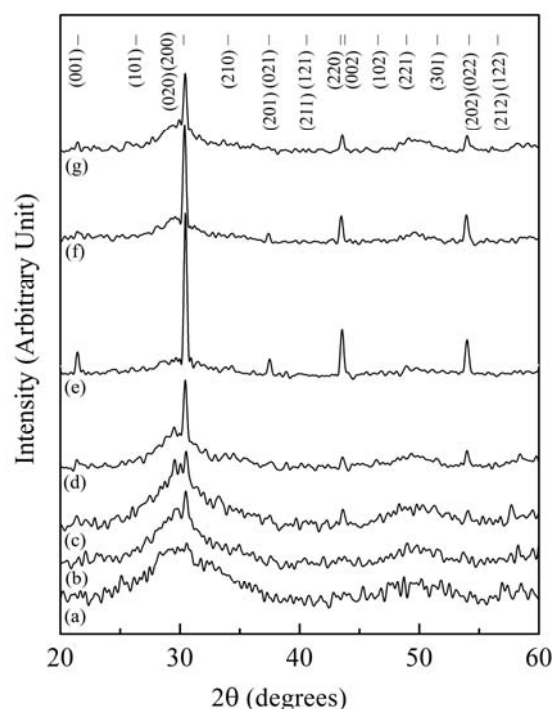


**Figure 2.** XRD patterns of the powders obtained from the reaction between  $\text{ZrO}(\text{NO}_3)_2 \cdot \text{H}_2\text{O}$  and  $\text{Pb}(\text{NO}_3)_2$  at 720 W for 3 hours in different concentrations of KOH solution: (a) 6 (b) 8 (c) 10 (d) 12 and (e) 14 moles  $\text{dm}^{-3}$ , compared to those obtained in 14 moles  $\text{dm}^{-3}$  KOH solution with different reaction times: (f) 4 hours and (g) 5 hours. The reference pattern is shown with vertical bars (ICSD 077-0856).

experiment in which a higher microwave power of 810 W was used. Rather than the desired PZ, mixtures of different oxides of lead and zirconium were obtained, which are the expected products of the hydrolysis reactions of the metal salts.

Based on the XRD patterns of the acid-treated powders, the synthesised PZ could be readily indexed as the orthorhombic *Pbma* phase with refined cell parameters  $a=5.87(1)$  Å,  $b=5.88(2)$  Å and  $c=4.15(2)$  Å (ICSD 077-0856). These results were well consistent with the conventional hydrothermal case, although the refined  $c$  parameter was shorter than the conventional heating case,  $c=4.27(3)$  Å [8], but closer to the standard,  $c=4.134$  Å (ICSD 077-0856).

The field-emission scanning electron microscopic (FESEM) images, as typically illustrated in Figure 3(a), showed that the powders largely consisted of discrete cubic particles although some particles with irregular shape were also present. The energy-dispersive X-ray spectroscopic measurements on the surface of several cubic particles indicated stoichiometric Pb:Zr, whereas the irregular-shape particles were found to be Zr-rich. This could account for the noisy background observed for the XRD patterns [Figure 2(e)]. The sizes of the cubic particles measured from the FESEM images were distributed in a significantly narrow range of 0.4–1.2  $\mu\text{m}$  with approximately 60% of the population having a size of about 1  $\mu\text{m}$  [Figure 4(a)]. Light scattering experiment on the bulk powder samples showed slightly larger particle sizes distributed mostly between 1–2  $\mu\text{m}$  [Figure 4(b)]. The difference in particle sizes obtained from the two techniques should be due to a potentially biased

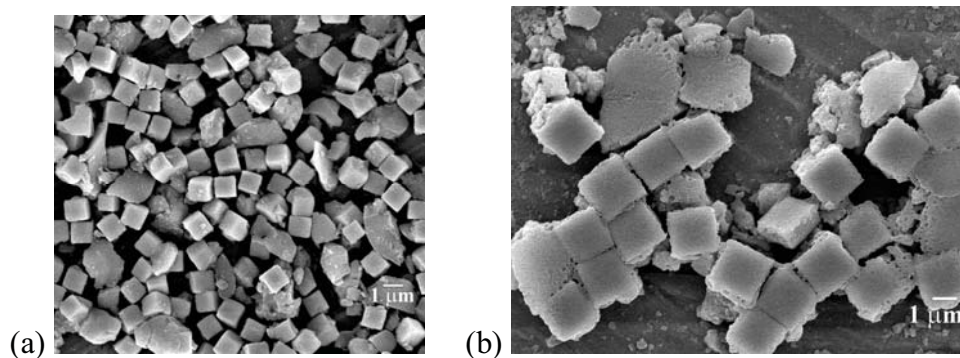


**Figure 3.** Typical FESEM photographs of PZ particles with corresponding XRD patterns shown in Figures 2(e) and 2(g) for crystals (a) and (b) respectively.

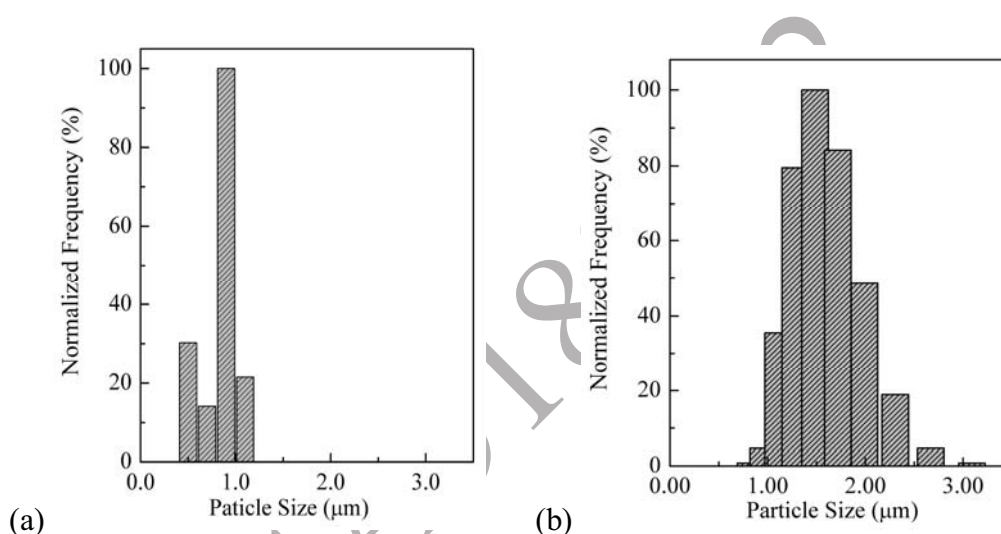


**Figure 4.** Particle size distribution of the cubic PZ particles measured from (a) FESEM images and (b) light scattering experiment (measured on the same powder sample)

analysis of the data. The non-spherical morphology of the particles normally introduces statistical errors to the laser light scattering data while a tendency of the particles to rest with preferred orientation on stub can induce bias in the data representation of the FESEM [17].

Thus, in comparison to the PZ powders derived from a conventional hydrothermal reaction where the particles were reportedly distributed in a 5-15  $\mu\text{m}$  range with an average diameter of 7.5  $\mu\text{m}$  [8], the pronouncedly narrower size distribution and the substantially smaller PZ particles have been achieved, although the negative effect on phase purity of the synthesised PZ and the contamination of some irregular Zr-rich particles were observed. A large number of nucleation induced by the localised microwave heating and the mechanism as described above, coupled with a poor crystal growth due to instantaneous and rapid ramping of such heating, could be the reasons for the approximate uniformity in the particle size [18-19]. Considering the PZ powders obtained from other chemical routes such as precipitation [20] and microemulsion [21], the apparent uniformity in particle shape and size may not be new. Both of these techniques can also give PZ powders composing of mono-dispersed spherical

particles typically 20 nm in diameter. However, calcination is required by both techniques, resulting in an unavoidable high temperature treatment and disadvantages incurred therein. As for the modified solid-state preparation of PZ powders, the problems with aggregation and particles with irregular shapes cannot be surmounted even though the vibro-milling is applied for over 25 hours [22].

The extension of the microwave heating time from 3 to 5 hours resulted in a reduction in intensity of the most intense (200) diffraction peak of the orthorhombic PZ and the appearing of a broad lump at the base of this peak as shown in Figure 2 (e-g). The FESEM images [Figure 3(b)] showed that the particles remained in the same cubic shape, although the bubbled surfaces and the necking between the adjacent particles could be observed. This indicated the boiling on the surfaces of these cubic PZ particles, which could be the result of a heat accumulation. The enlargement of the particles, which is a reflection of the particle growth process, and the disappearing of irregular particles with extended reaction time were also apparent.

## CONCLUSIONS

In order to promote the mono-dispersion and the uniformity in shape and size of the hydrothermally derived PZ particles without the assistance of organic additives, microwave heating was attempted. The occurrence of lead oxide seemed to be inevitable and washing with dilute acetic acid was necessary. Among different variables studied, the type of lead precursor and the KOH concentration were most critical in the success of the synthesis. It was shown that the critical KOH concentration and the optimal microwave heating time were 14 moles  $\text{dm}^{-3}$  and 3 hours respectively. The highly dispersed cubic lead zirconate particles of approximately 1  $\mu\text{m}$  in size could be synthesised in only 3 hour at 720 W of microwave heating. In comparison to conventional hydrothermal synthesis, the merits of the microwave method were clearly reflected by a shortening in hydrothermal reaction time, a reduction in particle size, an improved particle mono-dispersion, and a uniform particle size. However, the negative effects on the purity of synthesised powders, viz. the contamination of irregular particles, and the requirement for a very high concentration of potassium hydroxide mineraliser should be noted.

## ACKNOWLEDGEMENTS

This work is financially supported by Thailand Research Fund (TRF) and the Synchrotron Light Research Institute (Public Organisation). S. T. thanks the Royal Golden Jubilee Program of the TRF and the Graduate School of Chiang Mai University for their graduate scholarships.

## REFERENCES

1. T. Asada and Y. Koyama, "Ferroelectric domain structures around the morphotropic phase boundary of the piezoelectric material  $\text{PbZr}_{1-x}\text{Ti}_x\text{O}_3$ ", *Phys. Rev. B*, **2007**, 75, 214111-214121.
2. C. Z. Rosen, B. V. Hiremath and R. E. Newnham, "Key Papers in Physics; Piezoelectricity", American Institute of Physics, New York, **1992**, pp.159-181.
3. K. Yamakawa, S. Trolier-McKinstry and J. P. Dougherty, "Reactive magnetron co-sputtered antiferroelectric lead zirconate thin films", *Appl. Phys. Lett.*, **1995**, 67, 2014-2016.

4. P. Ayyub, S. Chattopadhyay, K. Sheshadri and R. Lahiri, "The nature of ferroelectric order in finite systems", *Nano Mater.*, **1999**, 12, 713-718.
5. O. Khamman, W. Chaisan, R. Yimnirun and S. Ananta, "Effect of vibro-milling time on phase formation and particle size of lead zirconate nanopowders", *Mater. Lett.*, **2007**, 61, 2822-2826.
6. E. D. Ion, B. Malic and M. Kosec, "Characterization of PbZrO<sub>3</sub> prepared using an alkoxide-based sol-gel synthesis route with different hydrolysis conditions", *J. Eur. Ceram. Soc.*, **2007**, 27, 4349-4352.
7. E. E. Oren, E. Taspinar and A. C. Tas, "Preparation of lead zirconate by homogeneous precipitation and calcination", *J. Am. Ceram. Soc.*, **1997**, 80, 2714-2716.
8. A. Rujiwatra, S. Tapala, S. Luachan, O. Khamman and S. Ananta, "One-pot hydrothermal synthesis of highly dispersed, phase-pure and stoichiometric lead zirconate", *Mater. Lett.*, **2006**, 60, 2893-2895.
9. G. Xu, G. Zhao, Z. Ren, G. Shen and G. Han, "PVA assisted synthesis of nanosized perovskite PZT powder by a two-stage precipitation route", *Mater. Lett.*, **2006**, 60, 685-688.
10. Z. Lu, J. Liu, Y. Tang and W. Li, "Hydrothermal synthesis of CaSnO<sub>3</sub> cubes", *Inorg. Chem. Commun.*, **2004**, 7, 731-733.
11. W. L. Sin, K. H. Wong and P. Li, "Surfactant effect on synthesis of nanocrystalline La<sub>x</sub>Sr<sub>1-x</sub>MnO<sub>3</sub> by hydrothermal method", *Acta Physica. Polonica. A*, **2007**, 111, 165-171.
12. S. Tapala, N. Thammajak, P. Laorattanakul and A. Rujiwatra, "Effects of microwave heating on sonocatalyzed hydrothermal preparation of lead titanate nanopowders", *Mater. Lett.*, **2008**, 62, 3685-3687.
13. J. G. Speight, "Lange's Handbook of Chemistry", 16th Edn., McGraw-Hill, New York, **2005**, Ch. 1.
14. Y. V. Kolen'ko, V. D. Maximov, A. A. Burukhin, V. A. Muhanov and B. R. Churagulov, "Synthesis of ZrO<sub>2</sub> and TiO<sub>2</sub> nanocrystalline powders by hydrothermal process", *Mater. Sci. Eng. C*, **2003**, 23, 1033-1038.
15. R. Walczak and J. A. Dziuban, "Microwave enhanced wet anisotropic etching of silicon utilizing a memory effect of KOH activation-A remote E2msi process", *Sens. Actuators A*, **2004**, 116, 161-170.
16. D. R. Stanisavljev, T. D. Grozdić, M. P. Marčeta Kaninski, A. R. Djordjević and D. Lj. Stojić, "The microwave influence on the electrolytic decomposition of KOH water solution", *Electrochem. Commun.*, **2007**, 9, 901-904.
17. A. Jillavenkatesa, S. J. Dapkunas and L.-S. H. Lum, "Particle Size Characterization; Practice Guide", U.S. Government Printing Office, Washington, D.C., **2001**, Ch. 5-6.
18. D. E. Clark and W. H. Sutton, "Microwave processing of materials", *Annu. Rev. Mater. Sci.*, **1996**, 26, 299-331.
19. P. Lidström, J. Tierney, B. Wathey and J. Westman, "Microwave assisted organic synthesis - A review", *Tetrahedron*, **2001**, 51, 9225-9283.
20. T. Ko and D. -K. Hwang, "Preparation of nanocrystalline lead zirconate powder by homogeneous precipitation using hydrogen peroxide and urea", *Mater. Lett.*, **2003**, 57, 2472-2479.



21. J. Fang, J. Wang, S. -C. Ng, L. -M. Gan, C. H. Quek and C. -H. Chew, "Synthesis of lead zirconate powders via a polyaniline-mediated microemulsion processing route", *Mater. Lett.*, **1998**, 36, 179-185.
22. O. Khamman, W. Chaisan, R. Yimnirun and S. Ananta, "Effect of vibro-milling time on phase formation and particle size of lead zirconate nanopowders", *Mater. Lett.*, **2007**, 61, 2822-2826.

© 2011 by Maejo University, San Sai, Chiang Mai, 50290 Thailand. Reproduction is permitted for noncommercial purposes.

RSA5180012

Full Paper

## Crystal growth and characterisation of a unique trinuclear $V^{IV}/V^V$ complex

Yothin Chimupala<sup>1</sup>, Wasinee Phonsri<sup>1</sup>, Timothy J. Prior<sup>2</sup> and Apinpus Rujiwatra<sup>1,\*</sup>

<sup>1</sup> Department of Chemistry and Centre for Innovation in Chemistry, Faculty of Science, Chiang Mai University, Chiang Mai 50200 Thailand

<sup>2</sup> Department of Chemistry, University of Hull, Kingston upon Hull, UK, HU6 7RX

\* Corresponding author, e-mail: [apinpus@chiangmai.ac.th](mailto:apinpus@chiangmai.ac.th)

Received: 10 August 2010 / Accepted: 15 February 2011 / Published: 28 February 2011

**Abstract:** Single crystals of a mixed-valence trinuclear cluster of formula  $[V_2^V V^{IV} O_5 (C_{12}H_8N_2)_3 (SO_4)_2 (H_2O)_3] \cdot 6H_2O$  were grown by layer diffusion technique and characterised by single-crystal X-ray diffraction;  $P2_1/c$ ,  $a = 20.5448(11)$  Å,  $b = 11.7647(9)$  Å,  $c = 18.1871(9)$  Å,  $\beta = 92.64(0)^\circ$ ,  $V = 4391.22(93)$  Å<sup>3</sup>,  $R = 0.0941$  and  $R_w = 0.1345$ . A distinct characteristic of the structure is the existence of the rare linear mono- $\mu$ -oxo  $[V_2^V V^{IV} O_5]^{4+}$  building units and the presence of a large number of hydrogen bonds and  $\pi$ - $\pi$  interactions. The study on the mixed valence state of vanadium by valence bond sum calculations, manganometric titration and cyclic voltammetry, and the presence of  $\pi$ - $\pi$  interactions by calculation of the harmonic oscillator model of aromaticity indices are presented. The thermogravimetric and differential scanning calorimetric analysis is also reported. The results of UV-Vis spectroscopic study and band gap energy calculation are included.

**Keywords:** vanadium complex, trinuclear complex, crystal structure, single-crystal X-ray diffraction

## INTRODUCTION

Prompted by a variety of valences and coordination chemistry that can be adopted by vanadium and a wide range of potential applications of its complexes [1-3], the interest in vanadium complexes has been unceasing, particularly in those of high nuclearity and mixed valence state. The bi-nuclear complexes containing a mono- $\mu$ -oxo  $[V_2O_3]^{2+}$  core are thus far the largest class in which the mixed valence state of vanadium is common. Examples of polynuclear  $V^{IV}/V^V$  complexes with mono- $\mu$ -oxo-

vanadium cores are still limited: the tetra-nuclear  $[V_4O_6(C_2H_5O)_6(C_{12}H_8N_2)_2]$ , penta-nuclear  $\{[V_2O_4(C_{12}H_8N_2)_2(PO_4)]_2VO(OH)\}_{3/4}\{[V_2O_4(C_{12}H_8N_2)_2(HPO_4)]_2\}_{1/4}\cdot 4.5H_2O$  and nona-nuclear  $K_7[V_9O_{16}(bdta)_4]\cdot 27H_2O$  (*bdta* = butanediaminetetraacetate) are known [4-6]. To the best of our knowledge, the first example of the tri-nuclear vanadium complex of this kind with a chemical formula of  $[VO_2(phen)(SO_4)(H_2O)]_2[VO(phen)(H_2O)]\cdot 4H_2O$  (*phen* = phenanthroline ligand) was reported by Huang et al. in 2008 [7]. Its hydrothermal synthesis and the novel characteristic of its structure in exhibiting a practically linear  $[V_3O_5]^{4+}$  core were reported with a brief description on the EPR and UV-Vis study of the complex.

As a continuation of our interest in the synthesis of new polyoxovanadates using organodiamines of different molecular flexibility and aromaticity, we embark on the synthesis and growing of single crystals of compound  $[V_2^V V^{IV} O_5(C_{12}H_8N_2)_3(SO_4)_2(H_2O)_3]\cdot 6H_2O$  (**1**). Although reported earlier [7], the synthesis and crystal growth of **1** by a different route carried out in this study and a detailed description of its crystal structure should be worth reporting. Different ways of determining the mixed valence state of vanadium are presented. The UV-Vis spectroscopic study, cyclic voltammetric analysis and thermogravimetric-differential scanning calorimetric analysis of **1** were also performed.

## MATERIALS AND METHODS

### Chemicals

All chemicals were used as-received: 1,10-phenanthroline ( $C_{12}H_8N_2$ ; Fluka, 99%), ethyl alcohol (Merck, 99.9%), ammonium metavanadate (Ajax, 99.5%), sodium hydroxide (Merck, 99%), sulfuric acid (Merck, 95-97%), potassium permanganate (BDS, 99%), sodium sulphite (Ajax, 98%) and potassium bromide (BDH 98.5%).

### Crystal Growth and Characterisation

An ethanolic solution of organic ligand (solution A) was prepared by dissolving 0.495 g of 1,10-phenanthroline (*phen*) in  $15.0\text{ cm}^3$  of ethyl alcohol. An aqueous solution of  $VO_2^+$  (solution B) was prepared by dissolving 2.00 g of ammonium metavanadate in  $50.0\text{ cm}^3$  of warm  $1.00\text{ mol dm}^{-3}$  sodium hydroxide solution, followed by addition of  $80.0\text{ cm}^3$  of  $1.00\text{ mol dm}^{-3}$  sulfuric acid. A portion of solution B ( $1.50\text{ cm}^3$ ) was gently loaded into a glass test tube of 5 mm in diameter and 10 cm in length, followed by  $1.50\text{ cm}^3$  of solution A. Dark green crystals of **1** appeared at the boundary between solutions A and B after leaving for 5 days at atmospheric condition.

The elemental composition of the crystals was semi-quantified using an energy-dispersive X-ray microanalyser equipped with a field-emission scanning electron microscope (JEOL JSM-6335F), whereupon a consistent V:S:O:C:N atomic ratio of 2.8:1.0:3.2:6.7:1.5 (exp.) compared to 2.4:1.0:5.5:6.7:1.3 (calc.) was obtained. A Fourier transform infrared (FTIR) spectrum of the ground crystals as a KBr pellet was collected on a Bruker Tensor 27 FT-IR instrument ( $4000\text{--}400\text{ cm}^{-1}$ , resolution  $0.5\text{ cm}^{-1}$ ):  $3450\text{ cm}^{-1}$ ,  $\nu(\text{O--H})$ ;  $3065\text{ cm}^{-1}$ ,  $\nu(\text{aromatic C--H})$ ; 1626, 1583, 1519 and  $1427\text{ cm}^{-1}$ ,  $\nu(\text{aromatic C=C})$ ; 1187, 1125 and  $1032\text{ cm}^{-1}$ ,  $\nu(\text{SO}_4)$ ; 970 and  $937\text{ cm}^{-1}$ ,  $\nu(\text{V=O})$ ; 870, 848, 778, 736 and  $723\text{ cm}^{-1}$ ,  $\delta_{\text{oop}}(\text{aromatic C-H})$ ; 647 and  $593\text{ cm}^{-1}$ ,  $\delta(\text{V--O--V})$ .

The purity of **1** was assured by X-ray powder diffraction pattern collected on a Bruker D8 Advance diffractometer (Ni filter, Cu  $K\alpha$ ,  $\lambda=1.540558$  Å, 48 kV, 30 mA). In order to determine the amount of  $V^{IV}$  and total  $V^{IV,V}$ , the aqueous solutions of **1** and its reduced form were titrated against standardised potassium permanganate solution. The solution of the reduced form of **1** was obtained by a reaction with sulphur dioxide generated from sodium sulphite. Cyclic voltammetry (CV) was also conducted using a BAS CV-50W voltammetric analyser (Bioanalytical System, Inc., USA) with Pt (MF-2013, 1.6 mm in diameter), Ag/AgCl (MF-2063) and Pt wire (MW-1032) as working, reference and auxiliary electrodes respectively.

Thermogravimetric-differential scanning calorimetric (TG-DSC) analysis was performed using ETZSCH STA 409 PC/PG thermal analyser (Netzsch-Gerätebau GmbH, Germany) (20-1200°C, rate 10°C/min,  $N_2$  gas) to evaluate the thermal stability of **1**. A UV-Vis spectrum of an aqueous solution of **1** from 200 nm to 800 nm was measured with a Perkin Elmer UV LAMDA 25 spectrophotometer. The loss of crystal colour after complete dissolution was noted.

### Crystal Structure Determination

Data of 8699 independent reflections were collected in a range of  $2.5 \leq \theta / ^\circ \leq 26.1$  on a  $0.45 \times 0.25 \times 0.15$  mm<sup>3</sup> greenish lozenge crystal of **1** using a Stoe IPDS2 diffractometer (Stoe & Cie GmbH, Germany) and Stoe X-Area software [8]. A face indexed absorption correction was applied within the Stoe X-RED software using Tompa method [9-10]. The data were then reduced and refined resulting in 5365 reflections with  $I > 2\sigma(I)$  and internal R of 0.070. The structure was determined by direct method and refined by full-matrix least-square methods using SHELXS97 and SHELXL97 programs via the WinGx program interface [11-13]. The structure was solved and refined in  $P2_1/c$ ,  $a = 20.5448(11)$  Å,  $b = 11.7647(9)$  Å,  $c = 18.1871(9)$  Å,  $\beta = 92.64(0)^\circ$ ,  $V = 4391.22(93)$  Å<sup>3</sup>,  $Z = 4$ ,  $R = 0.0941$  and  $R_w = 0.1345$ . The data were of reasonable quality. However, it was not possible to locate hydrogen atoms of the included water molecules. Some disorder in the positions of the water molecules was also detected. Details on data collection and structural deduction and refinement are summarised in Table 1. A rather large deviation of the goodness of fit from unity due to local disorder in the structure of **1** may be noted.

The structure of **1** was first reported by Huang et al. in 2008 [7]. The synthesis by hydrothermal route and the uniqueness of the complex as the first mixed-valence polynuclear vanadium with linear mono- $\mu$ -oxo  $[V_3O_5]^{4+}$  core were briefly reported. The study of the EPR and electronic spectrum was included. Crystallographic data of the formerly reported structure were compared with the presently reported structure as shown in Table 1, which suggests an approximate equivalence.



**Table 1.** Crystal data and structure refinement for **1**

	<b>1</b>	Data abstracted from Huang et al. [7]
Formula	$[V_2^V V^{IV} O_5(phen)_3(SO_4)_2(H_2O)_3] \cdot 6H_2O$	$[VO_2(phen)(SO_4)(H_2O)]_2[VO(phen)(H_2O)] \cdot 4H_2O$
	O	
Formula weight	1117	1091.66
Crystal description	Dark green	N/A
Crystal system	Monoclinic	Monoclinic
Space group	$P2_1/c$	$P2_1/c$
$a/\text{\AA}$	20.5448(11)	20.747(4)
$b/\text{\AA}$	11.7647(9)	11.828(2)
$c/\text{\AA}$	18.1871(9)	18.316(4)
$\beta / ^\circ$	92.639(4)	93.07(3)
Unit cell volume/ $\text{\AA}^3$	4391.2(5)	4488.2(16)
$Z$	4	4
$\rho_{\text{calc}}/\text{g.cm}^{-3}$	1.691	1.616
$T/\text{K}$	150(4)	293(2)
Radiation ( $\lambda/\text{\AA}$ )	Mo $K_\alpha$ (0.71073)	Mo $K_\alpha$ (0.71073)
Total data collected	24523	37068
$R_{\text{int}}$	0.070	0.0384
Data ( $I > 2\sigma(I)$ )	8699	10059
Goodness of fit ( $S$ )	0.797	1.049
$R, R_w$ (all data)	0.0941, 0.1345	N/A
$R, R_w(I > 2\sigma(I))$	0.055, 0.135	0.0558, 0.1488

## RESULTS AND DISCUSSION

### Crystal Structure of **1**

Compound **1**,  $[V_2^V V^{IV} O_5(C_{12}H_8N_2)_3(SO_4)_2(H_2O)_3] \cdot 6H_2O$ , crystallises in monoclinic space group  $P2_1/c$  with cell parameters  $a = 20.5448(11) \text{ \AA}$ ,  $b = 11.7647(9) \text{ \AA}$ ,  $c = 18.1871(9) \text{ \AA}$ ,  $\beta = 92.64(0)^\circ$ ,  $V = 4391.22(93) \text{ \AA}^3$  and  $Z = 4$ , which are similar to those of the previously reported structure [7]. Figure 1 shows an asymmetric unit of **1**, depicting three distinct vanadium atoms linked by two  $\mu_2$ -O11 and  $\mu_2$ -O12 to form an approximately linear trinuclear vanadium oxide backbone with bond angles being close to linearity:  $V1-O11-V2 = 163.1^\circ$  and  $V(2)-O(12)-V(3) = 159.2^\circ$ . Selected bond lengths and bond angles in **1** are listed in Table 2 and Table 3 respectively. The terminal V1 and V3 share the common distorted octahedral geometry, coordinated to two N atoms of the chelating *phen* and four O atoms from a monodentate sulphate, a terminal aqua ligand, the vanadyl bond and the oxo-bridge. Similar distorted octahedral geometry is adopted by the mediating V2, coordinated to two N atoms of the chelating *phen*, two *trans*  $\mu_2$ -O atoms of oxo-bridges, and the vanadyl and sulfate O atoms. The chemical formula of  $[V_3O_5(phen)_3(SO_4)_2(H_2O)_3]$  can thus be derived. A common question for polynuclear vanadium complexes is, however, the valence states of the vanadium atoms.

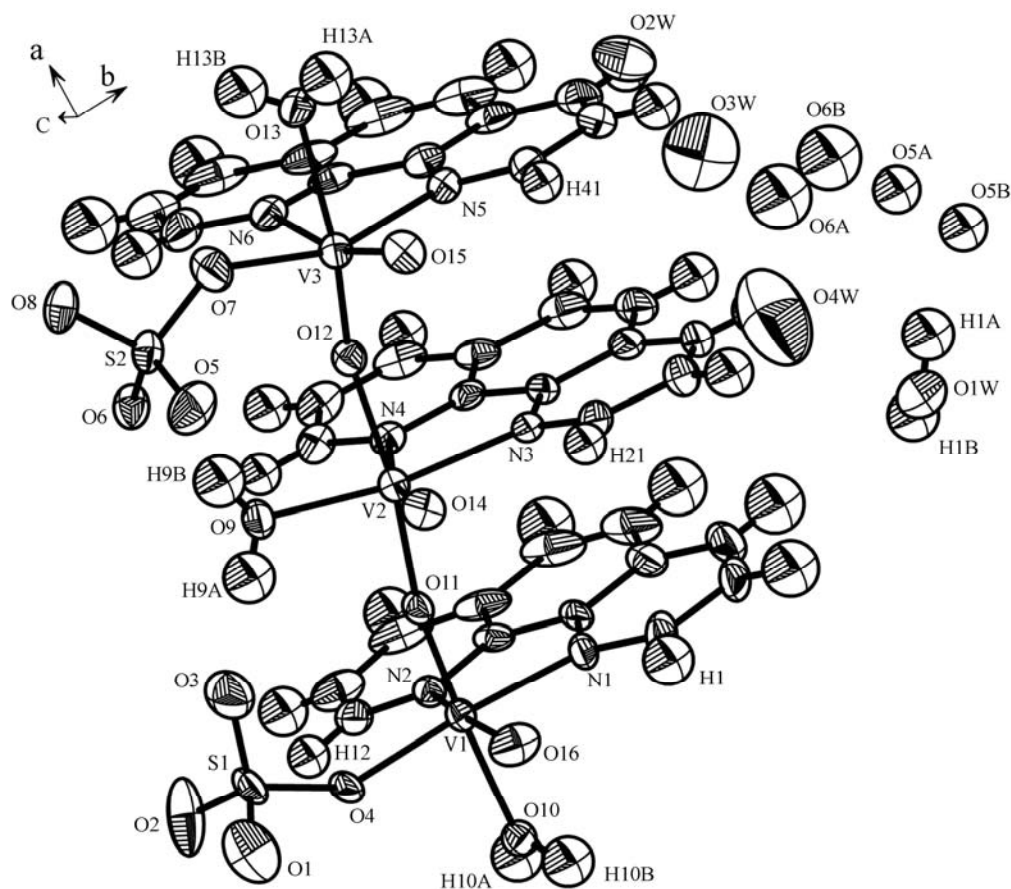


**Figure 1.** Asymmetric unit of **1** with atomic numbering scheme and drawn with 50% thermal elliptical possibility

**Table 2.** Selected bond distances (Å) in **1** with standard deviations in brackets

V1—O16	1.600(3)	V3—O12	1.677(3)
V1—O11	1.675(3)	V3—O7	1.930(3)
V1—O4	1.917(3)	V3—O13	2.123(4)
V1—N1	2.132(4)	V3—N5	2.136(4)
V1—O10	2.149(4)	V3—N6	2.296(4)
V1—N2	2.249(3)	S2—O5	1.430(4)
V2—O14	1.592(3)	S2—O8	1.455(3)
V2—O12	1.932(3)	S2—O6	1.468(3)
V2—O11	1.947(3)	S2—O7	1.521(4)
V2—O9	1.998(3)	S1—O2	1.421(4)
V2—N3	2.124(4)	S1—O1	1.457(4)
V2—N4	2.307(3)	S1—O3	1.462(5)
V3—O15	1.596(3)	S1—O4	1.510(3)

**Table 3.** Selected bond angles (°) in **1** with standard deviations in brackets

O16—V1—O11	104.73(16)	O12-V2-N3	87.57(13)	N5-V3-N6	73.96(13)
O16—V1—O4	104.79(18)	O11-V2-N3	96.01(13)	O5-S2-O8	113.5(2)
O11—V1—O4	99.86(14)	O9-V2-N3	159.64(14)	O5-S2-O6	111.2(2)
O16—V1—N1	92.14(18)	O14-V2-N4	166.12(15)	O8-S2-O6	110.40(19)
O11—V1—N1	88.54(15)	O12-V2-N4	80.55(12)	O5-S2-O7	109.1(2)
O4 —V1—N1	158.32(14)	O11-V2-N4	82.81(12)	O8-S2-O7	103.9(2)
O16—V1—O10	87.57(16)	O9-V2-N4	86.43(14)	O6-S2-O7	108.3(2)
O11—V1—O10	165.39(13)	N3-V2-N4	73.57(13)	O2-S1-O1	109.3(3)
O4 —V1—O10	84.22(13)	O15-V3-O12	104.37(16)	O2-S1-O3	116.4(3)
N1 —V1—O10	83.05(14)	O15-V3-O7	104.52(17)	O1-S1-O3	105.5(3)
O16—V1—N2	161.26(17)	O12-V3-O7	97.97(15)	O2-S1-O4	106.8(2)
O11—V1—N2	88.14(14)	O15-V3-O13	93.89(15)	O1-S1-O4	107.2(2)
O4 —V1—N2	85.91(13)	O12-V3-O13	161.30(13)	O3-S1-O4	111.2(2)
N1 —V1—N2	74.35(14)	O7-V3-O13	81.01(15)	S1-O4-V1	140.7(2)
O10-V1-N2	78.10(13)	O15-V3-N5	89.66(15)	S2-O7-V3	137.3(2)
O14-V2-O12	99.86(15)	O12-V3-N5	95.24(14)	V1-O11-V2	163.10(18)
O14-V2-O11	98.38(15)	O7-V3-N5	157.48(16)	V3-O12-V2	159.23(18)
O12-V2-O11	161.23(12)	O13-V3-N5	80.64(14)		
O14-V2-O9	107.45(16)	O15-V3-N6	162.33(16)		
O12-V2-O9	85.36(14)	O12-V3-N6	84.12(14)		
O11-V2-O9	85.00(13)	O7-V3-N6	89.31(16)		
O14-V2-N3	92.56(15)	O13-V3-N6	77.20(13)		

The bond valence sum (BVS) calculation was attempted using the refined bond lengths listed in Table 2 with the following assumed parameters:  $R_0(V^{V,IV}-O^{II}) = 1.735$ ,  $R_0(V^V-O^{II}) = 1.803$ ,  $R_0(V^{IV}-O^{II}) = 1.780$ ,  $R_0(V^{V,IV}-N^{III}) = 1.875$ , and  $b = 0.370$  [14]. The BVS of 4.81, 4.15 and 4.85 were obtained for V1, V2 and V3 respectively, indicating the presence of the expected  $V^{IV}$  and  $V^V$  with twice the amount of the latter. The result of manganometric titration confirms the calculation: 0.915 mol of  $V^{IV}$  per formula unit. The CV analysis confirms this by the presence of an irreducible reduction peak of  $V^V$  to  $V^{IV}$  at +0.242 V vs Ag/AgCl with a maximum current of 4.48 A. Based on the BVS calculation, manganometric titration and the CV experiment, a mixed  $2V^V:V^{IV}$  valence state for vanadium and the precise formula of  $[V_2^V V^{IV} O_5 (C_{12}H_8N_2)_3 (SO_4)_2 (H_2O)_3]$  can thus be deduced. This leads to the conclusion on charge neutrality for the cluster, which confirms the presence of only water molecules as the extra-cluster species and justifies the assignment of the extra-cluster O atoms as water during the crystal structure deduction and refinements. The chemical formula with six extra-cluster water molecules, viz.  $[V_2^V V^{IV} O_5 (C_{12}H_8N_2)_3 (SO_4)_2 (H_2O)_3] \cdot 6H_2O$ , is then established.

The phenanthroline (*phen*) ligands are located on the same side of the vanadium oxide backbone with the distances of 3.689 Å and 3.670 Å between the centroids of two adjacent molecular planes as shown in Figure 2. These distances are in a range possible for the  $\pi$ - $\pi$  interactions to occur [15-17], which can be regarded as an important parameter regulating the spatial arrangement of these chelating ligands. It is apparent that these phenanthroline ligands are not exactly parallel to each other but slightly converge towards the free end of the molecule. Figure 3 depicts the centroids of the central benzene rings of the *phen* ligands, showing the panning angles of 9.48° and 21.80° for the superjacent and subjacent ligands from the middle one. The relative arrangement of these organic ligands indicates that other interactions are present that subjugate the weak  $\pi$ - $\pi$  interactions, which favour the superimposed position of the ligands.

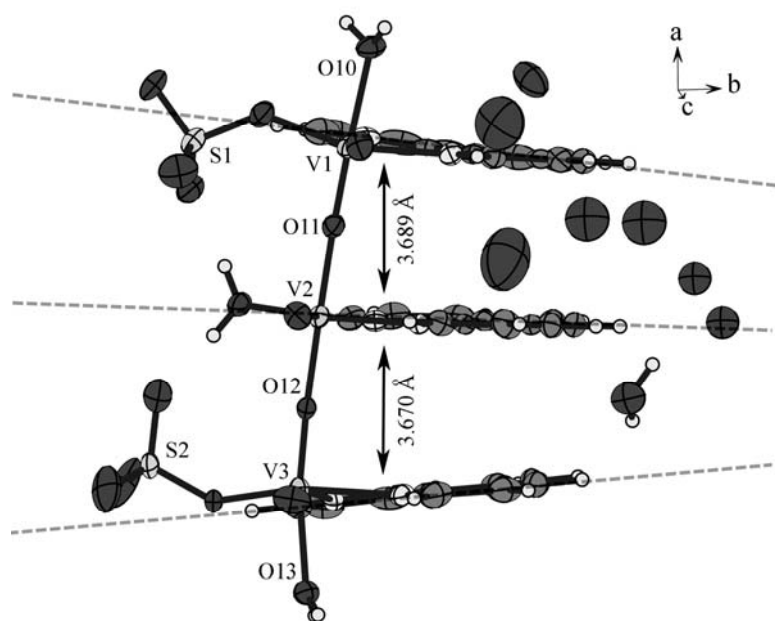


**Figure 2.** Illustration showing the relative spatial arrangement of *phen* and the corresponding inter-molecular planar distances

The interaction between  $\pi$  electrons commonly encountered in the stacking of aromatic molecules should impart an influence on their aromaticity. Here, the harmonic oscillator model of aromaticity (HOMA) index was used to evaluate the presence of this interaction [18-20]. According to a survey of structures consisting of *phen* in the molecules both in coordination and non-coordination modes found in the Cambridge structural databases [21], it is evident that the values of HOMA indices are distributed in different ranges depending on both the coordination and the  $\pi$ - $\pi$  interaction. For non-coordinated *phen*, the average indices of three fused benzene rings are distributed in a range of 0.25-0.50 for those without  $\pi$ - $\pi$  interactions and 0.66-0.83 for those with the interactions. On the other hand, the presence of  $\pi$ - $\pi$  interactions seems to be common with coordination with average indices distributed in a higher range of 0.70-0.94, suggesting the preference of these aromatic ligands to arrange themselves in such a way as to maximise the interactions. In the structure of **1**, the HOMA indices were calculated at similar values of ca. 0.80 for each *phen* ligand. This is in very good



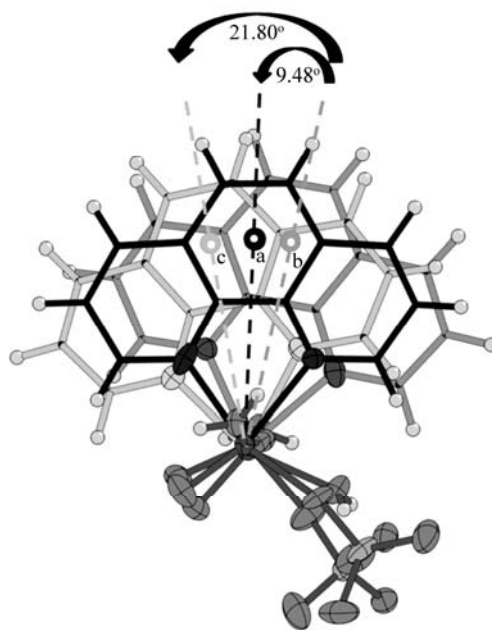


**Figure 3.** Illustration showing relative locations of the centroids (*a*, *b* and *c*) of the central benzene rings of the superjacent, middle and subjacent *phen* ligands respectively, with relative panning angles of *a* and *c* from *b*

agreement with the surveyed HOMA indices for those complexes with  $\pi$ - $\pi$  interacting *phen* ligands, hence the suggested presence of such weak interaction in **1**.

The analysis for hydrogen bonding according to the definition proposed by Jeffrey [22] was performed on the crystal structure and revealed a large number of hydrogen bonding interactions as depicted in Figure 4 and listed in Table 4. The weak C-H...O hydrogen bonds formed between *phen* and the neighbouring O atoms of both ligated and free water molecules as well as the nearby sulphate group may account for the subjugation of the  $\pi$ - $\pi$  interactions and the consequent orientation of these organic ligands. The strong hydrogen bonds of O-H...O type between the ligated water of the mediated V2 and the nearby sulphates also provide explanation for the orientation of the pending SO<sub>3</sub> motifs of V1 and V3 that incline towards each other with the bending angles of 140.71° and 137.32° for V1-O3-S1 and V3-O7-S2 respectively.

Compared to the complex, [VO<sub>2</sub>(*phen*)(SO<sub>4</sub>)(H<sub>2</sub>O)]<sub>2</sub>(VO(*phen*)(H<sub>2</sub>O)]·4H<sub>2</sub>O, reported by Huang et al. [7], structure **1** contains two more molecules of water of crystallisation and therefore a larger number of hydrogen bonding interactions. This may stem from the difference in crystal growth technique and condition. Crystals of **1** were grown at ambient temperature and pressure, whereas those of the former were obtained hydrothermally. The larger number of water outside the coordination sphere, however, does not significantly affect the solid state registry of the compound.

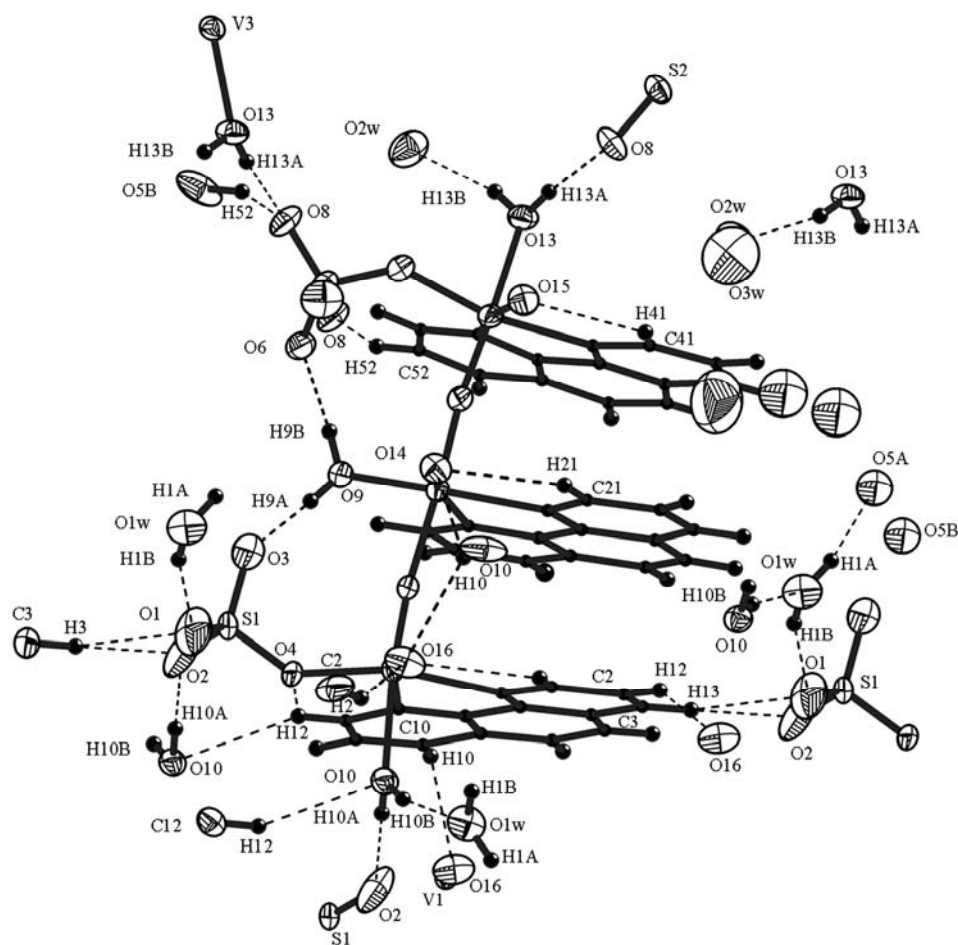


**Figure 4.** Hydrogen bonding interactions (dotted lines) of different types as listed in Table 4

### UV-Vis Spectroscopic Study

The UV-Vis spectrum measured on the aqueous solution of **1** at a concentration of  $5 \times 10^{-4} \text{ mol dm}^{-3}$  (Figure 5) exhibits absorption only in the UV region. The absorption bands characteristic of *phen* are clearly present with the maxima at 230 nm ( $3,205 \text{ dm}^3 \text{ mol}^{-1} \text{ cm}^{-1}$ ) and 264 nm ( $2,150 \text{ dm}^3 \text{ mol}^{-1} \text{ cm}^{-1}$ ), both of which are attributable to the intraligand  $\pi-\pi^*$  transitions. The most intense band at 206 nm ( $10,584 \text{ dm}^3 \text{ mol}^{-1} \text{ cm}^{-1}$ ) can be assigned to the LMCT process of the terminal oxygen while a broad band appearing as shoulder at 270 nm is the characteristic band associated to the LMCT of the bridging oxygen [23-25]. The absorption coefficients ( $\alpha$ ) can be calculated from the maximum ( $\lambda_{\text{max}}$ ) of each band, and the plot between  $(\alpha h\nu)^2$  and  $h\nu$  can be made (inset of Figure 5) if only the direct electronic transition is assumed [26]. The band gap energy for each transition can be obtained by extrapolation of the positive tangent line for each  $h\nu$  to  $\alpha=0$ : 4.3017, 5.2317 and 5.8182 eV for the transitions with  $\lambda_{\text{max}}$  at 264, 230 and 206 nm respectively.

**Table 4.** Summary of hydrogen bonding geometry for **1** (Standard deviations are in brackets)

D	A	H...A (Å)	D...A (Å)	∠ D-H...A (°)
O1 <sub>w</sub>	O5 <sub>A</sub>	2.17(5)	2.981(7)	158(5)
O1 <sub>w</sub>	O1	1.99(4)	2.807(5)	161(6)
O9	O3	1.72(4)	2.560(5)	175(7)
O9	O6	1.76(4)	2.604(5)	176(5)
O10	O2	1.91(4)	2.750(5)	179(7)
O10	O1 <sub>w</sub>	1.87(5)	2.690(5)	164(5)
O13	O8	1.82(5)	2.656(5)	174(5)
O13	O2 <sub>w</sub>	1.93(5)	2.728(5)	163(4)
C1	O16	2.57	2.994(7)	108
C2	O16	2.46	3.308(7)	149
C3	O1	2.50	3.270(7)	138
C3	O2	2.35	3.272(8)	163
C10	O14	2.56	3.243(7)	129
C10	O16	2.49	3.212(7)	133
C12	O4	2.56	3.058(5)	113
C12	O10	2.57	3.365(6)	142
C21	O14	2.49	2.957(6)	110
C41	O15	2.43	2.894(6)	110
C52	O8	2.45	3.246(7)	142

It is intriguing that there was no absorption in the visible light region (325-800 nm) for the solution of **1**, which was also colourless. This might be due to the loss of long-range order of the solid state structure when it was made into solution. It has been reported, however, that a broad absorption band which should be evidence for the inter-valence charge transfer between V<sup>IV</sup> and V<sup>V</sup> was observed in this region for the spectrum collected on a solid sample [7].

### Thermogravimetric and Differential Scanning Calorimetric Analysis

On heating **1** under the flow of N<sub>2</sub> gas, four stages of endothermic weight loss were observed (Figure 6). The first weight loss of 9.86% occurring between 80-150°C agrees well with the weight of six non-coordinating water molecules (9.58%), while the second loss of 5.14% observed at 150-340°C is approximately equivalent to the weight of three coordinating water molecules (4.79%). The corresponding endothermic features found in the DSC curve reflect the influence of the hydrogen bonding interactions involved with these water molecules. The next two subsequent weight losses found from 340°C to 700°C totalled 45.00%, which corresponds well with the release of three coordinated *phen* ligands. It should be noted that the argument is made based only on the agreement of weight percentages; further experiments on identification of the liberated species have to be performed if a definite conclusion is to be obtained.

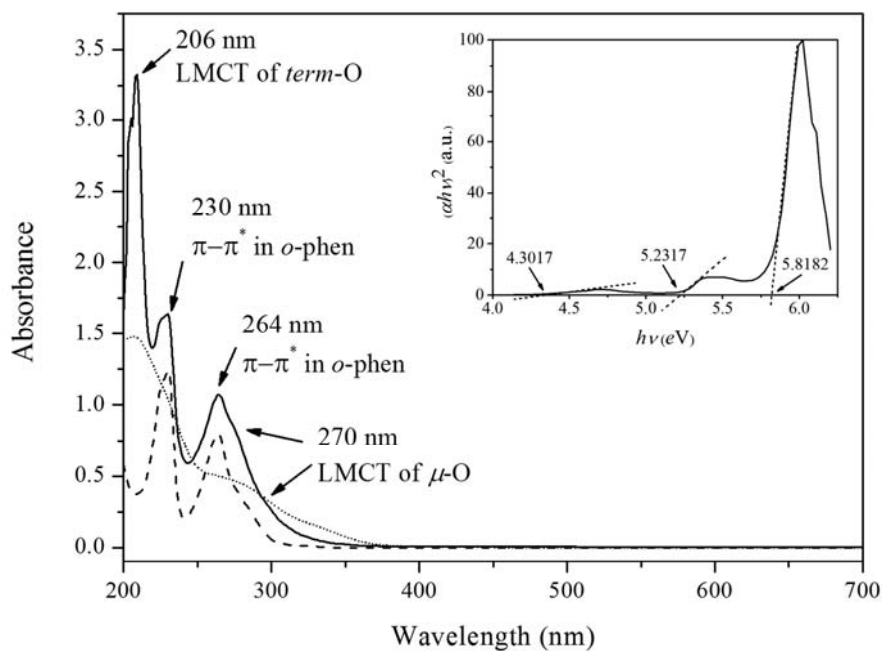


**Figure 5.** The UV-Vis spectrum of aqueous solution of **1** ( $5 \times 10^{-4} \text{ mol dm}^{-3}$ , solid line) compared with those of the ligand (dash line) and vanadium precursor (dotted line). The plot between  $(\alpha h\nu)^2$  and  $h\nu$  is provided in the inset

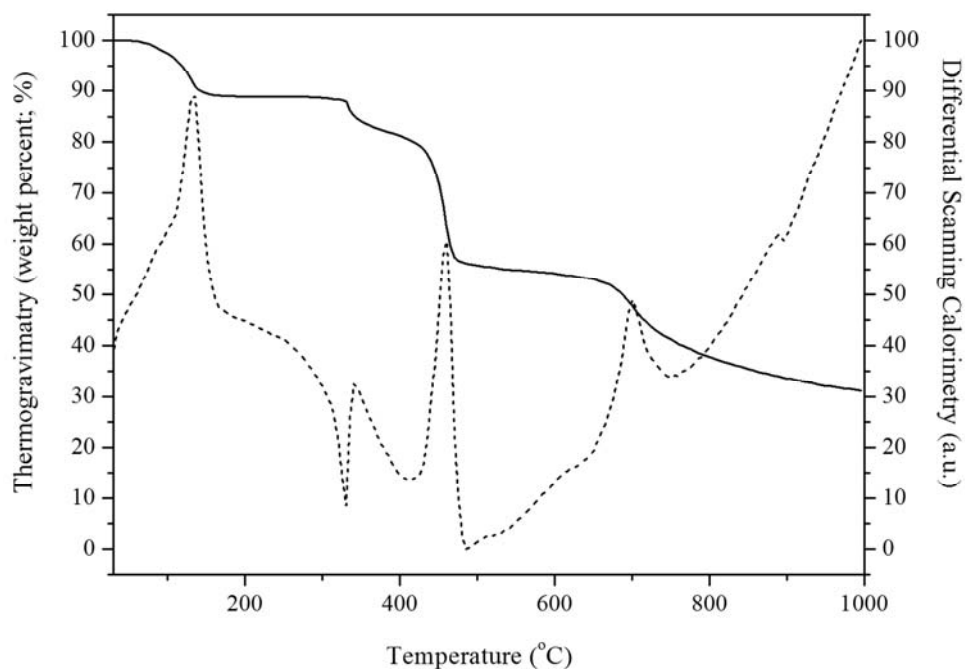


**Figure 6.** Thermogravimetric (solid line) and differential scanning calorimetric (dash line) graphs collected on **1**



## CONCLUSIONS

A rare example of mixed-valence trinuclear cluster,  $[V_2^V V^{IV} O_5 (C_{12}H_8N_2)_3 (SO_4)_2 (H_2O)_3] \cdot 6H_2O$ , has been synthesised at ambient atmosphere. Its crystal structure has been determined and refined with excellent agreement with the previously reported structure which had fewer water of crystallisation. Detailed analysis of the structure indicates the presence of both  $\pi$ - $\pi$  interactions and a large number of intra- and inter-cluster hydrogen bonds, which impart influence on spatial orientation of the cluster-building motifs. According to the bond valence sum calculations, the manganometric titration and cyclic voltammetry, the mixed valence of  $V^{IV}$  and  $V^V$  in the ratio of 1:2 can be deduced. The presence of six molecules of water of crystallisation is consistent with the results of the thermogravimetric/differential scanning calorimetric analysis, which suggest sequential loss of water of crystallisation, ligated water and the phenanthroline ligands.

## ACKNOWLEDGEMENTS

This work is financially supported by the Thailand Research Fund (TRF). Y. C. and W. P. thank the Graduate School of Chiang Mai University and the Development and Promotion of Science and Technology Talent Project, Institute for Promotion of Teaching Science and Technology for graduate scholarships.

## SUPPLEMENTARY MATERIAL

Crystallographic data for compound **1** is available as supplementary material of this article in cif format [[download](#)].

## REFERENCES

1. M. R. Maurya and A. Kumar, "Oxovanadium (IV) based coordination polymers and their catalytic potentials for the oxidation of styrene, cyclohexene and *trans*-stilbene", *J. Mol. Catal. A: Chem.*, **2006**, 250, 190-198.
2. C. Hiort, J. Goodisman and J. C. Dabrowiak, "Cleavage of DNA by the insulin-mimetic compound  $NH_4[VO(O_2)_2(phen)]$ ", *Biochem.*, **1996**, 35, 12354-12362.
3. J. H. Hwang, R. K. Larson and M. M. Abu-Omar, "Kinetics and mechanistic studies of anti-carcinogenic bisperoxovanadium(V) compounds: Ligand substitution reactions at physiological pH and relevance to DNA interactions", *Inorg. Chem.*, **2003**, 42, 7967-7977.
4. L. Mafra, F. A. Almeida Paz, F. Shi, C. Fernandez, T. Trindade, J. Klinowski and J. Roch, "A pentanuclear oxovanadium(V) phosphate complex with phenanthroline", *Inorg. Chem. Commun.*, **2006**, 9, 34-38.
5. H. Kumagai, M. Endo, S. Kawata and S. Kitagawa, "A mixed-valence tetranuclear vanadium(IV,V) complex  $[V_4O_4(\mu-OEt)_2-(\mu-O)_2(OEt)_4(phen)_2]$ ", *Acta Crystallogr. C*, **1996**, 52, 1943-1945.
6. J. P. Launay, Y. Jeannin and M. Daoudi, "Mixed-valence complexes containing the  $V_2O_3^{3+}$  core. Structure and properties of  $H[V_2O_3(pmida)_2] \cdot 4H_2O$  and  $K_7[V_9O_{16}(bdta)_4] \cdot 27H_2O$ ", *Inorg. Chem.*, **1985**, 24, 1052-1059.

7. X. H. Huang, C. C. Huang, X. H. Qin, L. S. Zhai and D. S. Liu, "A novel mixed-valence vanadium(IV/V) complex containing linear mono- $\mu$ -oxo  $[V_3O_5]^{4+}$  core", *Inorg. Chem. Commun.*, **2008**, *11*, 1236-1238.
8. Stoe & Cie X-Area (Version 1.18), Stoe & Cie, Darmstadt, Germany (**2002**).
9. Stoe & Cie X-RED (Version 1.04), Stoe & Cie, Darmstadt, Germany (**2002**).
10. J. D. Meulener and H. Tompa, "The absorption correction in crystal structure analysis", *Acta Crystallogr.*, **1965**, *19*, 1014-1018.
11. G. M. Sheldrick, "SHELXS-97: Program for solving crystal structure", University of Gottingen, Germany (**1997**).
12. G. M. Sheldrick, "SHELXL-97: Program for crystal structure refinement", University of Gottingen, Germany (**1997**).
13. L. J. Farrugia, "WinGX Suite for small-molecule single-crystal crystallography", *J. Appl. Crystallogr.*, **1999**, *32*, 837-838.
14. V. S. Urusov and I. P. Orlov, "State-of-art and perspectives of the bond-valence model in inorganic crystal chemistry", *Crystallogr. Rep.*, **1999**, *44*, 686-709.
15. F. J. Carver, C. A. Hunter and E. M. Seward, "Structure-activity relationship for quantifying aromatic interactions", *Chem. Commun.*, **1998**, 775-776.
16. S. B. Ferguson, E. M. Sanford, E. M. Seward and F. Diederich, "Cyclophane-arene inclusion complexation in protic solvents: Solvent effects versus electron donor-acceptor interactions", *J. Am. Chem. Soc.*, **1991**, *113*, 5410-5419.
17. C. A. Hunter and J. K. M. Sanders, "The nature of  $\pi$ - $\pi$  interactions", *J. Am. Chem. Soc.*, **1990**, *112*, 5525-5534.
18. T. M. Krygowski, M. K. Cyranski, Z. Czarnocki, G. Hafelinger and A. R. Katritzky, "Aromaticity: A theoretical concept of immense practical importance", *Tetrahedron*, **2000**, *56*, 1783-1796.
19. T. M. Krygowski, "Crystallographic studies of inter- and intramolecular interactions reflected in aromatic character of  $\pi$ -electron systems", *J. Chem. Inf.: Comput. Sci.*, **1993**, *33*, 70-78.
20. T. M. Krygowski and M. K. Cyranski, "Two faces of the structural aspects of aromaticity", *Phys. Chem. Chem. Phys.*, **2004**, *6*, 249-255.
21. F. H. Allen and W. D. S. Motherwell, "Applications of the Cambridge structural database in organic chemistry and crystal chemistry", *Acta Cryst.*, **2002**, *B58*, 380-388.
22. G. A. Jeffrey, "An introduction to hydrogen bonding", Oxford University Press, New York, **1997**.
23. L. Chen, F. Jiang, Z. Lin, Y. Zhou, C. Yue and M. Hong, "A basket tetradecavanadate cluster with blue luminescence", *J. Am. Chem. Soc.*, **2005**, *127*, 8588-8589.
24. Y. C. Liu, Z. F. Chen, S. M. Shi, H. S. Luo, D. C. Zhong, H. L. Zou and H. Liang, "Synthesis, crystal structure of polyoxovanadate complex of ciprofloxacin:  $V_4O_{10}(\mu_2-O)_2[VO(H-Ciprof)_2]_2 \cdot 13H_2O$  by hydrothermal reaction", *Inorg. Chem. Commun.*, **2007**, *10*, 1269-1272.
25. Y. Gong, C. Hu and H. Li, "Synthesis and crystal structure of a novel organic-inorganic hybrid hexavanadate  $[(phen)_4V_6O_{12}(CH_3OH)_4] \cdot 2CH_3OH \cdot 4H_2O$ ", *J. Mol. Struct.*, **2005**, *749*, 31-35.
26. J. I. Pankove, "Optical processes in semiconductors", Prentice-Hall, Englewood Cliffs, **1971**, 34-42.



Chiang Mai J. Sci. 2011; 38(2) : 252-262  
 www.science.cmu.ac.th/journal-science/josci.html  
 Contributed Paper

## Solvothermal Synthesis, Sintering Behavior and Dielectric Properties of Potassium Niobate Fine Powders

Kittichai Jinachai [a], Athipong Ngamjarujana [b] and Apinpus Rujiwatra\*[a]

[a] Department of Chemistry and Center for Innovation in Chemistry (PERCH-CIC), Faculty of Science,  
 Chiang Mai University, Chiang Mai 50200, Thailand.

[b] Department of Physics and Materials Science, Chiang Mai University, Chiang Mai 50200, Thailand.

\*Author for correspondence; e-mail: apinpus@gmail.com

Received: 22 July 2010

Accepted: 30 December 2010

### ABSTRACT

Fine potassium niobate powders composing of sub-micrometer sized lumber particles were synthesized under solvothermal conditions, with the use of mixed water-ethyl alcohol as the reaction medium and the application of the prior ultrasonication as the activation step. The influences of ethyl alcohol on particle shape and size, and the prior ultrasonication on the sintering behavior of the synthesized powders are present and discussed in relative to the conventional hydrothermal cases. The temperature dependent dielectric constants ( $\epsilon'$ ) and dielectric losses ( $\tan \delta$ ) of the sintered ceramics are also included, showing the origin of the losses to stem from the loss of potassium oxide in the sintering process.

**Keywords:** potassium niobate, solvothermal synthesis, sonocatalyzation, sintering, dielectric property.

### 1. INTRODUCTION

The emergence of the “*green attitude*” has resulted in the attempts to develop the green alternatives for various technologically important materials and processes including lead, despite of its important role technologically. Along this line, potassium niobate ( $\text{KNbO}_3$ , KN) has appeared as one of potential candidates for the lead-free piezoelectric materials. This is due to its excellent inherent properties and potential applications, for example, as an optical wave guide and devices for frequency doubling, holographic storage and surface acoustic wave [1-5]. The material is conventionally prepared by solid state reactions, which demand high temperatures and multiple cycles of heating-

and-grinding to assure the completeness of the reactions [6]. Besides being the energy-consumable process, the other drawbacks of the solid-state processes such as the formation of undesired impurities and aggregations are inherent [7]. During the last decade, the hydrothermal technique has been proved to be efficient for the preparation of KN in various forms, including fine powder, one-dimensional structure and thin film [8-11]. Despite of the promising future of the material and the technique, the practical application and commercialization of KN yet faces a major problem with sintering. At effective sintering temperature and duration,

the rapid vaporization of potassium oxide ( $K_2O$ ) and the large difference in properties of the cation involved result in the chemical control and densification problems [1]. The additions of other aiding compounds, such as magnesium oxide (MgO) and lead oxide (PbO), were reported to relieve the problems [12, 13].

Here, the adaptation of hydrothermal process by the use of mixed water-ethyl alcohol as reaction medium for the preparation of KN fine powders is described. The application of the ultrasonic wave on the reaction mixtures in prior to the synthesis is discussed. The sintering behavior and the preliminary investigation of the dielectric properties of the sintered ceramics are reported.

## 2. MATERIALS AND METHODS

The mixtures of niobium oxide ( $Nb_2O_5$ , Sigma-Aldrich 99.99%, 0.0056 mol) and potassium hydroxide (KOH, Merck 85%, 0.0028 mol) were first prepared in mixed water-ethyl alcohol liquid medium (0.278 mol of water, 0.086 mol of ethyl alcohol;  $C_2H_5OH$ , Merck 99.9%). The employed amount of KOH functioning as both reagent and mineralizer in the synthesis is the amount reported as the critical limit providing the successful synthesis [14]. Each mixture was then stirred and transferred into Teflon liners up to *ca.* 80% filling volume capacity. The mixtures were subsequently subjected to an autogenous pressure developed at 200°C for 1-24 hours. In order to study the effect of ultrasonication, some samples are ultrasonicated at 40( $\pm$ 5)°C for 1 h using a laboratory ultrasonic bath (Bandelin Electronic RK255H, 160/320W, 35kHz) before the reactions. The synthesized powders were finally recovered by filtration and washed with water until the pH of the filtrate was *ca.* 7 to assure the complete removal of the alkali.

Powder X-ray diffraction (XRD; Bruker

D8 Advance diffractometer, Ni-filtered,  $CuK_{\alpha}$ ,  $\lambda=1.54098 \text{ \AA}$ , 40 kV, 30 mA) was used in characterizing the synthesized crystalline phases. Lattice parameters of these phases were refined from the collected XRD patterns. Selected area electron diffraction (SAED) equipped by a transmission electron microscope (TEM; JEOL JEM-2010) was also used in characterizing growth direction of the elongated particles, whereas a field emission scanning electron microscope (SEM; JEOL JSM-6335F) was used in examining morphologies and sizes of the composing particles.

The synthesized powders composing of a single orthorhombic KN according to the XRD results were chosen for the sintering experiments. The powders were ground and pressed uniaxially at 100 bars and room temperatures to make the pellets of 10.15 mm in diameter and 2.45-2.75 mm in thickness. The obtained pellets were then sintered at 1,025°C for 1 hour (Carbolite, 2416CG) using a heating-cooling rate of 3°C min<sup>-1</sup>. After the sintering, densities of the sintered ceramics were evaluated using Archimedes technique [15]. Phase and microstructure of the sintered pellets were investigated by XRD and FESEM, respectively.

The dielectric properties of the sintered ceramics were studied as functions of both temperature and frequency using an automated dielectric measurement system and a silver electrode (Dupont, QS 171), which was prepared by printing on the lapped surfaces followed by firing at 600°C for 1 h. The computer-controlled dielectric measurement system consists of a precision LCR meter (Thonghui, TH2819A) and a temperature chamber. The temperature dependent measurements were performed using a Keithley Model 2,000-digit multimeter which was equipped by a temperature chamber, when the capacitance and the dielectric loss

tangent were determined over the temperature range of 50-500°C with the frequency ranging from 0.1 to 100 kHz.

### 3. RESULTS AND DISCUSSION

Figure 1 and 2 shows the XRD patterns of the powders obtained from the reactions conducted at 200°C for varied reaction times, with and without prior ultrasonication for an hour, respectively. The application of the ultrasonication as described did not showed any significant difference in the XRD patterns of the synthesized powders. When the reactions were conducted for an hour, the presence of the other diffraction peaks which were not of the desired KN was plain. The identification of these phases could not be precisely done due to a deficiency in number

and intensity of these peaks. It can be nonetheless ascertained that the formation of KN, which could be indexed as the orthorhombic phase with space group  $Cm2m$  (JCPDS 32-822), already occurred as the major phase. According to the XRD results, the pure phase of KN could be obtained after 3 h, irrespective to the application of the prior ultrasonication on the reaction mixtures. The obtained KN powders could be readily indexed and refined in orthorhombic  $Cm2m$  (JCPDS 32-822), giving  $a = 5.689(8)$ - $5.695(8)$  Å,  $b = 5.721(11)$ - $5.737(10)$  Å and  $c = 3.982(11)$ - $3.984(12)$  Å. There was not therefore any apparent effect of the ultrasonication on the formation and phase of the synthesized KN powders, within a limit of the XRD technique.

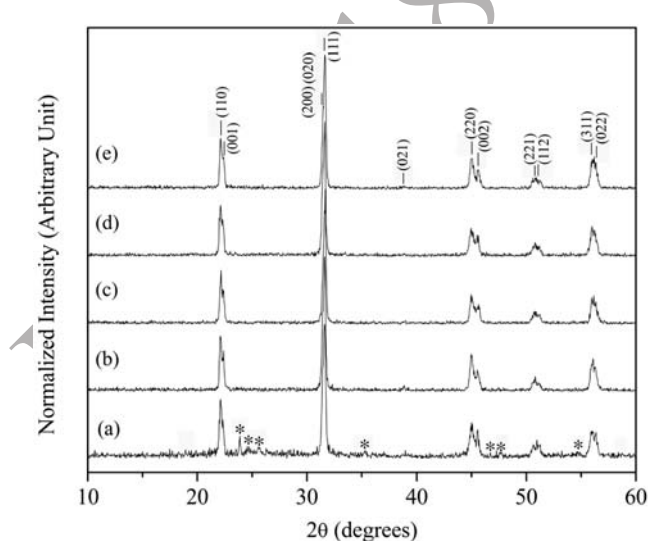


**Figure 1.** The XRD patterns of the powders obtained from the reactions conducted at 200°C for (a) 1 h, (b) 3 h, (c) 6 h, (d) 12 h and (e) 24 h on the ultrasonicated mixtures; \* indicates unidentified diffraction.

The SEM images show the synthesized KN powders to compose mostly of lumber particles with a few fraction of pseudo-cubic particles, independent also on the preparative

conditions. Figure 3 shows the representative images of the particles obtained from the reactions with and without the prior ultrasonication, illustrating well-defined shape



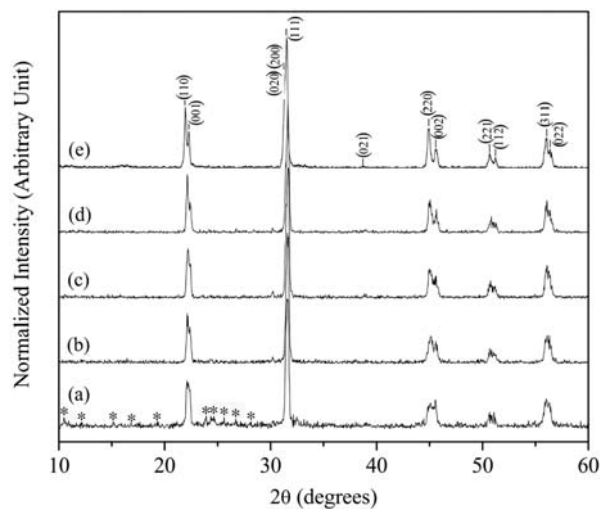


**Figure 2.** The XRD patterns of the powders obtained from the reactions conducted at 200°C for (a) 1 h, (b) 3 h, (c) 6 h, (d) 12 h and (e) 24 h on the mixtures without the prior ultrasonication; \* indicates unidentified diffraction.

of the KN particles for the powders obtained from the reactions with the prior ultrasonication. Sizes of these KN particles measured directly from the SEM were distributed in a range of approximately 0.1-1  $\mu\text{m}$  and 0.15-2.5  $\mu\text{m}$ , for the short and long axes, respectively. In contrast, the particles with a serious melting and poor-defined particle boundary were obtained from the reactions conducted without the prior application of the ultrasonic

wave. This may be rationalized by the ability of the ultrasonic wave in inducing the nucleation and in creation of the highly reactive and clean surface on the created nuclei which should promote the clean crystal growth in the afterward reactions [16]. The pressure generated under the solvothermal conditions generally causes the nucleation to occur as simultaneously as the crystal growth, which commonly results in hard aggregates [17].

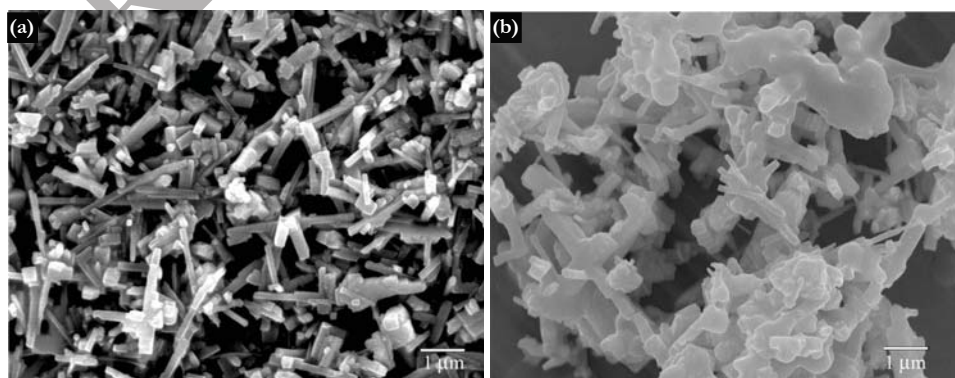


**Figure 3.** The SEM images exemplifying the lumber particles of potassium niobate derived from the reactions on (a) the ultrasonicated reaction mixture and (b) the mixture without prior ultrasonication, conducted under the same synthesis conditions.

In comparison to the former reports on the synthesis of KN fine powders using the hydrothermal reactions at the same temperature and KOH concentration of 200°C and 8 mol $\text{dm}^{-3}$ , several differences could be pointed out, although phase of the obtained KN is the same, which is the orthorhombic phase [14]. First, shape of the hydrothermally derived KN particles was largely pseudocubic, when the lumber particles could be obtained in this study. Second, sizes of the pseudocubic

particles were also distributed in a larger size region of 1-4  $\mu\text{m}$ , compared to the sub-micrometer sizes reported here. The use of mixed water-ethyl alcohol as a liquid medium apparently provided smaller sized and more elongated particles. Regarding the effective reaction, the employment of ethyl alcohol and the application of ultrasonic wave on the reaction mixtures did not result in any significant change.

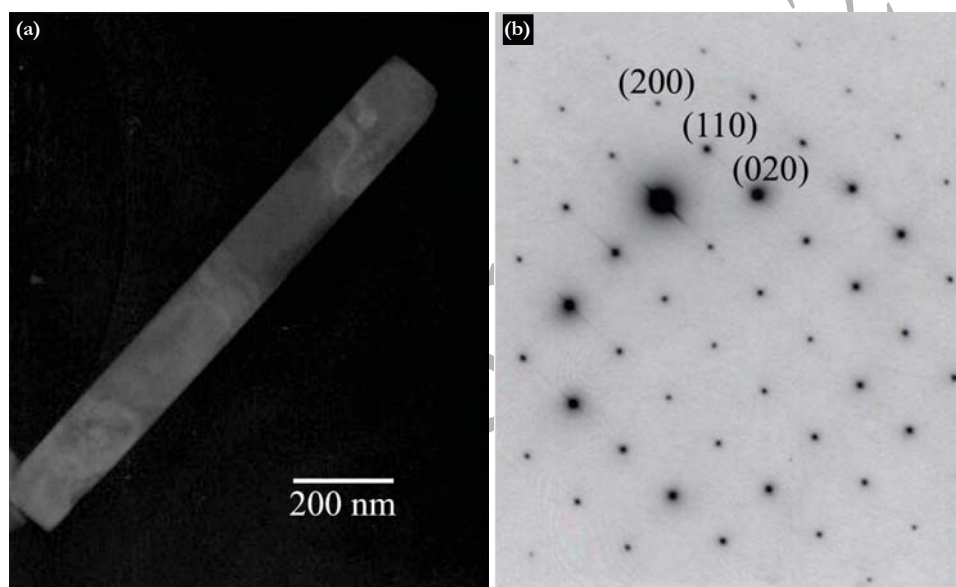


**Figure 4.** (a) The TEM image of the typical lumber potassium niobate particle with (b) the corresponding indexed SAED pattern based on the orthorhombic  $Cm2m$  (JCPDS 32-822).

The structure of the lumber particles was also evaluated through selected area electron diffraction (SAED) in the transmission electron microscope. Figure 4 shows the TEM images of the typical particle and the corresponding SAED pattern, which could be well indexed in the assigned orthorhombic  $Cm2m$  phase. The growth direction apparently lied along the crystallographic  $[110]$  direction.

The KN powders characterized by the XRD to be of the single orthorhombic phase

were chosen for the sintering experiments, including those obtained from the reactions conducted for 3-24 h, both with and without the prior ultrasonication. After the sintering, the diameters and thickness of the sintered bodies were substantially reduced; 8.35-8.60 mm and 2.10-2.30 mm for the sintered pellets compared to 10.15 mm and 2.45-2.75 mm for the green bodies. The contraction in diameter of  $\approx 18\%$  was slightly better than the contraction in thickness,  $\approx 14-16\%$ . This

corresponded to the volume shrinkage of *ca.* 36-42%. The densities of the sintered ceramics were measured, giving the results of *ca.* 95-98% in relative to the crystallographic density, 4.62 gcm<sup>-3</sup>. No correlation between the obtained values and the variation in synthesis reaction time could be observed, although the powders obtained from the reactions with the prior ultrasonication showed slightly better volume shrinkage and densification. The shrinkage and relative densities of *ca.* 40-42% and 96-98%, respectively, could be calculated for the ultrasonication cases, when the shrinkage of 36-39% with the corresponding relative densities of *ca.* 95% were obtained for the other cases. This could be due to the better defined particle shape and less melting between the particles in the former case as revealed by the SEM images.

The SEM images taken on the sintered KN pellets gave supportive evidence, as exemplified in Figure 5. The grain sizes of the sintered ceramic were measured and a slight growth of the sintered grain was revealed; 0.15-3.95  $\mu\text{m}$  and 0.25-4.45  $\mu\text{m}$  for the short and long axes. These results agree well with the calculated volume shrinkages and the calculated relative densities. It is apparent that the growth process occurred better along the short axis than the long axis, and resulted in an evolution of a pseudo-cubic grain from the pressurized lumber particles. It is also evident that the melting between grains was serious for the pellets which were prepared from the powders derived from prolonged solvothermal reaction, particularly those with the prior ultrasonication treatment. Regarding the hygroscopic problem commonly encountered with the sintering of KN [18], it was not the case in this study if the washing of the remaining alkali was performed carefully. The sensitivity to the atmospheric water may therefore attribute to the remaining of KOH which is hygroscopic.

The XRD was used to follow the change in phase, if any, after the sintering and the results are shown in Figure 6(a) and Figure 7(a). The remaining of the orthorhombic KN was significant, although the formation of the niobium-rich phase, KNb<sub>3</sub>O<sub>8</sub>, suggesting the loss of K<sub>2</sub>O during the sintering were evident. A develop of a big lump at low 2 $\theta$  region was additionally plain, implying the corruption of the long range order in the structure although the distinction between the three most intense peaks, including (020), (200) and (111), were clearer after the sintering. The exception was apparent for the sintered pellets which were prepared from the powders obtained from 24 h reaction with the prior ultrasonication, where there was no signature of the KNb<sub>3</sub>O<sub>8</sub> phase in the XRD pattern. This again reflects the merit of the application of the prior ultrasonication.

Figure 6(b) and Figure 7(b) show the temperature dependence of dielectric constants ( $\epsilon'$ ) and dielectric loss tangents ( $\tan \delta$ ) at 100 kHz for the sintered KN ceramics, revealing a difference in the measured values depending on the purity of KN according to the XRD patterns shown in the corresponding Figure 6(a) and Figure 7(a), respectively. Phase transition from the ideal cubic phase to the tetragonal phase was found around 425°C, while the tetragonal to the orthorhombic occurred around 225°C. The results are well consistent with the formerly reported values for the KN ceramics [18-21]. In the case of the ceramic composing of KN as nearly a single phase which was the one derived from the powders prepared from 3 h - 24 h reaction with the prior ultrasonication, the dielectric constants has increased with also a sharp peak transition, especially for the KN ceramics of high densities and good crystallinity. The KN ceramics which were fabricated from the powders prepared from the same conditions but without the prior ultrasonication, showed

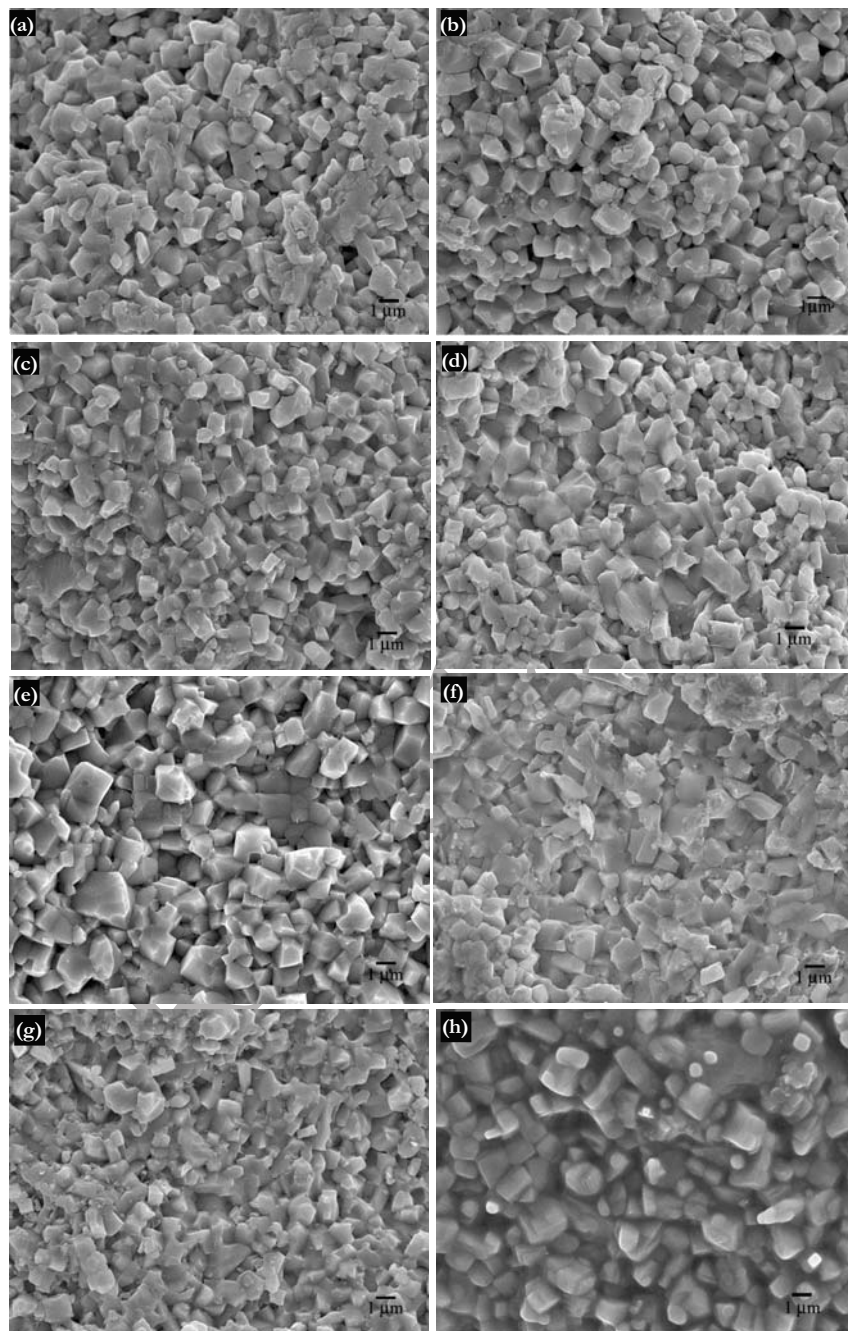


**Figure 5.** The SEM images of the sintered KN ceramics prepared from the powders obtained from the reactions conducted at 200°C for (a) 3 h, (b) 6 h, (c) 12 h and (d) 24 h on the mixtures without the prior ultrasonication, compared with those of the sonicated mixtures; (e) 3 h, (f) 6 h, (g) 12 h and (h) 24 h.

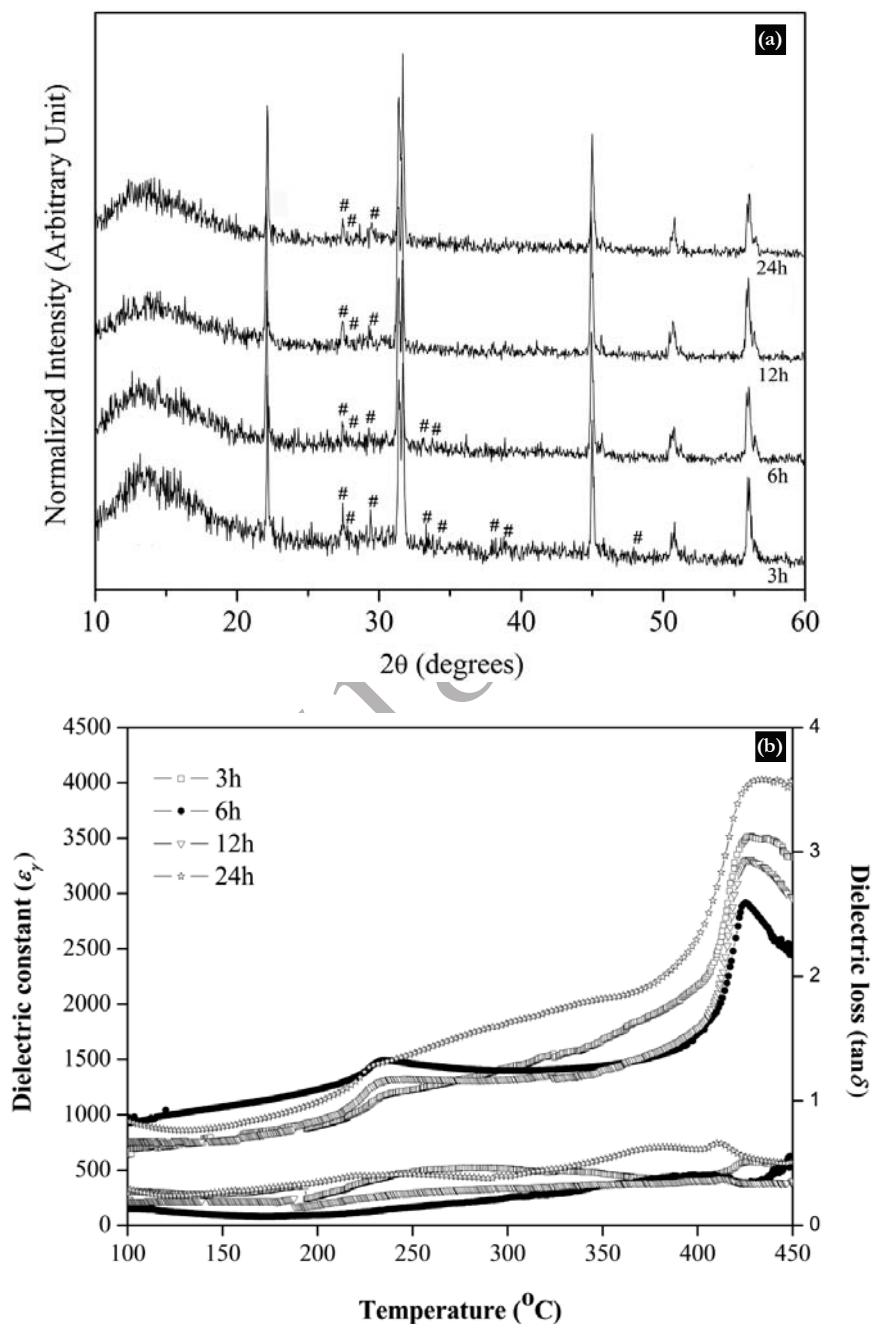


**Figure 6.** (a) The XRD patterns ( $\# = \text{KNb}_3\text{O}_8$ ) and (b) temperature dependence of dielectric properties measured on the KN ceramics prepared from the powders obtained from the reactions conducted at  $200^{\circ}\text{C}$  for (a) 3 h, (b) 6 h, (c) 12 h and (d) 24 h on the mixtures without the prior ultrasonication.



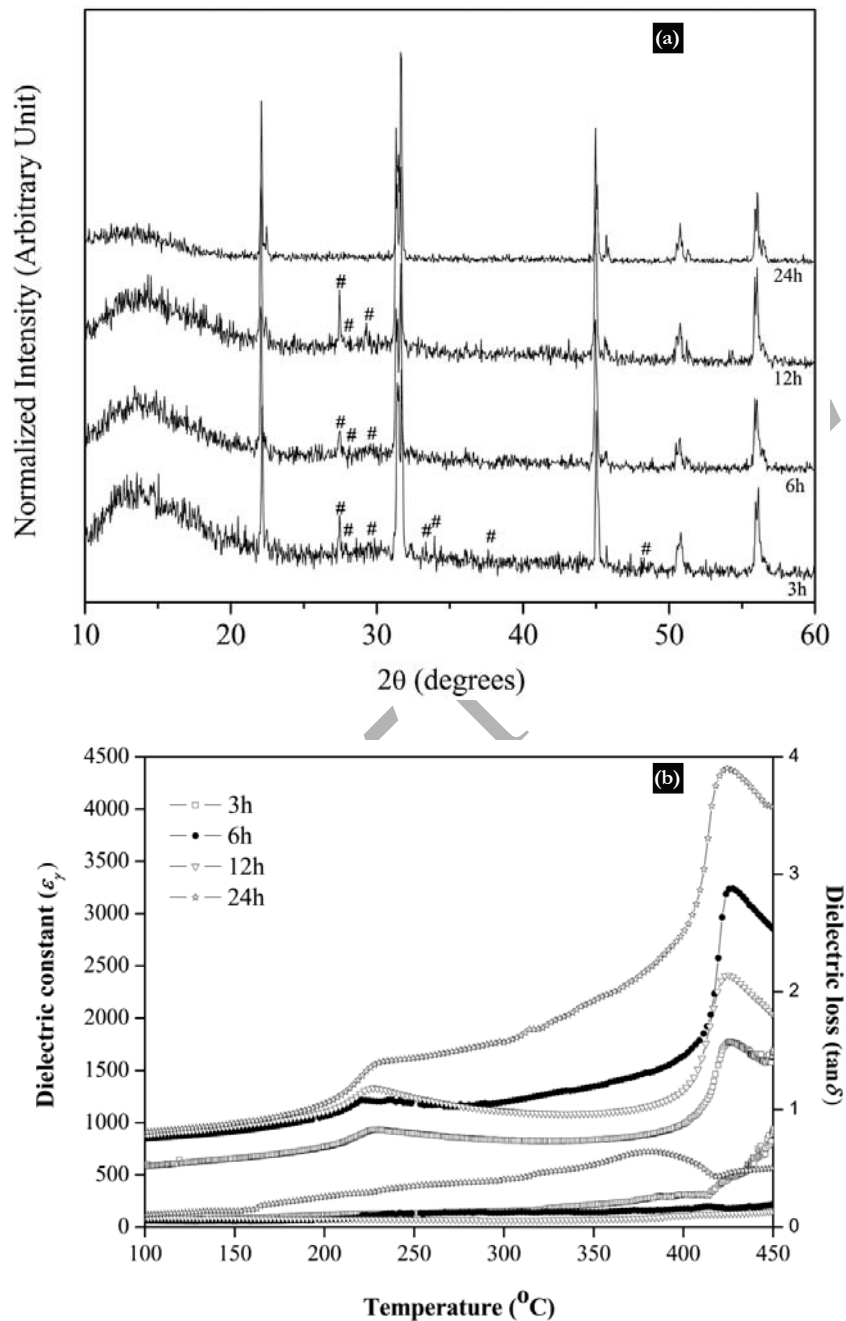


**Figure 7.** (a) The XRD patterns ( $\# = \text{KNb}_3\text{O}_8$ ) and (b) temperature dependence of dielectric properties of the KN ceramics prepared from the powders obtained from the reactions conducted at 200°C for (a) 3 h, (b) 6 h, (c) 12 h and (d) 24 h on the mixtures with the prior ultrasonication.

a broad peak transition, which should probably be due to the presence of the liquid phase in microstructure. This results were consistent with the XRD and SEM results that showed the formation of the second phase  $\text{KNb}_3\text{O}_8$  and the liquid phase in the microstructure due to the evaporation of  $\text{K}_2\text{O}$ . In general, it was evident that the ceramics prepared from the powders which were derived from the reactions with the prior ultrasonication showed higher dielectric constants and lower dielectric loss than those without the prior ultrasonication. This may attribute to the increase in oxygen vacancies which on the other hand contribute to the increase in conductivity [22].

#### 4. CONCLUSIONS

In summary, the sonocatalyzed ethano-thermal process has been attempted with the synthesis of potassium niobate fine powders, and proved to be able to provide the orthorhombic phase-pure KN powders under mild condition and rapid reaction times of at least 3 h. The use of mixed water-ethyl alcohol liquid medium apparently favored the formation of elongated lumber KN particles of sub-micrometer sizes, when the application of the prior ultrasonication on the reaction mixtures led to significant differences in sintering behavior, loss of  $\text{K}_2\text{O}$  and the tolerance of the orthorhombic KN to the sintering, as well as the corresponding dielectric properties. Dense KN ceramics of over 95% relative densities could be fabricated by conventional sintering without the hygroscopic problem. The significance of the prior ultrasonication on the reaction mixtures during the synthesis in enhancing both physical and electrical properties of the sintered ceramics was clearly illustrated.

#### ACKNOWLEDGEMENTS

The Thailand Research Fund is

acknowledged for financial support. K. Jinachai thanks to Department of Chemistry, Faculty of Science and the Graduate School, Chiang Mai University for a teaching assistant scholarship.

#### REFERENCES

- [1] Kakimoto K., Masuda I. and Ohsato H., Lead-free  $\text{KNbO}_3$  piezoceramics synthesized by pressure-less sintering, *J. Euro. Ceram. Soc.*, 2005; **25**: 2719-2722.
- [2] Tanaka K., Kakimoto K.I. and Ohsato H., Morphology and crystallinity of  $\text{KNbO}_3$ -Based nano powder fabricated by sol-gel process, *J. Euro. Ceram. Soc.*, 2007; **27**: 3591-3595.
- [3] Pribosic I., Makovec D. and Drofenik M., Chemical synthesis of  $\text{KNbO}_3$  and  $\text{KNbO}_3$ - $\text{BaTiO}_3$  ceramics, *J. Euro. Ceram. Soc.*, 2005; **25**: 2713-2717.
- [4] Yang R., Shen S.Y., Wang C.B., Shen Q. and Zhang L.M., Pulsed laser deposition of stoichiometric  $\text{KNbO}_3$  films on Si (100), *Thin Solid Films*, 2008; **516**: 8559-8563.
- [5] Muthurajan H., Kumar H.H., Samuel V., Gupta U.N. and Ravi V., Novel hydroxide precursor to prepare  $\text{NaNbO}_3$  &  $\text{KNbO}_3$ , *Ceram. Int.*, 2008; **34**: 671-673.
- [6] Su T., Jiang H., Gong H., Zhai Y., An alternative approach of solid-state reaction to prepare nanocrystalline  $\text{KNbO}_3$ , *J. Mater. Sci.*, 2010; **45**: 3778-3783.
- [7] Fluckiger U., Arend H., Oswald H.R., Synthesis of potassium niobate (V) powder, *Am. Ceram. Soc. Bull.*, 1977; **56**: 575-577.
- [8] Kumada N., Kyoda T., Yonesaki Y., Takei T. and Kinomura N., Preparation of  $\text{KNbO}_3$  by hydrothermal reaction, *Mater. Res. Bull.*, 2007; **42**: 1856-1862.
- [9] Liu J.W., Chen G., Li Z.H. and Zhang

- Z.G., Hydrothermal synthesis and photocatalytic properties of  $\text{ATaO}_3$  and  $\text{ANbO}_3$  ( $\text{A}=\text{Na}$  and  $\text{K}$ ), *Int. J. Hydrogen Energy*, 2007; **32**: 2269-2272.
- [10] Suchanek W.L., Synthesis of potassium niobate ( $\text{KNbO}_3$ ) thin films by low-temperature hydrothermal epitaxy, *Chem. Mater.*, 2004; **16**: 1083-1090.
- [11] Kajiyoshi K., Yanagisawa K., Feng Q. and Yoshimura M., Preparation of complex oxide thin film under hydrothermal and hydrothermal electro-chemical conditions, *J. Mater. Sci.*, 2006; **41**: 1535-1540.
- [12] Kosec M., Kolar D., On activated sintering and electrical properties of  $\text{NaKNbO}_3$ , *Mater. Res. Bull.*, 1975; **10**: 335-340.
- [13] Pribošić I., Makovec D., Drofenik M., PTCR effect in Pb-doped  $\text{KNbO}_3$ , *J. Mater. Res.*, 2002; **17** (12): 2989-2992.
- [14] Lu C.H., Lo S.Y., Lin H.C., Hydrothermal synthesis of non linear optical potassium niobate ceramic powder, *Mater. Lett.*, 1998; **34**: 172-176.
- [15] Morrel R., Handbook of properties of technical & engineering ceramics, *HMSO Publications*, London, 1989.
- [16] Suslick K.S., Sonochemistry, *Science*, New Series, 1990; **247**(4949): 1439-1445.
- [17] Riman R.E., Suchanek W.L. and Lencka M.M., Hydrothermal crystallization of ceramics, *Ann. Chim. Sci. Mat.*, 2002; **27** (6): 15-21.
- [18] Matsumoto K., Hiruma Y., Nagata H. and Takenaka T., Piezoelectric properties of  $\text{KNbO}_3$  ceramics prepared by ordinary sintering, *Ferroelectrics*, 2007; **358**: 169-174.
- [19] Ishikawa M., Takiguchi N., Hosaka H. and Morita T., Nondoped potassium niobate ceramics synthesized by hydrothermal method with optimum temperature condition, *Jpn. J. Appl. Phys.*, 2008; **47** (5): 3824-3828.
- [20] Tan C.K., Goh G.K.L. and Cheah W.L., Dielectric properties of hydrothermally epitaxied I-V perovskite thin films, *Thin Solid Films*, 2007; **515**: 6577-6581.
- [21] Ishikawa M., Kadota Y., Takiguchi N., Hosaka H. and Morita T., Synthesis of Nondoped Potassium Niobate Ceramics by Ultrasonic Assisted Hydrothermal Method, *Jpn. J. Appl. Phys.*, 2008; **47**(9): 7673-7677.
- [22] Singh G., Tiwari V.S. and Gupta P.K., Role of oxygen vacancies on relaxation and conduction behavior of  $\text{KNbO}_3$  ceramic, *J. Appl. Phys.*, 2010; **107**: 064103.